Quantitative analysis of Run-away B-stars

Master's Thesis in Physics

Presented by
Markus Dimpel
22.03.2021

Dr. Karl Remeis-Observatory
Friedrich-Alexander-Universität Erlangen-Nürnberg

Supervisor: Prof. Dr. Ulrich Heber

Contents

1. Introduction

Stars in our Galaxy are believed to be formed in star-forming regions in the Galactic disk and bulge. Young stars that are located at high galactic latitudes, far away from the disk, have been forced to leave their places of birth and are referred to as runaway stars. There are two classical mechanisms that are believed to operate in the ejection of such runaway stars. They are the binary supernova scenario (BSS, Blaauw 1961) and the dynamical ejection scenario (DES, Poveda et al. 1967).

In the BSS, the massive primary component of a binary system undergoes a core-collapse supernova resulting in the disruption of the binary system and the subsequent ejection of the secondary component at almost its orbital velocity. This process is shown schematically in Figure 1. In the DES, the ejection of a star takes place during close encounters in young clusters or associations. This scenario is most effective in terms of ejection velocity for interactions of two binaries. Under the most favourable conditions, both the BSS and DES are able to produce runaways with ejection velocities up to $\sim$400 kms^{-1}, but the majority of stars are ejected with velocities below $\sim$70 kms^{-1} as shown in Figure 2 for simulations of the BSS. Evidences for the two mechanisms have been found by Neuhäuser et al. (2020) and Dinçel et al. (2015) for the BSS, who are able to link the ejection of runaway stars to a neutron star and a supernova remnant, respectively, and Hoogerwerf et al. (2001) and Schoettler et al. (2020) for the DES, who both find runaway stars ejected from the Orion nuclear cluster.

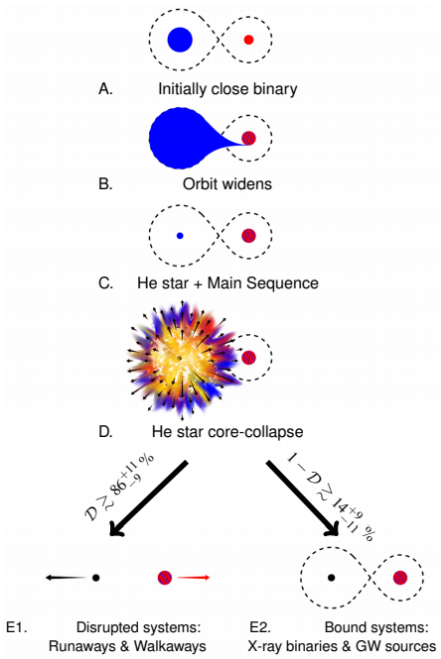

Figure 1: Schematic depiction of the binary supernova scenario (BSS). Figure taken from Renzo et al. (2019).

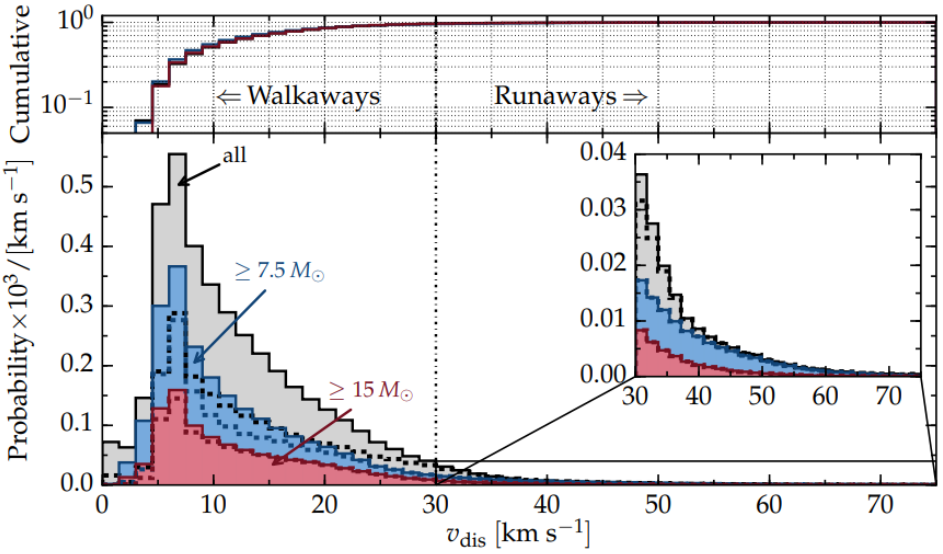

Figure 2: Simulated velocity distribution of main-sequence stars ejected from a binary system through a core-collapse supernova. Figure taken from Renzo et al. (2019).

A third and more powerful ejection mechanism, the so-called Hills mechanism (Hills 1988) is able to accelerate stars to even higher velocities up to multiple thousands of $\mathrm{km\,s^{-1}}$. In the Hills mechanism, a binary system is disrupted by the extreme tidal forces of a supermassive black hole (SMBH) during a close encounter. During the gravitational interaction, one component of the binary is captured by the SMBH and forced onto a close orbit while the other component is ejected at a velocity high enough to overcome the Galaxy's gravitational attraction.

The Hills mechanism was invoked, when the first hypervelocity stars (HVS) – stars that travel faster than their local escape velocity – were discovered in 2005 (Brown et al. 2005; Hirsch et al. 2005; Edelmann et al. 2005). More candidates of such hypervelocity stars were discovered from systematic radial-velocity surveys, but the quality of the astrometric data at hand was insufficient to constrain their places of origin and link them to the Hills mechanism. The astrometric data of more nearby runaway stars, however, was of better precision and accuracy and allowed Heber et al. (2008), Przybilla et al. (2008) and Irrgang et al. (2010) to exclude the Galactic center as place of origin of the runaway stars HD 271791 and HIP 60350. Due to the two runaways slightly exceeding the local escape velocity of the Milky Way, the term hyper-runaway star was coined in order to distinguish them from hypervelocity stars stemming from the Galactic center. For a sample of 96 main-sequence B-type runaway stars, Silva & Napiwotzki (2011) determine ejection velocities from the Galactic disk, and argue that the stars are separated in a high-velocity population with ejection velocities between 400 $\mathrm{kms^{-1}}$ and 500 $\mathrm{kms^{-1}}$ and a low-velocity population with a maximum velocity of 300 $\mathrm{kms^{-1}}$. This is demonstrated in Figure 3. However, the uncertainties on the ejection velocity were quite

large, especially for the high-velocity stars, due to the poor quality of the astrometric data.

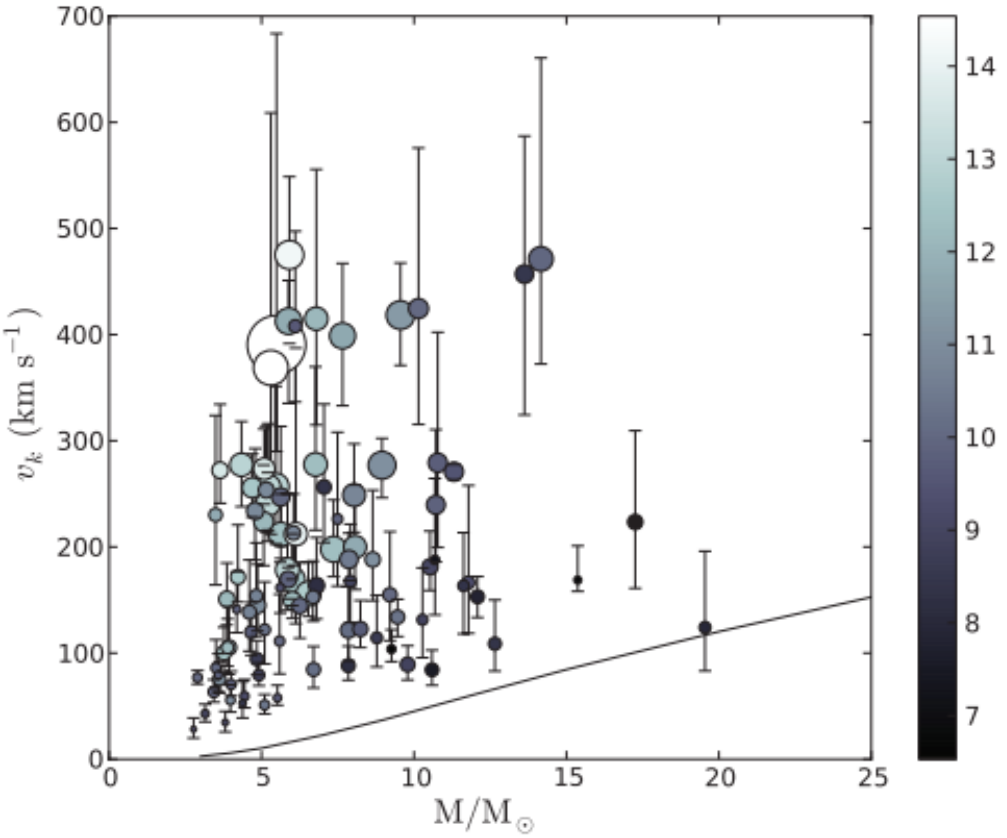

Figure 3: Ejection velocity−mass distribution of the Silva & Napiwotzki (2011) sample. The apparent visual magnitude of the stars is given by the gray scale. The size of the circles corresponds to the height above the Galactic plane and the black line marks the minimum velocity needed to reach a height of 1 kpc. Figure taken from Silva & Napiwotzki (2011).

The second data release of the *Gaia* mission (*Gaia* DR2, Gaia Collaboration et al. 2016, 2018) became a game changer for kinematic studies of hypervelocity and runaway stars. Making use of the astrometric *Gaia* data of unprecedented precision, Irrgang et al. (2018) and Kreuzer et al. (2020) reanalyze 40 hypervelocity stars and are able to eliminate the Galactic center as the place of origin for almost all targets with a relatively well-constrained place of origin. Similarly, Hattori et al. (2019) revisited the candidate hypervelocity star LAMOST-HVS1 and traced back the stars orbit to the Galactic disk, rather than the Galactic center. Evidence for the operation of the Hills mechanism, however, has been found by Koposov et al. (2020), who discovered the A-type star S5-HVS1 most likely originating in the Galactic center with an ejection velocity of $\sim$1800 kms^{-1}.

With the recent Early Data Release 3 of the *Gaia* mission (*Gaia* EDR3, Gaia Collaboration et al. 2020) we expect further improvement of the astrometric data and therefore revisit a sample of 41 runaway star candidates in the Galactic halo, comprised mainly of the fastest and a hand-full of less extreme stars from the analysis of Silva & Napiwotzki (2011), three of the LAMOST-HVS candidates and the two hyper-runaway stars HD 271791 and HIP 60350.

We will discuss the target sample and the available *Gaia* EDR3 data in Sections 2 and 3. Using the results of the spectroscopic analysis in Section 4, we will derive spectrophotometric distances in Section 5. We analyze the kinematics of the target stars in Section 6 and give a summary in Section 7.

2. Target sample

Before introducing our target sample of runaway stars, we want to briefly summarize the analysis of Silva & Napiwotzki (2011) to further motivate the work presented in this thesis.

Silva & Napiwotzki (2011) compiled an initial sample of 174 early-type candidate runaway stars located at high galactic latitudes from the literature. The majority of the candidate stars originated from the Palomar-Green (PG) and the Edinburgh-Cape (EC) surveys but also stars from various other studies were included. Thus the data collected for their study varies in terms of quality, the underlying analysis methods and models, as their sample includes data from studies based on high-resolution spectroscopy as well as medium-resolution spectroscopy and in some cases, the atmospheric parameters were derived from Stroemgren photometry only.

In order to classify the stars in their initial sample according to their evolutionary status, Silva & Napiwotzki (2011) consider three criteria: The position of the stars in the $T_{\rm eff} - \log(g)$ diagram, their projected rotational velocities $v \sin(i)$ and their abundance patterns. While it should in principle be possible to identify main-sequence (MS) stars from their position in the $T_{\rm eff} - \log(g)$ diagram, the region of interest for B-type stars is crossed by a population of evolved blue stars, the so-called blue horizontal branch (BHB). Instead of the heavier $(3 - 15\,M_{\odot})$ core hydrogen burning MS B-stars, stars on the BHB burn helium in their cores and hydrogen in a shell around the core and are significantly less massive ($\sim 0.5\,M_{\odot}$). A position of a candidate MS star that coincides with the BHB may hint towards an evolved nature of the star. The projected rotational velocity of the stars is a further indicator for the evolutionary status, since the evolved BHB stars are expected to rotate slowly, below $\lesssim 40\,\mathrm{km s^{-1}}$. The chemical abundance pattern of a star can also be used for the classification, as the young main-sequence stars typically show solar metal abundances, while the abundances of blue horizontal branch stars strongly deviate from the solar abundance pattern. By evaluating these three criteria for their initial sample, Silva & Napiwotzki (2011) classified 96 stars to be likely or very likely on the main-sequence.

For the 96 main-sequence candidates they derive stellar masses and ages by comparing temperatures and surface gravities to evolutionary tracks. Using the temperatures, gravities and masses of the stars, they computed the absolute magnitudes to derive distances for their target stars via the distance modulus. They complemented their distances with radial velocities from the literature and proper motion measurements from various catalogues to derive the full space motion of the stars and carry out a kinematic analysis. By tracing the stars' trajectories back in time to the Galactic plane they calculated ejection velocities using a modification of the Galactic potential of Allen & Santillan (1991). The resulting distribution of ejection velocities is plotted in Figure 3. While Silva & Napiwotzki (2011) find that the majority of the stars are ejected at velocities below $\sim$300 $\mathrm{km s^{-1}}$, there are also 11 stars with ejection velocities of $\sim$400 to 500 $\mathrm{km s^{-1}}$. Thus they argue that there may exist two separate populations of runaway stars, a low-velocity population with ejection velocities up to $\sim$300 $\mathrm{km s^{-1}}$ and a high-velocity

population above $\sim$400 kms^{-1}. It is unclear, however, whether these high-velocity stars are just extreme cases of runaway stars or are the lower tail of the hypervelocity stars.

The uncertainties on the ejection velocities of Silva & Napiwotzki (2011) are quite large due to the limited quality of the astrometric data. For some of the fastest stars the uncertainties on the ejection velocities even exceed 100 kms^{-1}. With the recent early data release 3 of the *Gaia* mission, providing astrometric measurements of unprecedented precision, it is worthwhile to revisit these runaway stars to further constrain their kinematic properties and potentially gain new insights. To this end, we investigate a sample of 41 runaway candidates, consisting of some of the fastest and a hand-full of less extreme stars from the analysis of Silva & Napiwotzki (2011) as well as three of the candidate hypervelocity stars of the LAMOST survey – LAMOST-HVS1, LAMOST-HVS3 and LAMOST-HVS4 (Zheng et al. 2014; Huang et al. 2017; Li et al. 2018; Hattori et al. 2019) – and the two hyper-runaway stars HD 271791 (Heber et al. 2008; Przybilla et al. 2008) and HIP 60350 (Irrgang et al. 2010). Additionally, the runaway candidate HD 151397 completes our sample. Unlike all the other sample stars, the latter is located inside the Galactic disk but appears to depart from it. HD 151397 was suggested to be a runaway star from the open cluster NGC 6321 by Blaauw (1961), but it seems to be ignored as no follow-up studies can be found in the literature.

Although Silva & Napiwotzki (2011) already provide atmospheric and stellar parameters for the majority of our target stars, we will still carry out a spectroscopic analysis (see Section 4) for all of our target stars, since Silva & Napiwotzki (2011) mostly compiled data from various studies resulting in a rather inhomogeneous sample in terms of quality of the data and analysis strategies.

3. Astrometric data

In order to kinematically investigate the runaway stars, that is to trace back their orbits to the Galactic plane of the Milky Way, their current position and velocity needs to be known. On 25 April 2018 the second data release of ESA's *Gaia* mission (*Gaia* DR2, Gaia Collaboration et al. 2016, 2018) was released and provided astrometric measurements of unprecedented precision for more than 1.3 billion sources. The spatial coordinates, proper motions and parallaxes from *Gaia* DR2 have already been used in various studies of hypervelocity and runaway stars, for example Irrgang et al. (2018) and Raddi et al. (2021).

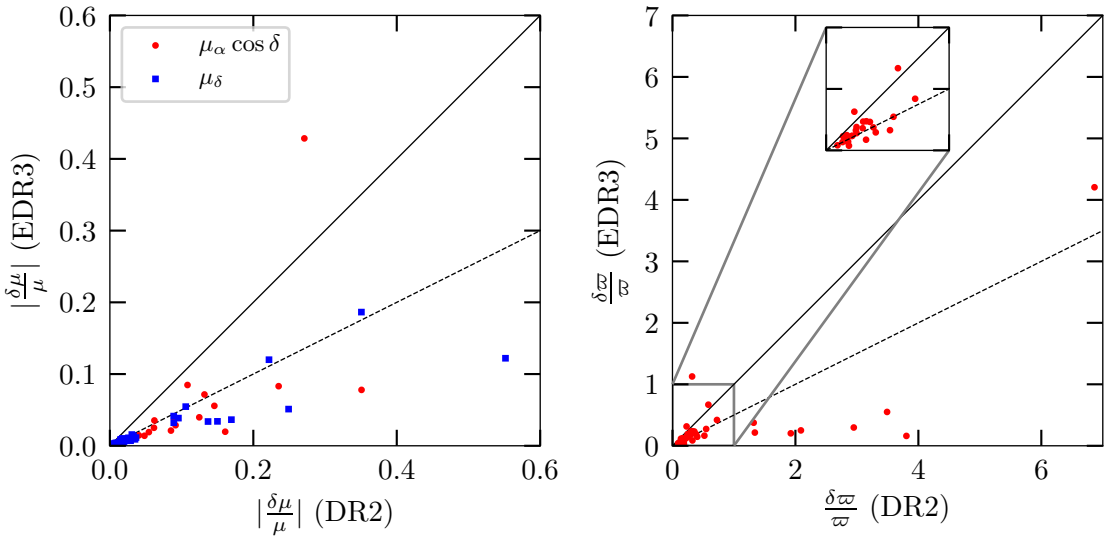

Figure 4: Comparison of the relative uncertainties of proper motion measurements (left panel) in the direction of right ascension $\mu_\alpha \cos\delta$ (red dots) and declination μ_δ (blue squares) and parallaxes ϖ (right panel) from *Gaia* DR2 and EDR3. For orientation, the identity line (black) and a line with slope $\frac{1}{2}$ (dashed) are shown.

Only recently on 3 December 2020, the *Gaia* Early Data Release 3 (*Gaia* EDR3, Gaia Collaboration et al. 2020) was released, extending the time span of the data collection to 34 month, compared to the 22 months for *Gaia* DR2. Thus, the astrometric data provided by EDR3 can be expected to further increase in precision compared to DR2 and consequently improve the results of kinematic studies. To get a brief overview of the improvement of the data, the relative uncertainties of the two proper motion components – ($\mu_\alpha \cos\delta$, μ_δ) in the direction of right ascension and declination respectively – and the parallaxes ϖ of the stars in the sample are plotted in Figure 4 as a comparison between *Gaia* DR2 and EDR3. There is one star for which the relative uncertainty on $\mu_\alpha \cos\delta$ has decreased, however for all the other stars the uncertainties on the proper motions have improved, in most cases even by a factor of 2 or more (see left panel of

Figure 4). Since many runaway stars are quite distant, often at more than 5 or even 10 kpc, parallax measurements may not be useful in some cases due to large uncertainties or even negative values. This is well demonstrated in the right panel of Figure 4, where the relative parallax uncertainties are compared for *Gaia* DR2 and EDR3. Especially in the case of the second data release, some of the *Gaia* parallax uncertainties are well above 100% and cannot be used to get a well constrained estimate on the distance of the stars. While the overall precision of the parallaxes increases with EDR3 and even most of the "unusable" parallaxes improve to $\frac{\delta\varpi}{\varpi} \lesssim 50\%$ there are still few cases in the sample for which the parallaxes cannot be used, including two stars with negative parallax measurements. Thus an independent method to determine the stars' distances is needed. The *Gaia* EDR3 proper motions and parallaxes of the sample stars are listed in Table 1.

#	Object	$\mu_\alpha \cos\delta$ (mas/yr)	μ_δ (mas/yr)	ϖ (mas)	ϖ_0 (mas)	RUWE
1	BD +20 3004	−11.30 ± 0.05	5.83 ± 0.04	0.52 ± 0.05	−0.030	1.00
2	BD −15 115	4.29 ± 0.06	−1.03 ± 0.06	0.18 ± 0.05	−0.033	0.77
3	BD −2 3766	0.69 ± 0.06	17.25 ± 0.04	0.22 ± 0.05	−0.036	1.08
4	EC 04420−1908	2.63 ± 0.02	−0.53 ± 0.02	0.08 ± 0.02	−0.035	0.99
5	EC 09452−1403	−7.21 ± 0.03	3.52 ± 0.03	0.13 ± 0.03	−0.037	1.07
6	EC 10087−1411	−8.69 ± 0.04	−5.11 ± 0.03	0.73 ± 0.03	−0.025	1.10
7	EC 10500−1358	−6.33 ± 0.04	−2.17 ± 0.03	0.17 ± 0.03	−0.045	0.91
8	EC 19596−5356	4.02 ± 0.03	−1.41 ± 0.02	0.05 ± 0.03	−0.033	1.00
9	EC 20104−2944	−3.72 ± 0.03	0.60 ± 0.03	0.27 ± 0.03	−0.041	1.04
10	EC 20252−3137	−5.87 ± 0.05	−2.88 ± 0.04	0.36 ± 0.06	−0.027	1.18
11	EC 23169−2235	4.44 ± 0.04	5.48 ± 0.04	0.32 ± 0.04	−0.046	1.12
12	HD 151397	−9.26 ± 0.03	−0.39 ± 0.02	0.52 ± 0.02	−0.028	0.81
13	HD 271791	−0.41 ± 0.04	4.70 ± 0.04	−0.05 ± 0.03	−0.043	1.07
14	HIP 105912	11.04 ± 0.05	−11.61 ± 0.04	0.46 ± 0.05	−0.030	0.98
15	HIP 108215	8.28 ± 0.05	−8.77 ± 0.03	0.39 ± 0.04	−0.031	1.05
16	HIP 114569	45.76 ± 0.05	32.22 ± 0.04	0.73 ± 0.05	−0.028	1.20
17	HIP 11809	−20.67 ± 0.04	−12.05 ± 0.04	0.53 ± 0.04	−0.064	1.05
18	HIP 55461	−0.54 ± 0.04	−5.89 ± 0.04	0.49 ± 0.04	−0.047	1.09
19	HIP 56322	2.91 ± 0.07	12.03 ± 0.05	0.34 ± 0.06	−0.029	1.12
20	HIP 60350	−13.30 ± 0.04	15.03 ± 0.05	0.28 ± 0.05	−0.039	1.29
21	HIP 70275	3.25 ± 0.06	−10.32 ± 0.05	0.39 ± 0.06	−0.030	1.38
22	HS 1914+7139	−2.93 ± 0.02	0.17 ± 0.02	0.05 ± 0.02	−0.016	1.09
23	LAMOST−HVS1	−3.56 ± 0.03	−0.79 ± 0.03	0.02 ± 0.03	−0.037	0.91
24	LAMOST−HVS3	1.15 ± 0.08	−0.55 ± 0.07	0.02 ± 0.08	−0.026	1.00
25	LAMOST−HVS4	0.13 ± 0.06	−0.34 ± 0.06	−0.05 ± 0.06	−0.018	1.00
26	PB 5418	1.67 ± 0.06	−2.87 ± 0.03	0.17 ± 0.04	−0.042	0.99
27	PG 0009+036	−1.84 ± 0.04	8.16 ± 0.03	0.19 ± 0.03	−0.037	1.01
28	PG 0122+214	−1.31 ± 0.05	−3.66 ± 0.03	0.15 ± 0.04	−0.040	0.79
29	PG 0855+294	6.23 ± 0.05	−4.18 ± 0.04	0.26 ± 0.05	−0.041	0.95
30	PG 0914+001	−2.62 ± 0.04	0.60 ± 0.02	0.09 ± 0.04	−0.037	1.02
31	PG 0955+291	−5.53 ± 0.04	−3.84 ± 0.04	0.04 ± 0.04	−0.038	0.95
32	PG 1205+228	−13.63 ± 0.04	1.17 ± 0.04	0.47 ± 0.05	−0.038	1.13
33	PG 1209+263	−1.19 ± 0.03	−0.93 ± 0.03	0.12 ± 0.03	−0.030	1.26
34	PG 1332+137	−6.57 ± 0.06	−8.46 ± 0.03	0.16 ± 0.05	−0.067	1.48
35	PG 1511+367	−0.60 ± 0.02	−13.52 ± 0.03	0.28 ± 0.03	−0.040	0.95
36	PG 1533+467	−10.80 ± 0.03	10.21 ± 0.04	0.45 ± 0.03	−0.010	1.10
37	PG 2219+094	−0.90 ± 0.05	−6.88 ± 0.06	0.07 ± 0.05	−0.063	1.25
38	PG 2229+099	−1.32 ± 0.03	−4.12 ± 0.03	0.13 ± 0.03	−0.033	1.03
39	PHL 159	−6.15 ± 0.05	−9.63 ± 0.04	0.39 ± 0.05	−0.025	1.11
40	PHL 2018	4.06 ± 0.04	−7.07 ± 0.03	0.17 ± 0.04	−0.064	1.09
41	PHL 346	6.21 ± 0.06	−4.69 ± 0.04	0.13 ± 0.05	−0.058	1.34

Table 1: Target stars and their *Gaia* EDR3 proper motion ($\mu_\alpha \cos\delta$, μ_δ), parallax ϖ, individual parallax zero-point offset ϖ_0 and Renormalised Unit Weight Error (RUWE). Each star is assigned a number (#) for identification in figures and tables.

4. Spectroscopic analysis

Although Silva & Napiwotzki (2011) already provide temperatures, gravities, radial velocities and more for the majority of our target stars, their data is mainly a compilation of results from multiple studies. Therefore, their data is very inhomogeneous in terms of quality, underlying models and analysis methods. In order to provide a sample of best possible homogeneity we therefore derive effective temperatures $T_{\rm eff}$, surface gravities $\log(g)$, projected rotational velocities $v \sin(i)$ and radial velocities $v_{\rm rad}$ of our target stars by analysing optical spectra obtained from the Archives of the European Southern Observatory (ESO) and the Large Sky Area Multi-Object Fiber Spectroscopic Telescope (LAMOST). Our sample therefore contains high-resolution spectra taken with the Ultraviolet and Visual Echelle Spectrograph (UVES, Dekker et al. 2000) and the Fiber-Fed Extended Range Optical Spectrograph (FEROS, Kaufer et al. 1999), as well as low-resolution LAMOST spectra. We use χ^2-minimization to fit a grid of synthetic spectra to the observed spectra over their entire spectral range.

4.1. Synthetic Spectra

The synthetic spectra are calculated in the so-called Atlas, Detail, Surface (ADS) or hybrid LTE/non-LTE approach, which is described in detail in Przybilla et al. (2011). In short, the structure of a model atmosphere in local thermal equilibrium (LTE) is calculated using the Atlas12 code (Kurucz 1996), while the Detail code (Giddings 1981) allows for departures from LTE. Finally, the synthetic spectrum is calculated with Surface (Giddings 1981). The grid of synthetic spectra used for this analysis was calculated for effective temperatures $T_{\rm eff}$ ranging from 10 000 K to 33 000 K in steps of 1000 K and surface gravities $\log(g)$ from 3.0 to 4.6 in steps of 0.2. Apart from Hydrogen and Helium, the synthetic spectra also model the spectral lines of a list of heavier elements (C, N, O, Ne, Mg, Al, Si, S, Ar and Fe).

To demonstrate the influence of effective temperature and surface gravity on the shape of the spectral lines, the Hydrogen Balmer lines Hα (λ = 6562.8 Å) and Hβ (λ = 4861.4 Å) are plotted in Figure 5 and Figure 6 for synthetic spectra of different parameter combinations. For a constant surface gravity, i.e. $\log(g) = 3.8$, the Balmer lines are strongest at the cooler end of the model grid at $T_{\rm eff} = 10\,000$ K. With increasing effective temperature, the strength of the Balmer lines decreases continually, see Figure 5. The surface gravity effects the shape of the Balmer lines in a different way. While the central drop of the lines is barely effected by the surface gravity for a constant temperature, the wings of the Balmer lines are very sensitive to $\log(g)$. Figure 6 shows, that an increase in surface gravity results in the broadening of the Balmer line wings.

Alongside the effective temperature and the surface gravity of a star, its rotational velocity is a third parameter that directly influences the shape of the spectral lines. By observing a rotating star, one side of the stellar sphere has a positive relative velocity, while the other side has a negative one. This results in a Doppler-broadened line shape, where the strength of the broadening is proportional to the stars rotation. Since an observer does not always see a star face-on and the inclination i, i.e. the angle between

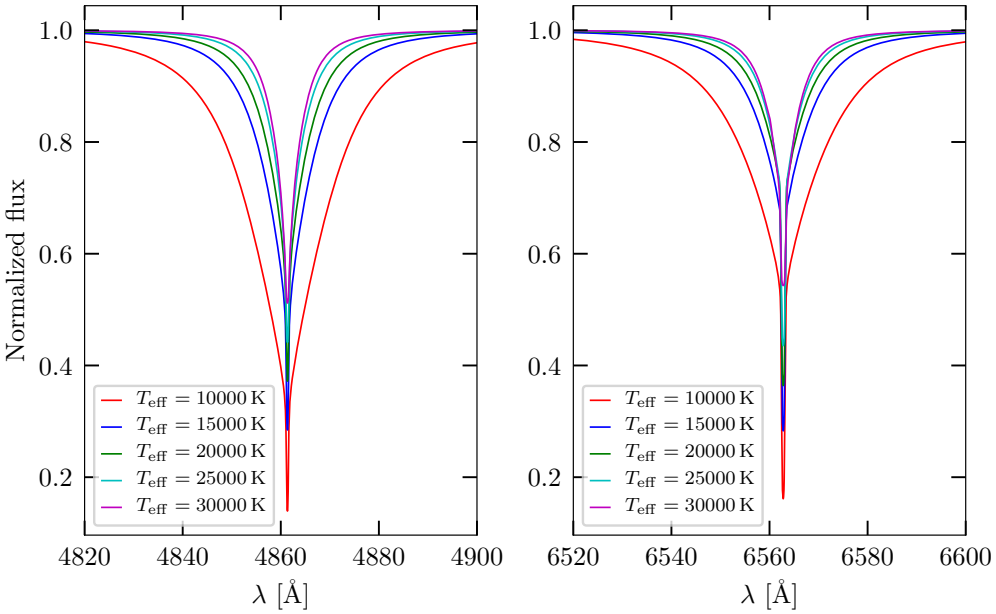

Figure 5: The Hydrogen Balmer lines Hβ (left panel) and Hα (right panel) in the synthetic spectra of surface gravity $\log(g) = 3.8$ and varying effective temperatures $T_{\rm eff}$.

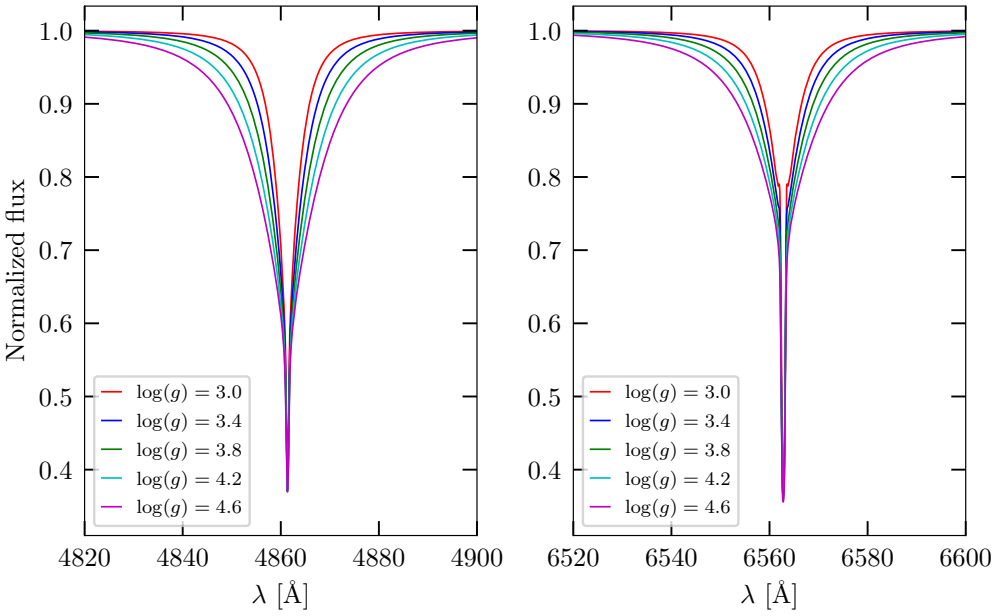

Figure 6: The Hydrogen Balmer lines Hβ (left panel) and Hα (right panel) in the synthetic spectra of effective temperature $T_{\rm eff} = 20\,000$ K and varying surface gravities $\log(g)$.

the line of sight of the observer and the rotational axis of the star, is generally unknown, it is only possible to derive the projected rotational velocity $v \sin(i)$ of a star, which is its rotational velocity projected to the line of sight, from its spectrum.

The radial velocity v_{rad} of a star, which is the relative velocity between the star and the observer, can also be derived from the spectrum but needs to be corrected to the barycentre of the solar system. Other than the effective temperature, surface gravity and rotational velocity, the radial velocity does not affect the shape of spectral lines. Instead, it merely shifts the central wavelengths of the lines via the Doppler-effect toward larger or smaller wavelengths for positive and negative values of v_{rad}, respectively. From the shift in wavelength $\Delta\lambda$, the radial velocity can be directly determined via

$$\frac{\Delta\lambda}{\lambda_0} = \frac{v_{\mathrm{rad}}}{c},$$

where λ_0 is the central rest wavelength of a spectral line and $c = 299\,792\,458\,\mathrm{m/s}$ is the speed of light.

4.2. Echelle-Spectrographs and the collection of spectra

For our spectroscopic analysis of the target stars, we use optical spectra taken with the UVES, FEROS and LAMOST spectrographs. The two former ones are so-called Echelle-Spectrographs that, instead of having a single dispersing element, contain a second cross-dispersing element that separates the different orders of refraction vertically. This results in a two-dimensional image on the detector, resembling the steps of a ladder (french: "echelle"), thus the name Echelle-Spectrograph. During the data reduction the different orders of refraction will be combined to a one-dimensional spectrum.

Information on the spectra used for our analysis is listed in Table 2. The majority of the UVES spectra were provided by Dr. Roberto Raddi, who obtained the spectra during his observing run with program ID 0102.D-0388. The remaining UVES and FEROS spectra were compiled from the ESO archive (http://archive.eso.org/scienceportal/home) and the LAMOST spectra from the LAMOST archive (http://www.lamost.org/public/?locale=en). While FEROS covers the full wavelength range in the optical, UVES extends to slightly larger wavelengths at the red end and thus covers more of the Hydrogen Paschen series. The main disadvantage of UVES is, however, the gap of $\sim$600 Å between the blue and red channel, but in the case of our B-type stars there are not many spectral features in this region anyways.

4.3. Atmospheric parameters

As described in the previous subsection, the strengths and shape of spectral lines vary with a star's atmospheric parameters, that is the effective temperature, the surface gravity, the helium abundance $n(\mathrm{He})$ and the microturbulent velocity ξ, and its projected rotational velocity. This does not only apply to the Balmer lines, shown in Figure 5 and Figure 6, but also to the Paschen lines and spectral lines of any other element that are present in the spectrum. Thus it is possible to derive the atmospheric parameters, the

#	Object	Spectorgraph	R	spectral range [Å]	S/N	$N_{\rm tot}$
2	BD −15 115	UVES	35 300	3732-5000, 4583-6687,6650-10 430	158	3
3	BD −2 3766	UVES	28 445	3732-5000, 5655-9465	206	4
4	EC 04420−1908	FEROS	48 000	3528-9217	39	8
5	EC 09452−1403	FEROS	48 000	3528-9217	24	7
6	EC 10087−1411	UVES*	31 585	3732-5000, 5655-9465	187	6
7	EC 10500−1358	UVES*	31 585	3732-5000, 5655-9465	141	4
8	EC 19596−5356	UVES	40 970	3732-5000	41	2
9	EC 20104−2944	UVES*	31 585	3732-5000, 5655-9465	126	4
10	EC 20252−3137	UVES*	31 585	3732-5000, 5655-9465	191	4
11	EC 23169−2235	FEROS	48 000	3528-9217	50	4
12	HD 151397	UVES*	31 585	3732-5000, 5655-9465	210	4
14	HIP 105912	UVES	28 445	3732-5000, 5655-9465	205	2
		FEROS	48 000	3528-9217	149	4
15	HIP 108215	FEROS	48 000	3528-9217	201	4
16	HIP 114569	FEROS	48 000	3528-9217	166	5
17	HIP 11809	UVES*	31 585	3732-5000, 5655-9465	149	4
18	HIP 55461	UVES*	31 585	3732-5000, 5655-9465	109	8
19	HIP 56322	UVES	28 445	3732-5000, 5655-9465	250	2
21	HIP 70275	FEROS	48 000	3528-9217	89	3
23	LAMOST−HVS1	LAMOST	1800	3700-9090	80	4
24	LAMOST−HVS3	LAMOST	1800	3700-9090	35	1
25	LAMOST−HVS4	LAMOST	1800	3700-9090	27	1
26	PB 5418	FEROS	48 000	3528-9217	50	3
27	PG 0009+036	LAMOST	1800	3700-9090	42	1
28	PG 0122+214	UVES	35 300	3732-5000, 4583-6687,6650-10 430	55	3
29	PG 0855+294	UVES*	31 585	3732-5000, 5655-9465	139	4
31	PG 0955+291	UVES*	31 585	3732-5000, 5655-9465	104	4
32	PG 1205+228	UVES*	31 585	3732-5000, 5655-9465	173	8
33	PG 1209+263	UVES*	31 585	3732-5000, 5655-9465	46	16
34	PG 1332+137	UVES*	31 585	3732-5000, 5655-9465	145	4
37	PG 2219+094	LAMOST	1800	3700-9090	120	1
38	PG 2229+099	UVES*	31 585	3732-5000, 5655-9465	99	8
39	PHL 159	UVES	35 300	3732-5000, 4583-6687,6650-10 430	160	3
40	PHL 2018	FEROS	48 000	3528-9217	69	6
41	PHL 346	UVES	35 300	3732-5000, 4583-6687,6650-10 430	139	3

Table 2: Properties of the optical spectra used for the analysis. Listed are the used spectrographs, the mean spectral resolution $R = \frac{\lambda}{\Delta\lambda}$, the wavelength range covered by the spectra, the mean signal to noise ratio S/N and the total number of spectra $N_{\rm tot}$. UVES spectra marked with * were provided by Dr. Roberto Raddi.

projected rotational velocity and the radial velocity of a star by fitting synthetic spectra to the observed ones via χ^2-minimization. Our analysis strategy is semi-automated so that the fitting parameters are fitted simultaneously and the main task for the user is to manually review and occasionally adjust the continuum normalization, which is realized via cubic spline interpolation. An example of the continuum fit is shown in Figure B.1. An extensive description of the fitting routine can be found in Irrgang et al. (2014). Although statistical error computation is in general a part of the fitting routine, we do not make use of it here as previous analyses have shown that the statistical uncertainties are negligible compared to systematic ones for the high-quality spectra analyzed here. By neglecting the statistical error computation it is possible to reduce the computation time drastically. An exemplary fit of the UVES spectrum of HIP 55461 is plotted in Figure 7 and the spectral fits of three stars with different atmospheric parameters are shown in Figures B.2 to B.19.

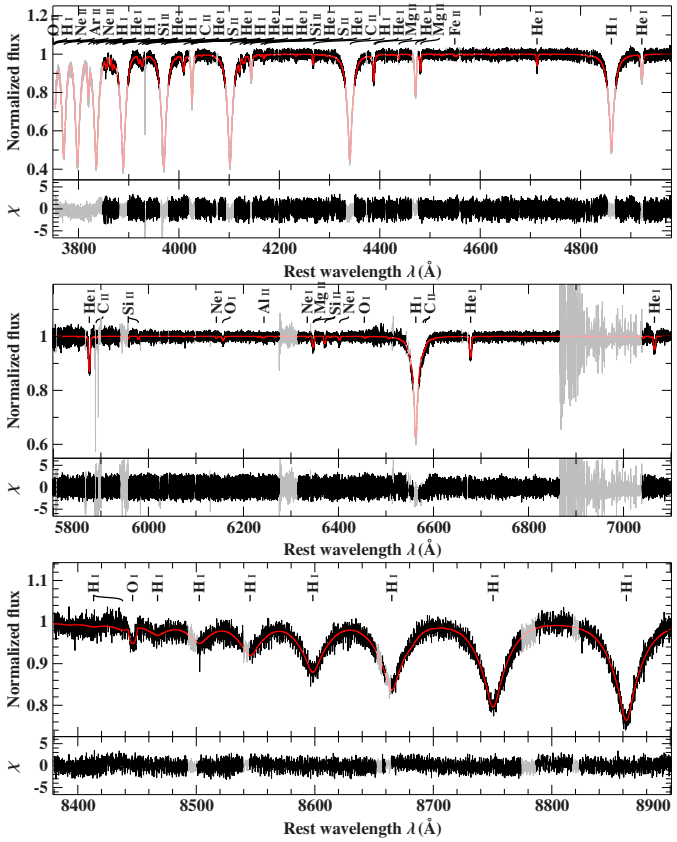

Figure 7: Fit of a synthetic spectrum (red) to the blue (top panel) and red (middle and bottom panel) range of a UVES spectrum of HIP 55461 (black) and residuals χ of the spectral fit. Gray-shaded areas of the spectrum are excluded from the fitting routine due to contamination with interstellar lines, insufficiently corrected telluric lines or untrustworthy regions of the model spectra.

#	Object	$T_{\rm eff}$ (K)	$\log(g)$ (cgs)	$v\sin(i)$	$v_{\rm rad}$	ξ	$\log(n({\rm He}))$
				($\rm km\,s^{-1}$)			
1	BD +20 3004[c]	13550 ± 180	3.75 ± 0.24	105 ± ...	22^{+14}_{-14}	–	–
2	BD −15 115	19830 ± 200	3.83 ± 0.04	$35.7^{+0.4}_{-0.4}$	$90.5^{+1.3}_{-1.3}$	1.6	−0.98
3	BD −2 3766	23620 ± 240	3.99 ± 0.04	$191.5^{+1.9}_{-1.9}$	$25.2^{+1.0}_{-1.0}$	2.5	−1.02
4	EC 04420−1908	12980 ± 130	3.16 ± 0.04	$228.2^{+2.3}_{-2.3}$	$211.1^{+2.5}_{-2.5}$	2.6	−0.83
5	EC 09452−1403	13730 ± 140	3.92 ± 0.04	$89.6^{+0.9}_{-0.9}$	$251.1^{+3.9}_{-3.9}$	1.4	−0.82
6	EC 10087−1411	13670 ± 140	3.88 ± 0.04	$187.0^{+1.9}_{-1.9}$	$116.5^{+2.3}_{-2.3}$	0.0	−0.89
7	EC 10500−1358	14680 ± 150	3.65 ± 0.04	$102.3^{+1.0}_{-1.0}$	$100.4^{+0.2}_{-0.2}$	2.6	−0.86
8	EC 19596−5356	15900 ± 160	4.05 ± 0.04	$236.5^{+2.4}_{-2.4}$	$-202.6^{+0.3}_{-0.3}$	2.4	−1.03
9	EC 20104−2944	14630 ± 150	4.13 ± 0.04	$43.6^{+0.4}_{-0.4}$	$139.0^{+0.4}_{-0.4}$	0.4	−0.95
10	EC 20252−3137	22880 ± 230	3.89 ± 0.04	$27.4^{+0.3}_{-0.3}$	$25.1^{+1.3}_{-1.3}$	4.9	−0.99
11	EC 23169−2235	14660 ± 150	4.08 ± 0.04	$165.9^{+1.7}_{-1.7}$	$81.9^{+1.5}_{-1.5}$	1.3	−0.85
12	HD 151397	29760 ± 300	4.26 ± 0.04	$47.5^{+0.5}_{-0.5}$	$149.6^{+0.6}_{-0.6}$	6.0	−1.04
13	HD 271791[a]	18630 ± 190	3.17 ± 0.04	$127.0^{+0.1}_{-0.1}$	$442.5^{+0.4}_{-0.4}$	6.5	−1.15
14	HIP 105912	23230 ± 230	3.81 ± 0.04	$108.0^{+1.1}_{-1.1}$	$2.5^{+5.4}_{-5.4}$	6.9	−0.96
15	HIP 108215	13780 ± 140	3.19 ± 0.04	$170.9^{+1.7}_{-1.7}$	$-61.1^{+1.3}_{-1.3}$	0.4	−0.85
16	HIP 114569	17350 ± 170	4.04 ± 0.04	$83.0^{+0.8}_{-0.8}$	$99.7^{+1.5}_{-1.5}$	0.6	−0.92
17	HIP 11809	12780 ± 130	4.17 ± 0.04	$218.7^{+2.2}_{-2.2}$	$2.5^{+9.0}_{-9.0}$	0.0	−0.99
18	HIP 55461	15240 ± 150	4.11 ± 0.04	$133.5^{+1.3}_{-1.3}$	$73.9^{+3.2}_{-3.2}$	1.0	−0.93
19	HIP 56322	24020 ± 240	4.10 ± 0.04	$172.9^{+1.7}_{-1.7}$	$260.3^{+1.3}_{-1.3}$	1.3	−1.08
20	HIP 60350[a]	16520 ± 170	4.08 ± 0.04	$135.1^{+0.2}_{-0.4}$	$263.6^{+0.4}_{-0.5}$	1.7	−0.98
21	HIP 70275	22760 ± 230	4.06 ± 0.04	$61.9^{+0.6}_{-0.6}$	$242.3^{+0.2}_{-0.2}$	1.5	−1.01
22	HS 1914+7139[b]	17600 ± 880	3.90 ± 0.10	250 ± ...	-39^{+10}_{-10}	–	–
23	LAMOST−HVS1	19180 ± 380	3.58 ± 0.08	$161.5^{+1.8}_{-1.5}$	$612.2^{+5.7}_{-5.7}$	8.0	−1.05
24	LAMOST−HVS3	12980 ± 260	4.02 ± 0.08	$227.5^{+18.7}_{-22.8}$	$360.9^{+5.1}_{-4.2}$	2.3	−1.05
25	LAMOST−HVS4	13520 ± 270	3.25 ± 0.08	$148.1^{+18.1}_{-20.0}$	$332.9^{+4.5}_{-5.0}$	0.0	−1.05
26	PB 5418	18580 ± 190	3.98 ± 0.04	$53.5^{+0.5}_{-0.5}$	$146.6^{+2.6}_{-2.6}$	0.9	−0.96
27	PG 0009+036	14970 ± 300	3.84 ± 0.08	$427.2^{+16.4}_{-\ 9.2}$	$141.6^{+5.7}_{-6.4}$	0.0	−1.05
28	PG 0122+214	19430 ± 190	4.00 ± 0.04	$121.9^{+1.2}_{-1.2}$	$33.4^{+2.8}_{-2.8}$	0.9	−1.03
29	PG 0855+294	20800 ± 210	4.17 ± 0.04	$130.9^{+1.3}_{-1.3}$	$64.3^{+0.3}_{-0.3}$	0.0	−1.06
30	PG 0914+001[c]	13100^{+400}_{-600}	$4.0^{+0.4}_{-0.5}$	325 ± ...	90^{+20}_{-20}	–	–
31	PG 0955+291	13340 ± 130	3.84 ± 0.04	$198.1^{+2.0}_{-2.0}$	$55.6^{+3.7}_{-3.7}$	0.0	−0.94
32	PG 1205+228	16240 ± 160	4.10 ± 0.04	$172.8^{+1.7}_{-1.7}$	$143.2^{+2.1}_{-2.1}$	1.2	−0.91
33	PG 1209+263	12100 ± 120	3.84 ± 0.04	$82.3^{+0.8}_{-0.8}$	$26.2^{+6.9}_{-6.9}$	6.0	−1.25
34	PG 1332+137	17110 ± 170	4.11 ± 0.04	$118.6^{+1.2}_{-1.2}$	$160.5^{+1.7}_{-1.7}$	0.5	−0.95
35	PG 1511+367[b]	16100 ± 805	4.15 ± 0.10	77 ± ...	102^{+11}_{-11}	–	–
36	PG 1533+467[b]	18500 ± 925	4.09 ± 0.10	215 ± ...	33^{+6}_{-6}	–	–
37	PG 2219+094	17970 ± 360	3.60 ± 0.08	$214.5^{+4.2}_{-3.4}$	$-38.2^{+1.5}_{-1.3}$	0.3	−1.05
38	PG 2229+099	17210 ± 170	3.89 ± 0.04	~ 0	$-14.0^{+0.7}_{-0.7}$	1.3	−0.98
39	PHL 159	21660 ± 220	4.04 ± 0.04	$23.3^{+0.2}_{-0.2}$	$87.8^{+0.6}_{-0.6}$	2.7	−1.01
40	PHL 2018	18690 ± 190	3.78 ± 0.04	$240.9^{+2.4}_{-2.4}$	$145.3^{+3.7}_{-3.7}$	2.9	−0.97
41	PHL 346	21570 ± 220	3.83 ± 0.04	$27.3^{+0.3}_{-0.3}$	$59.9^{+1.2}_{-1.2}$	7.7	−0.97

Table 3: Effective temperatures $T_{\rm eff}$, surface gravities $\log(g)$, projected rotational velocities $v\sin(i)$, radial velocities $v_{\rm rad}$, microturbulences ξ and helium abundaces $n({\rm He})$ of the target stars. [a] Parameters taken from Irrgang (2014). [b] Parameters taken from Silva & Napiwotzki (2011). [c] $T_{\rm eff}$ and $\log(g)$ obtained from a photometric analysis, $v\sin(i)$ and $v_{\rm rad}$ taken from Silva & Napiwotzki (2011).

The results of the spectroscopic analysis are summarized in Table 3. We assume systematic uncertainties on the effective temperature of 1% for stars with high-resolution UVES and FEROS spectra and 2% for low-resolution LAMOST spectra. Similarly, we assume systematic uncertainties of 0.04 and 0.08 on the surface gravity for high- and low-resolution spectra, respectively. For stars with low-resolution spectra we fix the Helium abundance to the solar value of $\log(n(\mathrm{He})) = -1.05$, where $n(\mathrm{He})$ is given as the particle fraction. From the uncertainties on temperature and gravity follows a systematic uncertainty of $\sim$0.5 kms^{-1} on the microturbulence and $\sim$0.05 on the helium abundance. For seven of the target stars no spectra were available in the ESO and LAMOST databases. For two of these seven stars the coverage of photometric measurements was sufficient to obtain estimates for the effective temperature and surface gravity with adequate precision be able to determine a reliable distance later on. The photometric analysis of the two stars will be discussed in Section 5. For the remaining five stars without spectra, atmospheric parameters and rotational and radial velocities are adopted from Irrgang (2014) and Silva & Napiwotzki (2011).

4.4. Stellar parameters

The effective temperatures and surface gravities of the sample stars are plotted against each other in Figure 8 as a so-called Kiel diagram. Overplotted are evolutionary tracks of B-type stars from Georgy et al. (2013) of metallicity $z = 0.014$ and different values of stellar rotation. By comparing our atmospheric parameters to these evolutionary models, we can interpolate the masses M and evolutionary ages τ_{evol} of our stars. In order to get a realistic estimate of the rotational velocity at the stellar equator, we assume a statistically averaged inclination of $\sin(i) = \frac{\pi}{4}$ for stars with $v \sin(i) < 150\,\mathrm{kms}^{-1}$ and $\sin(i) = 1$ otherwise. From the definition of the surface gravity of a star, $g = GMR^{-2}$, where G is the gravitational constant, it is also possible to directly obtain the stellar radius once its mass has been derived. Furthermore, the stellar luminosity can be easily calculated in solar units via $L/L_{\odot} = (R/R_{\odot})^2 \cdot (T_{\mathrm{eff}}/T_{\mathrm{eff},\odot})^4$, where the subscript $\odot$ denotes the solar values. The stellar parameters of the target stars are summarized in Table 4 and the given uncertainties are propagated from the uncertainties on T_{eff} and $\log(g)$. We also calculate an estimate for the stellar rotation with respect to the critical rotation $\Omega/\Omega_{\mathrm{c}}$, where we use the same assumptions for the inclination as above and calculate the critical rotation via $\Omega_{\mathrm{c}} = \sqrt{GM/R}$.

#	Object	M ($M_\odot$)	R ($R_\odot$)	$\tau_{\rm evol}$ (Myr)	$\log(L/L_\odot)$	$\Omega/\Omega_{\rm c}$
1	BD +20 3004	$4.50^{+0.27}_{-0.52}$	$4.3^{+1.4}_{-1.1}$	$132^{+31}_{-\ 6}$	$2.81^{+0.24}_{-0.23}$	0.30
2	BD −15 115	$7.88^{+0.20}_{-0.19}$	$5.64^{+0.28}_{-0.27}$	$32.4^{+1.1}_{-1.1}$	$3.65^{+0.05}_{-0.05}$	0.09
3	BD −2 3766	$9.92^{+0.20}_{-0.20}$	$5.27^{+0.25}_{-0.25}$	$16.7^{+0.9}_{-1.2}$	$3.89^{+0.05}_{-0.05}$	0.32
4	EC 04420−1908	$6.20^{+0.24}_{-0.23}$	$10.8^{+0.6}_{-0.6}$	78^{+8}_{-8}	$3.48^{+0.05}_{-0.05}$	0.69
5	EC 09452−1403	$4.19^{+0.10}_{-0.09}$	$3.71^{+0.18}_{-0.18}$	129^{+4}_{-4}	$2.65^{+0.05}_{-0.05}$	0.25
6	EC 10087−1411	$4.29^{+0.10}_{-0.09}$	$3.93^{+0.19}_{-0.19}$	129^{+5}_{-5}	$2.69^{+0.05}_{-0.05}$	0.41
7	EC 10500−1358	$4.98^{+0.13}_{-0.20}$	$5.49^{+0.28}_{-0.26}$	$111^{+16}_{-\ 5}$	$3.10^{+0.05}_{-0.05}$	0.31
8	EC 19596−5356	$5.04^{+0.11}_{-0.08}$	$3.50^{+0.17}_{-0.16}$	60^{+5}_{-6}	$2.85^{+0.05}_{-0.05}$	0.45
9	EC 20104−2944	$4.20^{+0.08}_{-0.08}$	$2.92^{+0.14}_{-0.14}$	$80^{+\ 8}_{-10}$	$2.55^{+0.05}_{-0.05}$	0.11
10	EC 20252−3137	$9.84^{+0.26}_{-0.25}$	$5.88^{+0.29}_{-0.28}$	$19.4^{+0.7}_{-0.7}$	$3.94^{+0.05}_{-0.05}$	0.06
11	EC 23169−2235	$4.35^{+0.08}_{-0.07}$	$3.15^{+0.15}_{-0.15}$	87^{+7}_{-8}	$2.62^{+0.05}_{-0.05}$	0.32
12	HD 151397	$13.80^{+0.28}_{-0.38}$	$4.54^{+0.22}_{-0.22}$	$1.3^{+1.3}_{-1.0}$	$4.16^{+0.05}_{-0.05}$	0.08
13	HD 271791	$10.9^{+0.4}_{-0.5}$	$14.2^{+0.8}_{-0.7}$	$23.8^{+1.8}_{-1.8}$	$4.34^{+0.05}_{-0.05}$	0.42
14	HIP 105912	$10.45^{+0.25}_{-0.24}$	$6.6^{+0.4}_{-0.4}$	$20.0^{+0.8}_{-0.8}$	$4.07^{+0.05}_{-0.05}$	0.25
15	HIP 108215	$6.53^{+0.29}_{-0.25}$	$10.7^{+0.6}_{-0.6}$	67^{+8}_{-9}	$3.57^{+0.05}_{-0.05}$	0.50
16	HIP 114569	$5.72^{+0.11}_{-0.10}$	$3.78^{+0.18}_{-0.18}$	$52.8^{+2.6}_{-3.8}$	$3.07^{+0.05}_{-0.05}$	0.20
17	HIP 11809	$3.50^{+0.06}_{-0.06}$	$2.54^{+0.13}_{-0.12}$	103^{+19}_{-21}	$2.19^{+0.05}_{-0.05}$	0.43
18	HIP 55461	$4.56^{+0.07}_{-0.07}$	$3.12^{+0.15}_{-0.15}$	70^{+7}_{-9}	$2.67^{+0.05}_{-0.05}$	0.32
19	HIP 56322	$9.78^{+0.20}_{-0.20}$	$4.61^{+0.23}_{-0.22}$	$12.5^{+1.7}_{-2.0}$	$3.81^{+0.05}_{-0.05}$	0.27
20	HIP 60350	$5.21^{+0.10}_{-0.10}$	$3.44^{+0.17}_{-0.17}$	55^{+5}_{-6}	$2.90^{+0.05}_{-0.05}$	0.32
21	HIP 70275	$8.80^{+0.14}_{-0.14}$	$4.58^{+0.22}_{-0.21}$	$17.6^{+1.2}_{-1.7}$	$3.71^{+0.05}_{-0.05}$	0.13
22	HS 1914+7139	$6.4^{+0.5}_{-0.5}$	$4.6^{+0.6}_{-0.6}$	50^{+11}_{-10}	$3.28^{+0.14}_{-0.14}$	0.49
23	LAMOST−HVS1	$8.53^{+0.27}_{-0.38}$	$7.8^{+0.8}_{-0.8}$	$35.1^{+2.8}_{-2.7}$	$3.88^{+0.09}_{-0.10}$	0.35
24	LAMOST−HVS3	$3.78^{+0.12}_{-0.12}$	$3.13^{+0.30}_{-0.29}$	138^{+13}_{-19}	$2.40^{+0.09}_{-0.09}$	0.47
25	LAMOST−HVS4	$6.0^{+0.5}_{-0.5}$	$9.6^{+1.0}_{-1.0}$	83^{+14}_{-14}	$3.44^{+0.1}_{-0.1}$	0.55
26	PB 5418	$6.53^{+0.12}_{-0.11}$	$4.33^{+0.21}_{-0.21}$	$42.4^{+1.9}_{-1.9}$	$3.30^{+0.05}_{-0.05}$	0.13
27	PG 0009+036	$5.25^{+0.27}_{-0.25}$	$4.5^{+0.5}_{-0.5}$	78^{+5}_{-5}	$2.97^{+0.09}_{-0.09}$	0.91
28	PG 0122+214	$6.93^{+0.11}_{-0.10}$	$4.36^{+0.20}_{-0.21}$	$33.8^{+1.9}_{-1.6}$	$3.39^{+0.05}_{-0.05}$	0.28
29	PG 0855+294	$7.35^{+0.14}_{-0.15}$	$3.69^{+0.18}_{-0.18}$	16^{+4}_{-5}	$3.36^{+0.05}_{-0.05}$	0.27
30	PG 0914+001	$4.0^{+1.0}_{-0.7}$	$2.8^{+1.8}_{-1.1}$	$113^{+\ 24}_{-111}$	$2.4^{+0.5}_{-0.4}$	0.62
31	PG 0955+291	$4.24^{+0.10}_{-0.10}$	$4.09^{+0.20}_{-0.20}$	138^{+5}_{-5}	$2.68^{+0.05}_{-0.05}$	0.45
32	PG 1205+228	$5.00^{+0.10}_{-0.07}$	$3.30^{+0.16}_{-0.16}$	54^{+6}_{-6}	$2.83^{+0.05}_{-0.05}$	0.32
33	PG 1209+263	$3.66^{+0.08}_{-0.08}$	$3.80^{+0.19}_{-0.18}$	210^{+9}_{-9}	$2.45^{+0.05}_{-0.05}$	0.24
34	PG 1332+137	$5.44^{+0.10}_{-0.10}$	$3.40^{+0.16}_{-0.17}$	46^{+5}_{-6}	$2.95^{+0.05}_{-0.05}$	0.27
35	PG 1511+367	$4.8^{+0.4}_{-0.4}$	$3.0^{+0.4}_{-0.4}$	53^{+13}_{-24}	$2.75^{+0.14}_{-0.14}$	0.18
36	PG 1533+467	$6.3^{+0.5}_{-0.5}$	$3.7^{+0.5}_{-0.5}$	$34^{+\ 8}_{-13}$	$3.17^{+0.14}_{-0.14}$	0.38
37	PG 2219+094	$7.1^{+0.5}_{-0.6}$	$6.9^{+0.8}_{-0.7}$	$51^{+14}_{-\ 5}$	$3.66^{+0.10}_{-0.09}$	0.48
38	PG 2229+099	$6.17^{+0.15}_{-0.14}$	$4.67^{+0.22}_{-0.22}$	$50.5^{+1.9}_{-1.9}$	$3.24^{+0.05}_{-0.05}$	0.00
39	PHL 159	$8.22^{+0.16}_{-0.15}$	$4.53^{+0.22}_{-0.21}$	$21.2^{+1.0}_{-1.5}$	$3.61^{+0.05}_{-0.05}$	0.05
40	PHL 2018	$7.42^{+0.14}_{-0.53}$	$5.77^{+0.29}_{-0.31}$	$40.1^{+7.9}_{-1.2}$	$3.56^{+0.05}_{-0.05}$	0.49
41	PHL 346	$9.05^{+0.28}_{-0.21}$	$6.06^{+0.29}_{-0.30}$	$23.2^{+1.0}_{-0.7}$	$3.86^{+0.05}_{-0.05}$	0.07

Table 4: Masses M, radii R, luminosities L, evolutionary ages $\tau_{\rm evol}$ and stellar rotation $\Omega/\Omega_{\rm c}$ of the target stars.

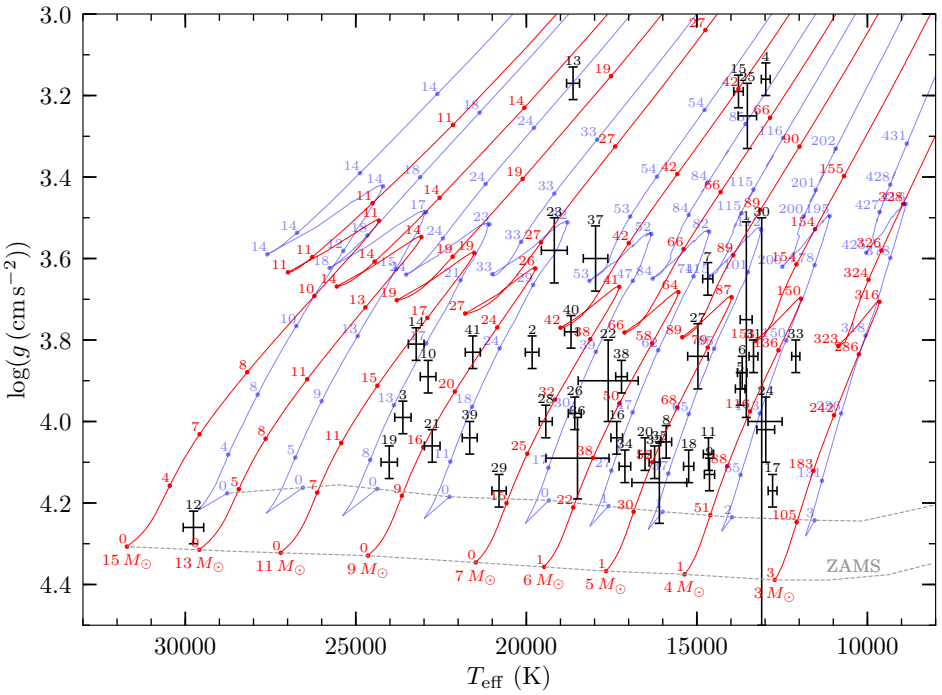

Figure 8: Suface gravities $\log(g)$ vs. effective temperatures $T_{\rm eff}$ of the target stars, which are labeled according to Table 1. Overplotted in red are non-rotating evolutionary tracks (Georgy et al. 2013) of B-type stars of masses between $3\,M_\odot$ and $15\,M_\odot$ and metallicity $z = 0.014$. The zero-age main-sequence (ZAMS) is plotted as a gray dashed line. For reference evolutionary tracks at 95 % critical rotation of the same metallicity and masses are shown in light blue. Red and blue numbers denote the evolutionary ages at the given points of the tracks. The end of the core hydrogen burning phase is at the kink like feature of the tracks. The tracks show that rotating stars are younger and more massive than non-rotating stars with the same atmospheric parameters.

4.5. Peculiar Spectra

PHL 346 is known to be a β Cep pulsator and has already been studied for example by Handler et al. (2019). Such β Cep stars are variable stars that rapidly change in brightness due to pulsations of their surfaces. These pulsations also affect the optical spectra, as they can change the strengths and shapes of metal lines. Due to the relative motion of the stellar surface when shrinking or expanding, the cores of metal lines may experience slight red- or blue-shifts, resulting in asymmetric shapes of the lines. We are able to observe such varying metal lines in our spectra and an example is plotted in Figure 9. The two subplots show the same lines in different observations and the model spectra (red) that were fit to the observations are identical in both cases. While in the top panel the spectral lines are quite asymmetric with slightly blue-shifted cores, in the

bottom panel the lines are overall stronger and seem more symmetric, especially in the case of the two marked Si III and the S II line.

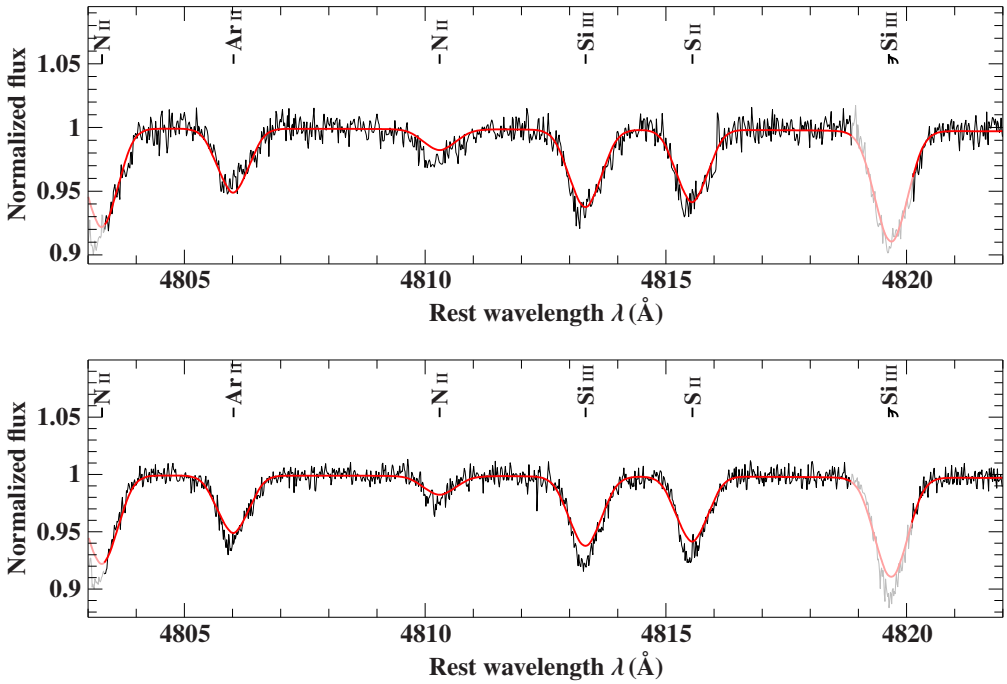

Figure 9: Variations of metal line profiles in the spectra of PHL 346.

We also observe similar line variations in the spectra of EC 20252−3137. Again, an example is plotted in Figure 10 for two different observations and the model spectra are also identical in both subplots. In the observation plotted in the top panel, the N II lines have slightly asymmetric and red-shifted line cores, while the same lines are weaker and more symmetric in the bottom panel. This hints towards a pulsating nature of EC 20252−3137, which seems to be unknown to this date as we were unable to find any literature discussing any kind of variability of this star.

Another star showing peculiar spectral features is PG 1209+263. We observe a lot of spectral lines that are not covered by our synthetic model grids (see Figure 11) and might stem form heavier elements. Additionally the strength of some spectral lines varies over the different spectra. An example is the Si II line at about 4620 Å shown in Figure 11 for two different observations. Thus the star does not only seem to be chemically peculiar but also shows pulsations. The latter is supported by the fact, that the star appears in the Catalina Surveys Catalog of periodic variable stars (Drake et al. 2014) under the identifier CRTS J121213.2+260000. Since we are unable to properly model the stars peculiar spectral features and it is a variable star, our atmospheric parameters should be considered as preliminary and a detailed follow up analysis should be carried out to derive more reliable results.

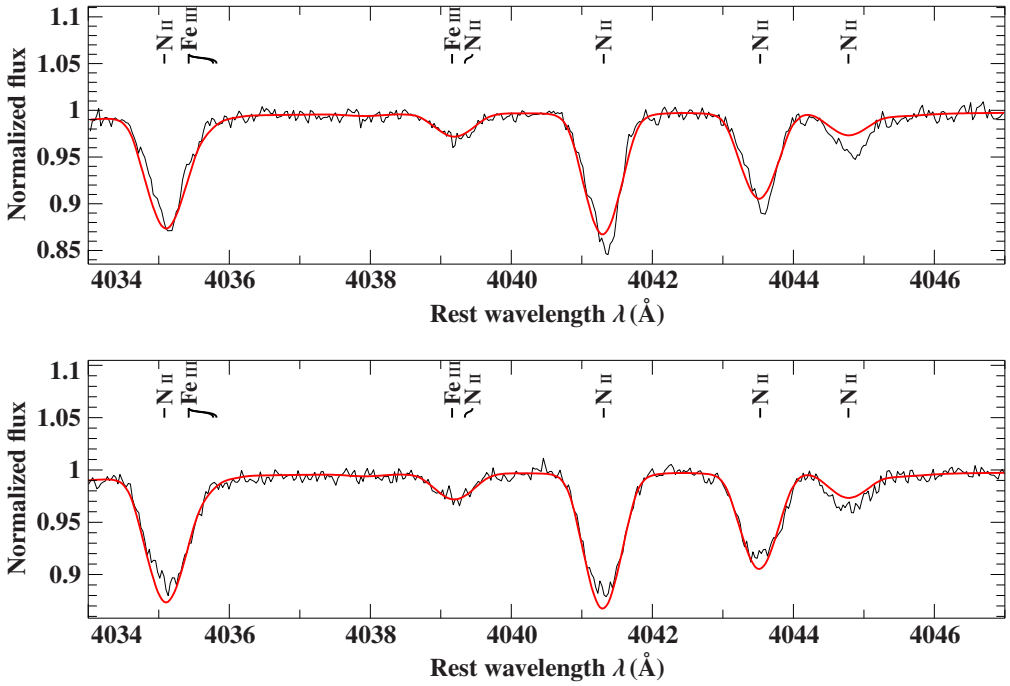

Figure 10: Variations of metal line profiles in the spectra of EC 20252−3137.

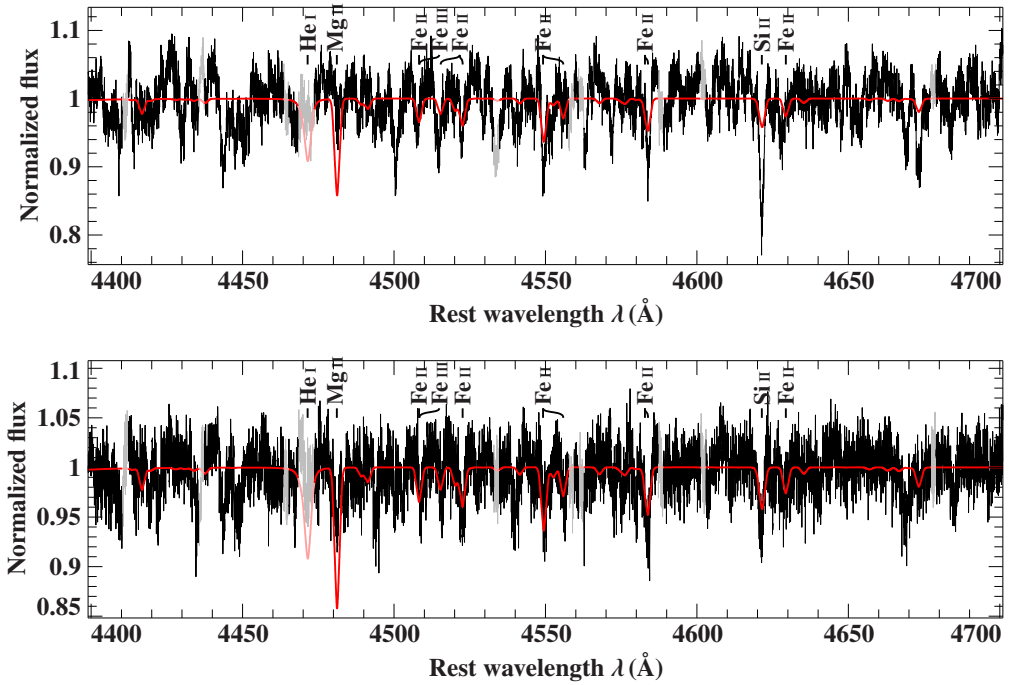

Figure 11: Excerpt of the spectral fit of PG 1209+263 with features not covered by our synthetic spectra.

4.6. Comparison to Silva & Napiwotzki (2011)

For the subgroup of our target sample that was also analyzed by Silva & Napiwotzki (2011), we plot a comparison between our spectroscopic results to the ones used by Silva & Napiwotzki (2011) in Figure 12. This comparison includes the effective temperature $T_{\rm eff}$, the surface gravity $\log(g)$, the projected rotational velocities $v\sin(i)$ and the radial velocity $v_{\rm rad}$. For the majority of stars, our parameters agree within the 2σ uncertainties and overall we are able to reduce the uncertainties compared to the ones from Silva & Napiwotzki (2011), with the exceptions of BD +20 3004 and PG 0914+001 for which our uncertainties on $\log(g)$ are larger since we had to purely rely on photometric data to derive atmospheric parameters as no spectra were available for those two stars, as discussed above.

The few cases for which our parameters differ by more than 2σ are not surprising, however, since the quality of the data of Silva & Napiwotzki (2011) is quite inhomogeneous as they mostly compile the parameters from various different studies from the literature. These studies are very different from one another in terms of their analysis methods but also the quality of the analyzed data and the models used for the analyses vary.

For the projected rotational velocities Silva & Napiwotzki (2011) do not consider uncertainties, thus the residuals plotted in Figure 12 in this incidence are only based on our uncertainties, which are small due to the high quality of the analyzed spectra. Thus there are some outliers with high residuals, however the vast majority of our values are comparable to the ones of Silva & Napiwotzki (2011). While our radial velocities are very similar to the values of Silva & Napiwotzki (2011) for almost all stars, there is one extreme outlier, EC 19596−5356, with a radial velocity of $v_{\rm rad} = -202.6 \pm 0.3\,{\rm kms}^{-1}$ from our analysis but $v_{\rm rad} = 200 \pm 15\,{\rm kms}^{-1}$ in Silva & Napiwotzki (2011). In this particular case it is evident that the minus sign got lost in Silva & Napiwotzki (2011).

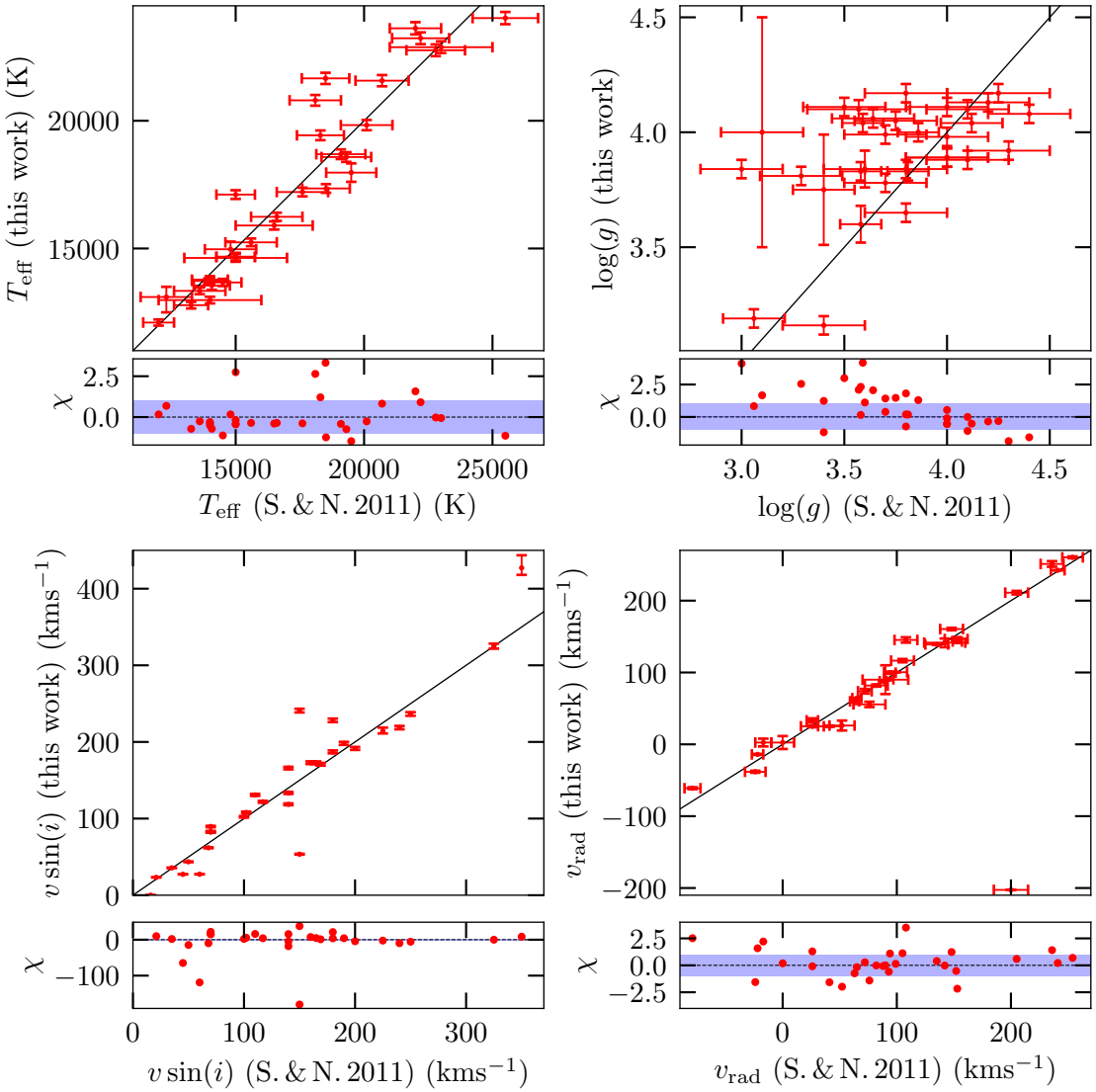

Figure 12: Comparison of effective temperatures $T_{\rm eff}$, surface gravities $\log(g)$, projected rotational velocities $v \sin(i)$ and radial velocities $v_{\rm rad}$ of our spectroscopic analysis to the values used by Silva & Napiwotzki (2011). The identity line is shown in all subplots. Residuals χ are plotted and the interval $-1 \leq \chi \leq 1$ is marked in blue.

5. Derivation of spectrophotometric distances

As pointed out in Section 3, there are some stars in our sample that have quite uncertain or even negative parallaxes that are of no help for a kinematic analysis. Thus, we have to rely on an independent distance estimate and do so by deriving spectrophotometric distances for all our target stars.

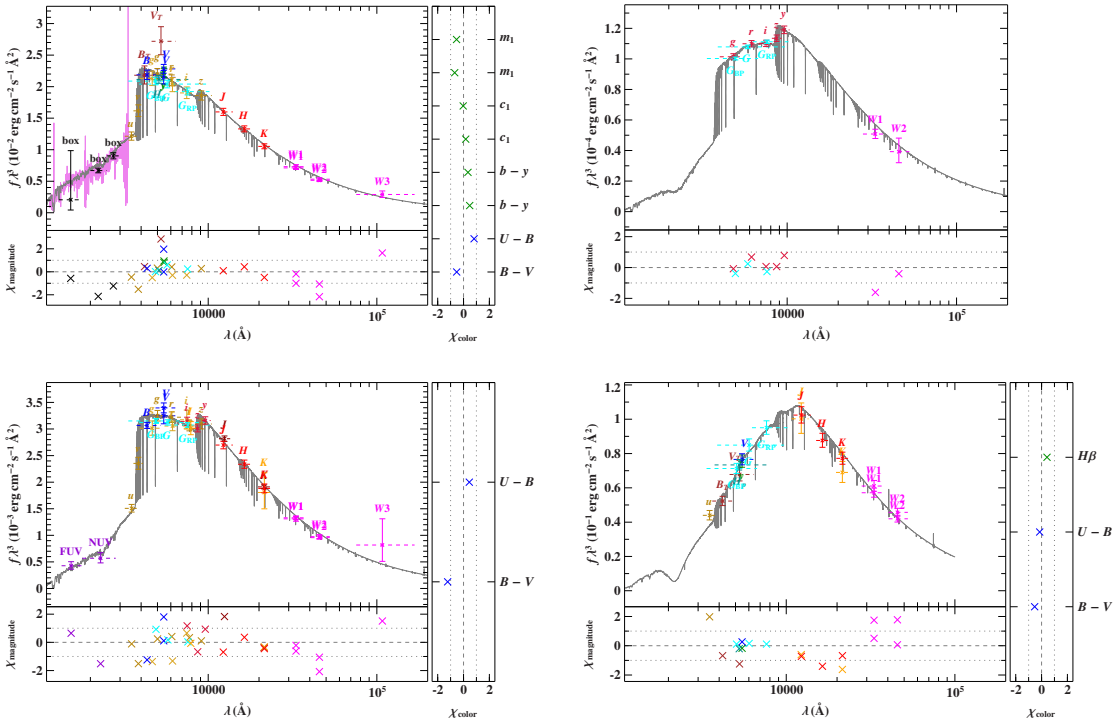

Figure 13: Photometric fits of HIP 55461, LAMOST-HVS4, EC 04420−1908 and HD 151397. The synthetic SEDs are plotted in gray and photometric data is displayed in various colors. IUE spectra are overplotted in magenta if available. Residuals in magnitude and color are plotted in the bottom and right panels, respectively.

We calculate synthetic spectral energy distributions (SEDs) and colors using the atmospheric parameters obtained from our spectroscopic analysis in Section 4 using the ATLAS12 code and compare them to photometric measurements. The photometric data usually covers the infrared, optical and ultraviolet range and is compiled from a variety of surveys using the VizieR catalog access tool (https://vizier.u-strasbg.fr/viz-bin/VizieR). In the photometric fitting routine we are left with two free parameters, namely the angular diameter Θ as a distance scaling factor and the color excess $E(44-55)$, which is an indicator for interstellar reddening and extinction. We make use of the extinction curve by Fitzpatrick et al. (2019) and keep the extinction parameter fixed at $R_{55} = 3.02$, the value for the interstellar medium. For BD +20 3004 and PG 0914+001, for which no spectra were available, the photometric coverage was suf-

#	Object	$E(44-55)$ (mag)	$\log(\Theta)$	$\delta_{\rm excess}$ (mag)	$d_{\rm spec}$ (kpc)
1	BD +20 3004	$0.006^{+0.006}_{-0.006}$	$-9.9616^{+0.0027}_{-0.0028}$	0.009	$1.8^{+0.6}_{-0.5}$
2	BD −15 115	$0.011^{+0.004}_{-0.004}$	$-10.254^{+0.004}_{-0.004}$	0.031	$4.57^{+0.22}_{-0.22}$
3	BD −2 3766	$0.063^{+0.004}_{-0.004}$	$-10.163^{+0.004}_{-0.004}$	0.02	$3.46^{+0.17}_{-0.17}$
4	EC 04420−1908	$0.037^{+0.004}_{-0.004}$	$-10.5416^{+0.0029}_{-0.0028}$	0.013	$17.0^{+0.9}_{-0.8}$
5	EC 09452−1403	$0.044^{+0.006}_{-0.006}$	$-10.685^{+0.004}_{-0.004}$	0.024	$8.1^{+0.4}_{-0.4}$
6	EC 10087−1411	$0.065^{+0.007}_{-0.007}$	$-9.933^{+0.004}_{-0.004}$	0.034	$1.52^{+0.08}_{-0.08}$
7	EC 10500−1358	$0.027^{+0.005}_{-0.005}$	$-10.4138^{+0.0030}_{-0.0030}$	0.024	$6.42^{+0.33}_{-0.30}$
8	EC 19596−5356	$0.033^{+0.006}_{-0.006}$	$-10.861^{+0.004}_{-0.004}$	0.029	$11.5^{+0.6}_{-0.6}$
9	EC 20104−2944	$0.083^{+0.005}_{-0.005}$	$-10.501^{+0.004}_{-0.004}$	0.024	$4.17^{+0.20}_{-0.20}$
10	EC 20252−3137	$0.097^{+0.008}_{-0.008}$	$-10.144^{+0.006}_{-0.006}$	0.057	$3.70^{+0.18}_{-0.18}$
11	EC 23169−2235	$0.0000^{+0.0024}_{-0.0000}$	$-10.4120^{+0.0036}_{-0.0025}$	0.015	$3.67^{+0.17}_{-0.18}$
12	HD 151397	$0.462^{+0.008}_{-0.008}$	$-9.908^{+0.005}_{-0.005}$	0.044	$1.66^{+0.08}_{-0.08}$
13	HD 271791	$0.054^{+0.005}_{-0.005}$	$-10.486^{+0.004}_{-0.004}$	0.019	$19.6^{+1.0}_{-1.0}$
14	HIP 105912	$0.098^{+0.006}_{-0.006}$	$-9.850^{+0.005}_{-0.005}$	0.037	$2.12^{+0.11}_{-0.10}$
15	HIP 108215	$0.0000^{+0.0007}_{-0.0000}$	$-9.659^{+0.004}_{-0.004}$	0.026	$2.21^{+0.12}_{-0.11}$
16	HIP 114569	$0.0000^{+0.0012}_{-0.0000}$	$-9.984^{+0.004}_{-0.004}$	0.017	$1.64^{+0.08}_{-0.08}$
17	HIP 11809	$0.009^{+0.006}_{-0.006}$	$-10.293^{+0.004}_{-0.004}$	0.043	$2.25^{+0.11}_{-0.11}$
18	HIP 55461	$0.015^{+0.005}_{-0.005}$	$-10.202^{+0.004}_{-0.004}$	0.03	$2.24^{+0.11}_{-0.11}$
19	HIP 56322	$0.0099^{+0.0030}_{-0.0030}$	$-10.174^{+0.004}_{-0.004}$	0.011	$3.10^{+0.15}_{-0.15}$
20	HIP 60350	$0.005^{+0.007}_{-0.005}$	$-10.334^{+0.004}_{-0.004}$	0.034	$3.35^{+0.16}_{-0.16}$
21	HIP 70275	$0.033^{+0.004}_{-0.004}$	$-10.048^{+0.004}_{-0.004}$	0.018	$2.30^{+0.11}_{-0.11}$
22	HS 1914+7139	$0.166^{+0.007}_{-0.007}$	$-10.845^{+0.010}_{-0.010}$	0.027	$14.6^{+1.9}_{-1.7}$
23	LAMOST−HVS1	$0.054^{+0.005}_{-0.005}$	$-10.651^{+0.005}_{-0.005}$	0.0	$15.7^{+1.5}_{-1.5}$
24	LAMOST−HVS3	$0.112^{+0.011}_{-0.011}$	$-11.194^{+0.008}_{-0.008}$	0.022	$22.1^{+2.1}_{-2.1}$
25	LAMOST−HVS4	$0.137^{+0.007}_{-0.007}$	$-11.237^{+0.006}_{-0.006}$	0.0	74^{+8}_{-8}
26	PB 5418	$0.068^{+0.005}_{-0.005}$	$-10.495^{+0.004}_{-0.004}$	0.018	$6.10^{+0.29}_{-0.29}$
27	PG 0009+036	$0.043^{+0.005}_{-0.005}$	$-10.585^{+0.005}_{-0.005}$	0.027	$7.8^{+0.8}_{-0.8}$
28	PG 0122+214	$0.037^{+0.007}_{-0.007}$	$-10.616^{+0.004}_{-0.004}$	0.029	$8.1^{+0.4}_{-0.4}$
29	PG 0855+294	$0.009^{+0.006}_{-0.006}$	$-10.540^{+0.004}_{-0.004}$	0.024	$5.76^{+0.28}_{-0.27}$
30	PG 0914+001	$0.059^{+0.012}_{-0.017}$	$-10.796^{+0.009}_{-0.006}$	0.043	$7.8^{+4.9}_{-3.0}$
31	PG 0955+291	$0.0000^{+0.0019}_{-0.0000}$	$-10.535^{+0.004}_{-0.004}$	0.0	$6.32^{+0.30}_{-0.30}$
32	PG 1205+228	$0.0000^{+0.0029}_{-0.0000}$	$-10.214^{+0.004}_{-0.004}$	0.03	$2.44^{+0.12}_{-0.12}$
33	PG 1209+263	$0.009^{+0.007}_{-0.007}$	$-10.814^{+0.005}_{-0.005}$	0.051	$11.2^{+0.6}_{-0.6}$
34	PG 1332+137	$0.000^{+0.002}_{-0.000}$	$-10.402^{+0.004}_{-0.004}$	0.034	$3.87^{+0.18}_{-0.19}$
35	PG 1511+367	$0.012^{+0.008}_{-0.008}$	$-10.424^{+0.012}_{-0.011}$	0.04	$3.6^{+0.5}_{-0.5}$
36	PG 1533+467	$0.023^{+0.009}_{-0.009}$	$-10.217^{+0.011}_{-0.011}$	0.046	$2.8^{+0.4}_{-0.4}$
37	PG 2219+094	$0.049^{+0.006}_{-0.006}$	$-10.406^{+0.005}_{-0.005}$	0.022	$7.9^{+0.9}_{-0.8}$
38	PG 2229+099	$0.069^{+0.005}_{-0.005}$	$-10.641^{+0.004}_{-0.004}$	0.007	$9.2^{+0.5}_{-0.5}$
39	PHL 159	$0.066^{+0.005}_{-0.005}$	$-10.231^{+0.004}_{-0.004}$	0.026	$3.48^{+0.17}_{-0.17}$
40	PHL 2018	$0.004^{+0.006}_{-0.004}$	$-10.413^{+0.004}_{-0.004}$	0.033	$6.7^{+0.4}_{-0.4}$
41	PHL 346	$0.062^{+0.005}_{-0.005}$	$-10.375^{+0.004}_{-0.004}$	0.03	$6.5^{+0.4}_{-0.4}$

Table 5: Results of the photometric analysis: the color excess $E(44-55)$, the angular diameter Θ, the generic excess noise $\delta_{\rm excess}$ and the spectrophotometric distance $d_{\rm spec}$.

ficient to also use the effective temperature and surface gravity as free parameters in the photometric analysis and still recover quite well constrained results. Examples of a photometric fit are plotted in Figure 13, where the subplots in the top row demonstrate examples of good and bad photometric coverage (HIP 55461 and LAMOST-HVS4) and the bottom row compares the shapes of the SEDs for low and high effective temperatures (EC 04420−1908 and HD 151397). The photometric fits of BD +20 3004 and PG 0914+001 are plotted in Figure B.20 and Figure B.21, respectively. The results of the photometric analysis of the stars are listed in Table 5. If the reduced χ^2 value of the fit is larger than 1, a generic uncertainty – the so called generic excess noise δ_{excess} – is added in quadrature to the uncertainties of the photometric data. For acceptable fits the excess noise should be $\lesssim 0.05$ mag, which is the case for all our target stars. Because the stars are located at high galactic latitudes, interstellar reddening is small, except for HD 151397, which lies in the Galactic plane. By making use of the definition of the angular diameter $\Theta = 2R/d$, we can now calculate spectrophotometric distances by combining the stellar radii obtained in Section 4 with the angular diameters obtained from the photometric analysis. The resulting distances are also listed in Table 5.

We can now crosscheck our spectrophotometric distances by comparing them to distance estimates obtained from the *Gaia* EDR3 parallaxes. The parallaxes can be easily converted to a distance estimate by simply inverting them. Since most of our stars are located at a few kpc from the sun, representing the distance estimate from the parallax via the median may be misleading, as inverting a Gaussian distribution close to zero will result in a highly skewed distribution. We therefore carry out a Monte Carlo simulation to convert parallaxes to distances by sampling the parallaxes according to their uncertainties as a Gaussian distribution and inverting each of the 1 million sampled values individually. We then calculate the distance estimate from the resulting distribution as the mode, i.e. the most likely value of the distribution, and determine the uncertainties as the edges of the high density interval containing 68% of the distribution.

Lindegren et al. (2020) determine that the parallax zero-point is not exactly at $\varpi = 0$, instead, there is a global parallax zero-point of $\varpi_0 = -17\,\mu$as, determined from the parallax distribution of Quasars. Furthermore, they suspect that the parallax zero-point of an individual source depends on at least its magnitude, color and ecliptic latitude. Therefore, they provide a way to calculate this individual zero-point for each source separately, but state that this method "should be considered as provisional and indicative" and "[u]sers are urged to make their own judgement [...]". Thus, we also derive distance estimates from the parallaxes using the global zero-point, as well as individually calculated zero-points for every star (see Table 1).

In Figure 14 we compare our spectrophotometric distances d_{spec} to the distance estimates from the *Gaia* EDR3 parallaxes in the three cases of no correction, global zero-point correction by $-17\,\mu$as and individual zero-point correction, for stars where the relative uncertainty of the parallax is 30% or better. In the first case, i.e. the left panel, the data points scatter nicely around the identity line, and our spectrophotometric distances agree with the parallaxes within 2σ. Although there are slightly more stars with positive residuals than negative ones, the inequality is likely still subject to statistical

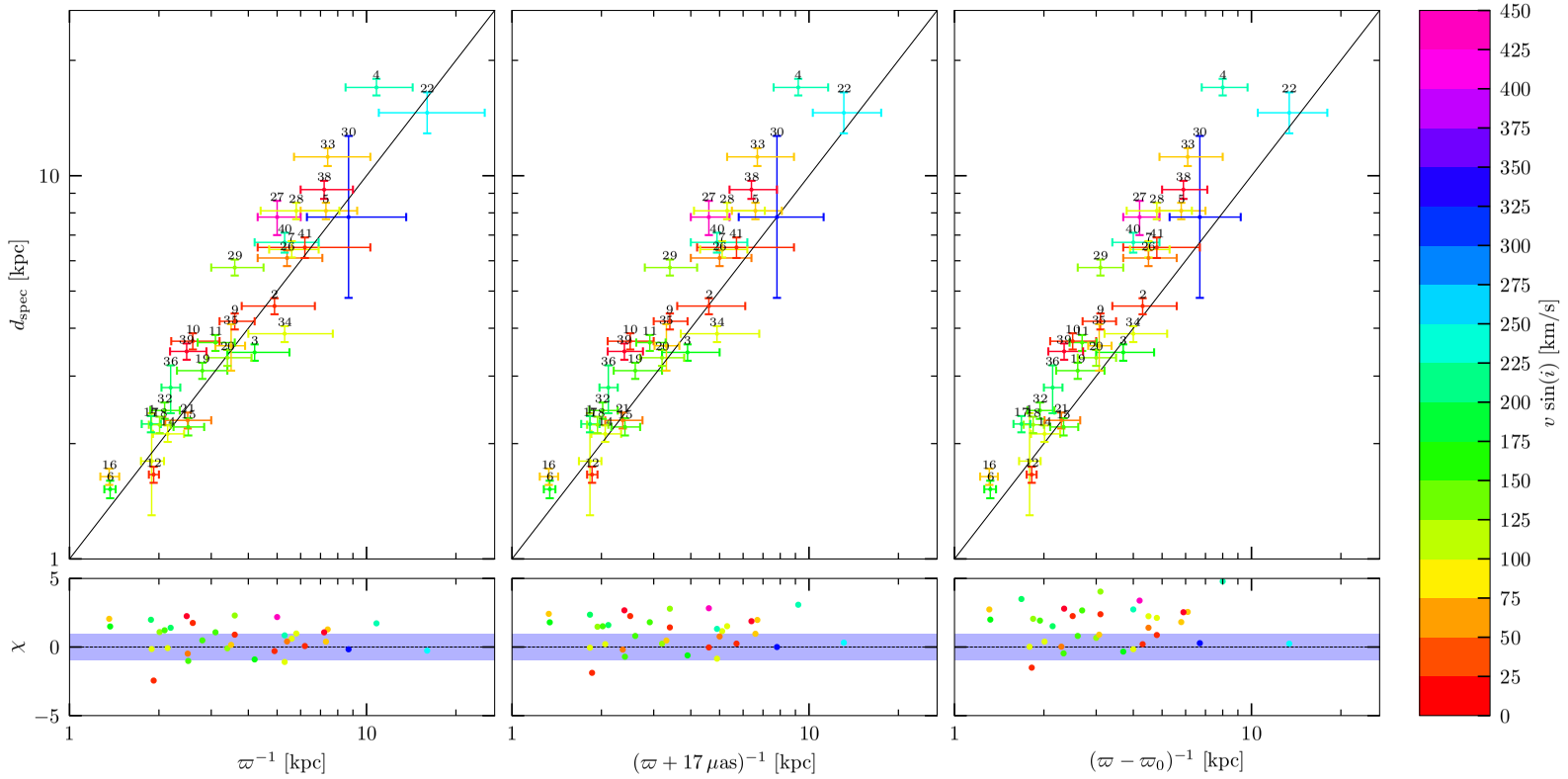

Figure 14: *Top panels:* Comparison of spectrophotometric distances $d_{\rm spec}$ with *Gaia* EDR3 parallaxes ϖ for the three cases of no zero-point offset, global zero-point correction by $-17\,\mu$as and individual zero-point correction ϖ_0. The identity line is marked in black. *Bottom panels:* Residual plots. The blue shaded area marks residuals of $-1 < \chi < 1$. The data points are color-coded according to the projected rotational velocity $v \sin(i)$ and labeled for better identification.

scatter. Furthermore, there is a handfull of stars with high projected rotational velocities $v \sin(i) \geq 200\,\mathrm{kms}^{-1}$ that we most likely see equator on. Due to the fast rotation, these stars may have ellipsoidal shape with an increased stellar radius at the equator compared to the poles. This way the obtained spectra will be dominated by the equatorial part of the star and the surface gravity from our spectral analysis may be slightly underestimated compared to the surface averaged surface gravity of the star. A result of this underestimation of $\log(g)$ is a slight overestimation of the spectrophotometric distance. This may also explain the small overabundance of stars at residuals χ between 1 and 2.

In the case of the global zero-point correction in the middle panel, the residuals are slightly more shifted towards positive values compared to the left panel. Thus, when taking the global parallax zero-point into account, the agreement of our spectrophotometric distances with the parallaxes is not as good. Some cases of the stars with predominantly high residuals may again be explained by the fast rotation of some of the stars. However, also a majority of the slowly rotating stars is above $\chi = 0$. There are two possible reasons to explain this small discrepancy. On the one hand, we might generally underestimate the surface gravity and/or overestimate the mass of our stars slightly, which would lead to a slight overestimation of the distances. On the other hand, the global zero-point of the *Gaia* parallaxes may be overestimated for our blue target stars, leading to smaller distance estimates from the parallaxes. We believe the latter is especially the case for the individual parallax zero-point correction, as demonstrated in the right panel of Figure 14. Only few of our spectrophotometric distances agree with the parallaxes within their 1σ uncertainties in this case. This observation further endorses the suggestion of Lindegren et al. (2020) to use the individually tailored parallax zero-points with care.

In order to clarify the issues stated above, a future project to compare parallaxes and spectrophotometric distances of a larger sample of stars with an increased distribution of distances may be worthwhile. Figure 14 may even point to a slightly positive zero-point offset for blue stars. Forthcoming analyses and the next *Gaia* data release will clarify this issue.

For the majority of stars in our sample the relative uncertainties on our spectrophotometric distances are better than the ones of the distance estimates obtained from the *Gaia* parallaxes. We therefore use our spectrophotometric distances for the kinematic analysis of our stars, unless the parallax of a star yields a more precise distance. The latter is the case for BD +20−3004, EC 10087−1411, HD 151397, PG 0914+001, PG 1511+367 and PG 1533+467, the more so since we had to rely on photometry to determine the atmospheric parameters of BD +20−3004 and PG 0914+001, meaning for those stars we use the *Gaia* EDR3 parallaxes instead.

6. Kinematic analysis

For the kinematic analysis of our sample of runaway stars we use the GALPY package (Bovy 2015, http://github.com/jobovy/galpy) for PYTHON to trace back in time the stars' orbits to the Galactic plane. We calculate the positions of disk intersection (x_p, y_p) as well as the ejection velocities $v_\mathrm{ej,p}$ from these positions and the times of flight $\tau_\mathrm{flight,p}$ to the stars' current locations.

6.1. Galactic potential and orbit integration

Using the astrometric data, i.e. current position and velocity, of a star, GALPY numerically integrates the equations of motion in a given Galactic gravitational potential to calculate the orbit. As the Galactic potential we use Model I of Irrgang et al. (2013), which is a revised version of the widely used potential of Allen & Santillan (1991). Model I is the sum of a spherical bulge

$$\Phi_\mathrm{b}(R) = -\frac{M_\mathrm{b}}{\sqrt{R^2 + b_\mathrm{b}^2}},$$

an axisymmetric disk

$$\Phi_\mathrm{d}(r,z) = -\frac{M_\mathrm{d}}{\sqrt{r^2 + \left(a_\mathrm{d} + \sqrt{z^2 + b_\mathrm{d}^2}\right)^2}},$$

and a spherical dark matter halo

$$\Phi_\mathrm{h}(R) = \begin{cases} \frac{M_\mathrm{h}}{a_\mathrm{h}} \left(\frac{1}{\gamma-1} \ln \left(\frac{1+\left(\frac{R}{a_\mathrm{h}}\right)^{\gamma-1}}{1+\left(\frac{\Lambda}{a_\mathrm{h}}\right)^{\gamma-1}} \right) - \frac{\left(\frac{\Lambda}{a_\mathrm{h}}\right)^{\gamma-1}}{1+\left(\frac{\Lambda}{a_\mathrm{h}}\right)^{\gamma-1}} \right) & \text{if } R < \Lambda, \\ -\frac{M_\mathrm{h}}{R} \frac{\left(\frac{\Lambda}{a_\mathrm{h}}\right)^{\gamma}}{1+\left(\frac{\Lambda}{a_\mathrm{h}}\right)^{\gamma-1}} & \text{otherwise,} \end{cases}$$

with the spherical radius R, the cylindrical radius r, the weighting factors $M_\mathrm{b}/M_\mathrm{d}/M_\mathrm{h}$ for the contributions of the respective components to the potential, the scale lengths $b_\mathrm{b}/a_\mathrm{d}/b_\mathrm{d}/a_\mathrm{h}$, the cut-off parameter $\Lambda = 200\,\mathrm{kpc}$ and the exponent $\gamma = 2$. The weighting factors and scale lengths were calibrated by fitting the potential of Model I to the observed rotation curve of the Milky Way. For details on the calibration and the potential itself see Irrgang et al. (2013). Although Model I is already implemented in GALPY, only an approximation of the dark matter halo potential is used. We therefore update the exact form of the halo potential and its spatial derivatives and replace GALPY's approximation. The PYTHON code for the halo potential is listed in Appendix C. In GALPY's left-handed coordinate system Model I places the Sun at $(x, y, z) = (8.4, 0, 0)\,\mathrm{kpc}$ and the local standard of rest (LSR) rotates around the Galactic center at a velocity $v_0 = 242\,\mathrm{kms}^{-1}$ at the Sun's galactocentric radius. For the peculiar

motion of the Sun relative to the LSR we adopt $(U, V, W)_\odot = (-11.1, 12.24, 7.25)\,\mathrm{kms}^{-1}$ from Schönrich et al. (2010).

We numerically integrate the stars' orbits for three times their evolutionary age τ_{evol} and compute the coordinates and velocity components at the first disk intersection at $z = 0$. From the velocity components we calculate the Galactic rest-frame velocity at disk intersection $v_{\mathrm{Grf,p}}$, the ejection velocity $v_{\mathrm{ej,p}}$, which is the Galactic rest-frame velocity corrected for the rotation of the Galaxy, and the time of flight $\tau_{\mathrm{flight,p}}$ from disk intersection to the star's current location. In order to obtain uncertainties on the orbital parameters we carry out a Monte Carlo simulation, where we generate 100 000 sets of the input parameters $(\alpha, \delta, \mu_\alpha \cos(\delta), \mu_\delta, d, v_{\mathrm{rad}})$ per star, following Gaussian distributions according to their uncertainties, while also taking into account the correlations between α, δ, $\mu_\alpha \cos(\delta)$ and μ_δ and asymmetric uncertainties on d and v_{rad}. After the integration we then sample the sets of orbital parameters at the current position and the location of disk intersection and determine the mode and the uncertainties from the high density interval containing 68% of the sampled values. By comparing the stars' current velocities in the Galactic rest-frame with the local escape velocity v_{esc}, we derive the probability P_{b} for a star to be bound to the Galaxy as the fraction of orbit instances for which the star's rest-frame velocity does not exceed its local escape velocity. The orbital parameters at the stars' current locations are listed in Table A.1 and the parameters at disk intersection are listed in Table A.2.

6.2. Discussion

6.2.1. Disk intersections and ejection velocities

The positions of disk intersection are well constrained for the majority of the target stars and are plotted in Figure 15. Predominantly, the stars cross the Galactic plane within about 3 kpc of the solar circle and in most cases this position can be narrowed down with a precision of less than 1 kpc. Two stars, PHL 346 (#41) and HIP 108215 (#15), have an origin at small Galactic radii of ∼2.5 kpc and ∼3.5 kpc, respectively, and are thus ejected close to the Galactic bulge. For three stars – LAMOST-HVS4 (#25), PG 0009+036 (#27) and PG 0914+001 (#30) – the places of origins could not be constrained as precisely as for the other stars. Their disk intersections are plotted in the right panel of Figure 15. While LAMOST-HVS4 and PG 0914+001 are ejected most likely from the outer rim of the Galactic disk at ∼18.5 kpc and ∼15 kpc, respectively, the calculated orbits of PG 0009+036 reach the Galactic plane only at a radius $r_{\mathrm{p}} = 60^{+30}_{-20}$ kpc, which is far beyond the extent of the Galactic disk. Thus we cannot consider PG 0009+036 a disk runaway star, as its true spatial origin remains unclear.

Overall the precise *Gaia* EDR3 astrometry is a game changer when it comes to constraining the places of origin of runaway stars. *Gaia*'s improvement on the uncertainties of the disk intersections compared to the pre-*Gaia* era is demonstrated in Figure B.22 in the Appendix for the case of HD 271791. While the 2σ contour of the disk intersection based on *Hipparcos* proper motions covers almost an entire Galactic quadrant beyond the solar circle, the intersections based on the *Gaia* proper motions constrain the star's

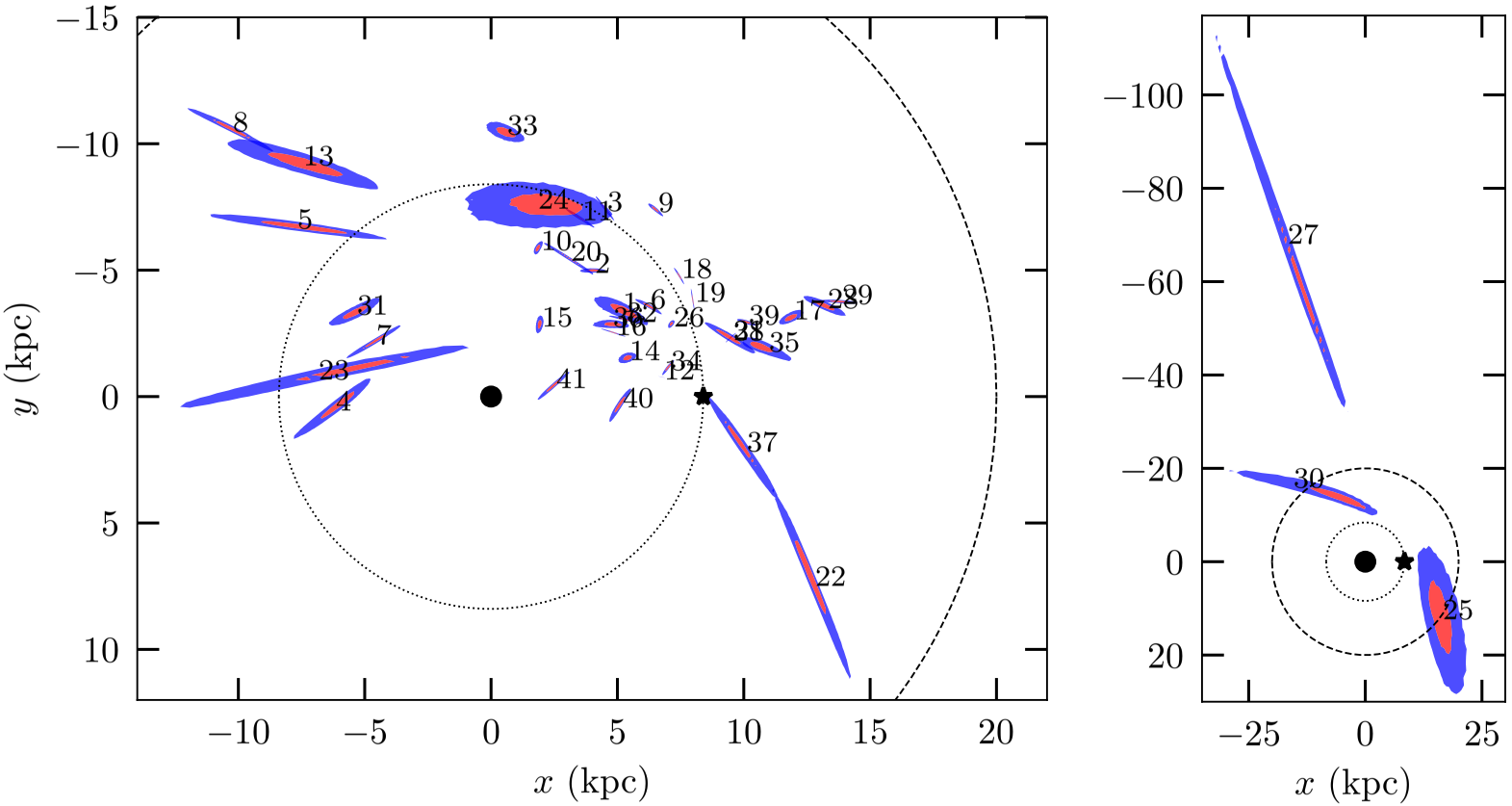

Figure 15: Galactic plane crossing contours of the target stars. The shaded areas mark the 1σ (red) and 2σ (blue) contours. The Galactic center is marked as a black dot and the position of the Sun as a black star. The solar circle (dotted circle, 8.4 kpc) and the edge of the Galactic disk (dashed circle, 20 kpc) are shown for reference.

place of origin to a thin region at a galactocentric radius of ∼12 kpc.

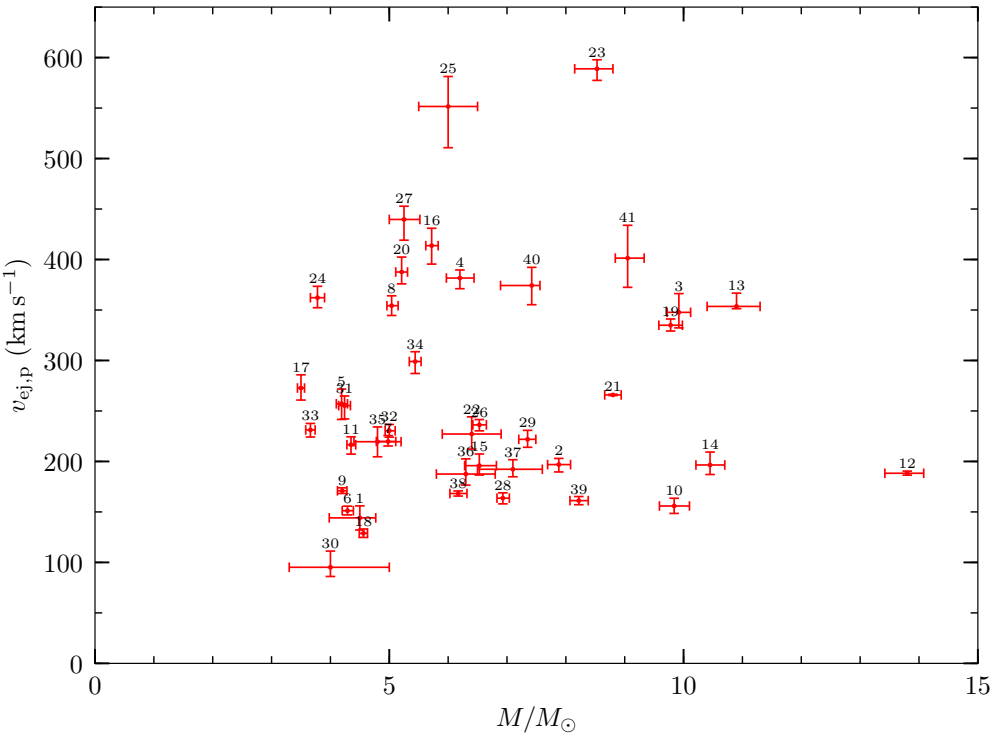

Figure 16: Ejection velocity to mass distribution. Error bars are 1σ uncertainties. The stars are labeled for better identification.

The ejection velocities of the stars are plotted in Figure 16. While the majority of the stars are ejected with velocities below ∼300 kms^{-1}, there are 11 stars with ejection velocities exceeding 350 kms^{-1} within their 1σ uncertainties, excluding PG 0009+036 (#27) for the reasons stated above. In their analysis of 96 runaway stars, Silva & Napiwotzki (2011) observe a gap in the distribution of ejection velocities at about 300 to 400 kms^{-1} and therefore argue for the existence of two separate populations of runaway stars. Although we also observe a small gap at 300 to 350 kms^{-1}, we can neither confirm nor deny this separation due to the relatively low number of stars considered here. To further investigate this issue, a larger target sample would be required to be able to draw further conclusions. It is also worth mentioning that we do not observe a trend of decreasing ejection velocity with stellar mass, although one would expect that the ejection of more massive stars with high velocities should be less likely. Since the majority of stars in our sample was also investigated by Silva & Napiwotzki (2011), we can directly compare our ejection velocities that are based on *Gaia* EDR3 astrometry to the ones from Silva & Napiwotzki (2011) from the pre-*Gaia* era. This comparison is plotted in Figure 17. Again the improved precision of the astrometric data with *Gaia* is directly reflected by the uncertainties on the ejection velocities. While the uncertainties in the analysis of Silva & Napiwotzki (2011) even exceed 100 kms^{-1} for some of the fastest stars,

our uncertainties are significantly lower in general. Also, once precise astrometric data is available, the ejection velocities tend to become less extreme in most cases. Here the most obvious exceptions are EC 04420−1908 (#4) and PG 0009+036 (#27), although our ejection velocity of the latter has to be handled with caution, as PG 0009+036 crosses the Galactic plane far beyond the edge of the disk in our analysis.

The vast majority of our target stars are gravitationally bound to the Milky Way with a probability $P_\mathrm{b} \gtrsim 99\,\%$ (see Table A.1). Since we can rule out the Galactic center as the place of origin for all stars, we are able to classify these bound stars as disk runaways. This includes HIP 60350 and particularly HD 271791, for which the term hyper-runaway star was originally coined, so that they no longer qualify as such. LAMOST-HVS1 and LAMOST-HVS4 on the other hand are two examples of such hyper-runaway stars as they originate in or the latter at the edge of the Galactic disk and are clearly unbound from the Galaxy with bound probabilities of 1.6 % and 0 %, respectively. Furthermore, PG 0009+036 is potentially unbound from the Galaxy with $P_\mathrm{b} = 43.7\,\%$, but we are unable to further classify this star due to its peculiar orbit as discussed above.

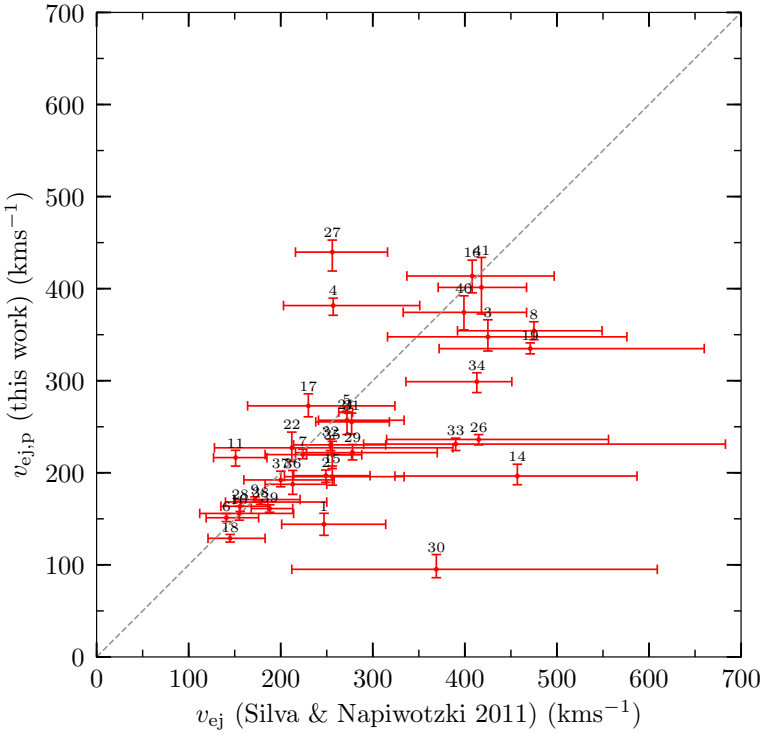

Figure 17: Comparison of our ejection velocities $v_{\mathrm{ej,p}}$ to the ejection velocities v_{ej} from Silva & Napiwotzki (2011) for the stars included in both samples. The dashed identity line is shown for reference.

Since we can rule out the Galactic center as the place of origin for our (hyper-)runaway stars, the only two known ejection scenarios that operate in the disk are the BSS and the

DES. While the two mechanism are capable of ejecting runaway stars with velocities up to $\sim$400 kms^{-1} under the most favourable conditions, the majority of stars are expected to have ejection velocities $\lesssim$ 70 kms^{-1}. While our analysis does not include stars with such low ejection velocities – mainly due to the fact that we selected the more extreme cases and systematic surveys in general favour stars with high radial velocities or proper motions – instead the runaways at the upper end of our ejection velocity distribution, especially above 400 kms^{-1} that is HIP 60350, PHL 346, HIP 114569, LAMOST-HVS1 and LAMOST-HVS4, are a challenge to the classical ejection scenarios. This can be seen as a hint that the extreme cases of disk runaways may be ejected from close encounters with extremely massive stars or even intermediate-mass black holes. This is particularly interesting as no intermediate-mass black holes in the Galactic disk are known to date (Greene et al. 2020).

6.2.2. Flight time vs. age

In order for the hypothesis of ejection from the Galactic disk of the runaway stars to be correct, the times of flight from the position of disk intersection need to be smaller or equal to the stellar evolutionary ages. To verify this, we plot the flight times and stellar ages of our runaways in Figure 18.

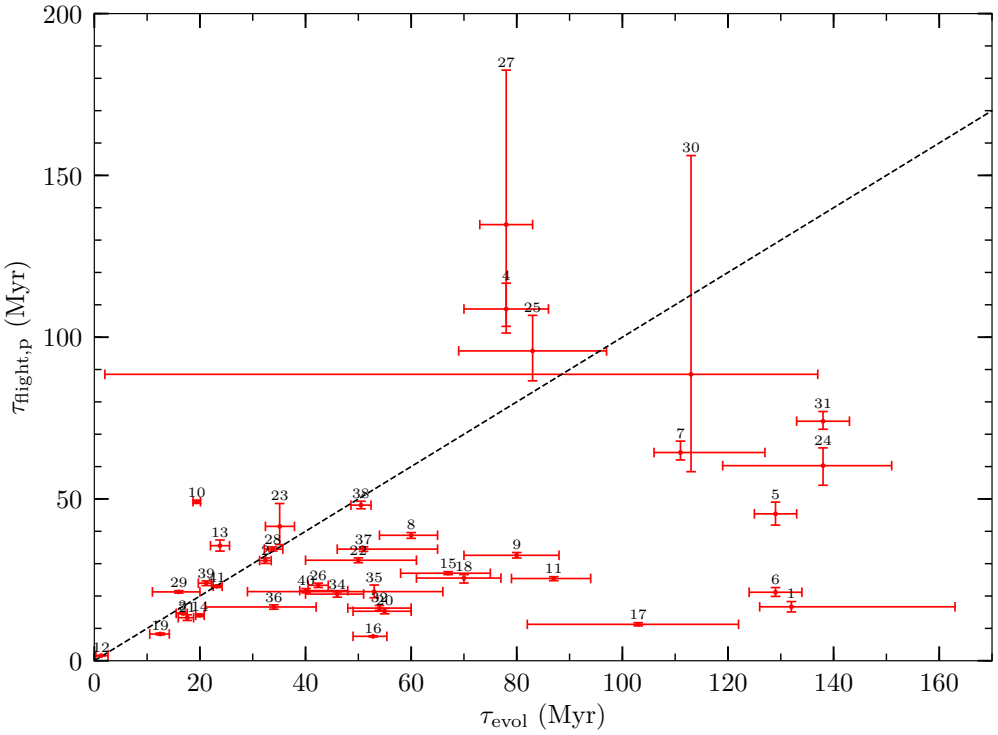

Figure 18: Comparison of the flight times $\tau_{\rm flight,p}$ from the position of disk intersection to the stellar evolutionary ages $\tau_{\rm evol}$ of the sample stars. Uncertainties are of 1σ confidence and stars are labeled for easier identification.

For most of the stars, the flight times are well below the stellar ages. For four stars – HD 151397 (#12), LAMOST-HVS1 (#23), LAMOST-HVS4 (#25) and PG 0122+214 (#28) – the flight times slightly exceed the stellar ages, however the values are still in agreement within their 1σ uncertainties. Similarly, for PG 0009+036 (#27) and PG 0855+294 (#29) the flight times and ages are in agreement within 2σ, although a disk origin for the former has already been ruled out by its position of intersection with the Galactic plane. Furthermore, for PHL 159 (#39), EC 04420−1908 (#4), HD 271791 (#13) and EC 20252−3137 (#10) the two parameters differ by more than 2σ, 3σ, 4σ and 34σ, respectively, and in these cases, the flight times are in tension with the stellar ages. This is especially the case for EC 20252−3137 and there is no doubt that this star cannot stem from the Galactic disk unless the input data were flawed. Since we derive our disk crossing parameters exactly at $z = 0$ and do not account for the finite thickness of the disk, the tension reflected in our results for the three former stars might in reality not be as severe as they theoretically could have been ejected slightly above the Galactic plane. In these cases the slight tension might be resolved with new astrometric data from future *Gaia* data releases and a more realistic treatment of the non-zero disk height. However, this correction will be very small for most stars. Such tensions between stellar age and flight time might however be resolved if the stars can be assigned to the binary supernova ejection channel. In this case the runaway may have gone through a phase of mass transfer in a close binary system before ejection, leading to a rejuvenation making the star appear younger after the mass accretion. This is likely the case for HD 271791 for which the abundance pattern hints to an ejection via the BSS (see Przybilla et al. 2008).

7. Summary and Outlook

Using high resolution optical UVES (mostly provided by Dr. Roberto Raddi) and FEROS spectra and low-resolution LAMOST spectra form the ESO and LAMOST archives, we carry out a quantitative spectrophotometric analysis of 41 candidate runaway stars to derive atmospheric parameters and radial velocities and compare the results to evolutionary models of main-sequence stars of spectral type B to compute stellar masses and ages. From a photometric analysis we obtain the angular diameters of the stars and combined with the masses and surface gravities we are able to derive spectrophotometric distances. We complement the distances and radial velocities with astrometric data from the early data release 3 of the *Gaia* mission of unprecedented precision to numerically compute stellar trajectories in the Galactic gravitational potential of Model I from Irrgang et al. (2013). From the trajectories we derive the stars' positions of intersection with the Galactic disk and calculate kinematic properties such as ejection velocities from the disk and flight times from the positions of ejection to the stars' current locations.

We are able to rule out the Galactic center as the place of origin for all our target stars and instead find that the vast majority of the stars is ejected near the solar circle. The trajectory of PG 0009+036 is quite unusual as it reaches out to large Galactic radii and intersects the Galactic plane at a radius of about 60 kpc, which greatly exceeds the outer edge of the Galactic disk. By comparing the times of flight from the disk to the stellar evolutionary ages, we find a slight tension with the scenario of disk ejection for three stars. For one additional star, EC 20252−3137, the flight time exceeds the stellar age by more than 34σ and thus it can not originate in the Galactic disk. Two stars, LAMOST-HVS1 and LAMOST-HVS4, are unbound from the Galaxy and are thus classified as hyper-runaway stars. The remaining 37 stars are gravitationally bound to the Milky Way and can be classified as runaway stars, including the two former hyper-runaway stars HIP 60350 and HD 271791.

While the two classical disk ejection scenarios, i.e. the binary supernova scenario (BSS) and the dynamical ejection scenario (DES), are capable of accelerating runaway stars to velocities of $\sim$400 kms^{-1} in the most favourable cases and can thus be responsible for the ejection of most stars in our sample, our most extreme stars with ejection velocities above 400 kms^{-1} pose a challenge to the classical mechanisms. This is in particular the case for the two hyper-runaway stars in our sample. Consequently ejection scenarios involving dynamical interactions with extremely massive stars or even intermediate-mass black holes may be at play. The latter scenario is particularly interesting as no intermediate-mass black holes are known yet in the Galactic disk (Greene et al. 2020).

A general trend of decreasing ejection velocities can be observed once precise astrometric data is available, as shown by the comparison with results from Silva & Napiwotzki (2011). Astrometric data with a further increase in precision from future data release of *Gaia* may bring new insights for the kinematics of runaway stars. Furthermore, a detailed abundance analysis of the program stars can be carried out to possibly assign particularly the less extreme runaways to the two classical ejection scenarios.

Acknowledgements

I would like to thank my supervisor Uli Heber for the opportunity to write this thesis at the Remeis-Observatory and his immense support. I want to thank Andreas Irrgang for providing and explaining his ISIS-scripts as well as the insightful discussions. A special thanks to Roberto Raddi for providing his UVES spectra for the analysis. A big thanks to the admins for taking care of the Remeis cluster and keeping the machines running, and to my office-mates and all other members of the Remeis-Observatory for the positive working atmosphere.

This work is based on observations collected at the European Southern Observatory under programs 0102.D-0388, 088.A-9003, 088.D-0064, 091.C-0713, 091.D-0061, 093.D-0302, 383.D-0909, 67.D-0010. This work makes use of the Guoshoujing Telescope (the Large Sky Area Multi-Object Fiber Spectroscopic Telescope LAMOST, Cui et al. 2012) and is a National Major Scientific Project built by the Chinese Academy of Sciences. Funding for the project has been provided by the National Development and Reform Commission. LAMOST is operated and managed by the National Astronomical Observatories, Chinese Academy of Sciences. This work has made use of data from the European Space Agency (ESA) mission *Gaia* (https://www.cosmos.esa.int/gaia), processed by the *Gaia* Data Processing and Analysis Consortium (DPAC, https://www.cosmos.esa.int/web/gaia/dpac/consortium). Funding for the DPAC has been provided by national institutions, in particular the institutions participating in the *Gaia* Multilateral Agreement. Based on observations made with the NASA Galaxy Evolution Explorer. GALEX is operated for NASA by the California Institute of Technology under NASA contract NAS5-98034. Funding for SDSS-III has been provided by the Alfred P. Sloan Foundation, the Participating Institutions, the National Science Foundation, and the U.S. Department of Energy Office of Science. The SDSS-III web site is http://www.sdss3.org/. SDSS-III is managed by the Astrophysical Research Consortium for the Participating Institutions of the SDSS-III Collaboration including the University of Arizona, the Brazilian Participation Group, Brookhaven National Laboratory, University of Cambridge, Carnegie Mellon University, University of Florida, the French Participation Group, the German Participation Group, Harvard University, the Instituto de Astrofisica de Canarias, the Michigan State/Notre Dame/JINA Participation Group, Johns Hopkins University, Lawrence Berkeley National Laboratory, Max Planck Institute for Astrophysics, Max Planck Institute for Extraterrestrial Physics, New Mexico State University, New York University, Ohio State University, Pennsylvania State University, University of Portsmouth, Princeton University, the Spanish Participation Group, University of Tokyo, University of Utah, Vanderbilt University, University of Virginia, University of Washington, and Yale University. This publication makes use of data products from the Wide-field Infrared Survey Explorer, which is a joint project of the University of California, Los Angeles, and the Jet Propulsion Laboratory/California Institute of Technology, and NEOWISE, which is a project of the Jet Propulsion Laboratory/California Institute of Technology. WISE and NEOWISE are funded by the National Aeronautics and Space Administration This publication makes use of data products from the Two

Micron All Sky Survey, which is a joint project of the University of Massachusetts and the Infrared Processing and Analysis Center/California Institute of Technology, funded by the National Aeronautics and Space Administration and the National Science Foundation. This publication makes use of data products from the Wide-field Infrared Survey Explorer(Wright et al. 2010), which is a joint project of the University of California, Los Angeles, and the Jet Propulsion Laboratory/California Institute of Technology, funded by the National Aeronautics and Space Administration. Funding for the SDSS and SDSS-II has been provided by the Alfred P. Sloan Foundation, the Participating Institutions, the National Science Foundation, the U.S. Department of Energy, the National Aeronautics and Space Administration, the Japanese Monbukagakusho, the Max Planck Society, and the Higher Education Funding Council for England. The SDSS Web Site is http://www.sdss.org/. The SDSS is managed by the Astrophysical Research Consortium for the Participating Institutions. The Participating Institutions are the American Museum of Natural History, Astrophysical Institute Potsdam, University of Basel, University of Cambridge, Case Western Reserve University, University of Chicago, Drexel University, Fermilab, the Institute for Advanced Study, the Japan Participation Group, Johns Hopkins University, the Joint Institute for Nuclear Astrophysics, the Kavli Institute for Particle Astrophysics and Cosmology, the Korean Scientist Group, the Chinese Academy of Sciences (LAMOST), Los Alamos National Laboratory, the Max-Planck-Institute for Astronomy (MPIA), the Max-Planck-Institute for Astrophysics (MPA), New Mexico State University, Ohio State University, University of Pittsburgh, University of Portsmouth, Princeton University, the United States Naval Observatory, and the University of Washington. The Pan-STARRS1 Surveys (PS1) have been made possible through contributions of the Institute for Astronomy, the University of Hawaii, the Pan-STARRS Project Office, the Max-Planck Society and its participating institutes, the Max Planck Institute for Astronomy, Heidelberg and the Max Planck Institute for Extraterrestrial Physics, Garching, The Johns Hopkins University, Durham University, the University of Edinburgh, Queen's University Belfast, the Harvard-Smithsonian Center for Astrophysics, the Las Cumbres Observatory Global Telescope Network Incorporated, the National Central University of Taiwan, the Space Telescope Science Institute, the National Aeronautics and Space Administration under Grant No. NNX08AR22G issued through the Planetary Science Division of the NASA Science Mission Directorate, the National Science Foundation under Grant No. AST-1238877, the University of Maryland, and Eotvos Lorand University (ELTE). This research has made use of the SIMBAD database, operated at CDS, Strasbourg, France. This research has made use of NASA's Astrophysics Data System. This research has made use of the VizieR catalogue access tool, CDS, Strasbourg, France. This research made use of matplotlib, a Python library for publication quality graphics (Hunter 2007), Astropy, a community-developed core Python package for Astronomy (Astropy Collaboration et al. 2018, 2013), NumPy (Harris et al. 2020) and galpy (`http://github.com/jobovy/galpy`, Bovy 2015). This research has made use of ISIS functions (ISISscripts) provided by ECAP/Remeis observatory and MIT (`http://www.sternwarte.uni-erlangen.de/isis/`). Parts of the acknowledgements were compiled using the Astronomy Acknowledgement Generator.

References

Allen, C. & Santillan, A. 1991, Rev. Mexicana Astron. Astrofis., 22, 255

Astropy Collaboration, Price-Whelan, A. M., Sipőcz, B. M., et al. 2018, AJ, 156, 123

Astropy Collaboration, Robitaille, T. P., Tollerud, E. J., et al. 2013, A&A, 558, A33

Blaauw, A. 1961, Bull. Astron. Inst. Netherlands, 15, 265

Bovy, J. 2015, ApJS, 216, 29

Brown, W. R., Geller, M. J., Kenyon, S. J., & Kurtz, M. J. 2005, ApJ, 622, L33

Cui, X.-Q., Zhao, Y.-H., Chu, Y.-Q., et al. 2012, Research in Astronomy and Astrophysics, 12, 1197

Dekker, H., D'Odorico, S., Kaufer, A., Delabre, B., & Kotzlowski, H. 2000, in Society of Photo-Optical Instrumentation Engineers (SPIE) Conference Series, Vol. 4008, Optical and IR Telescope Instrumentation and Detectors, ed. M. Iye & A. F. Moorwood, 534–545

Dinçel, B., Neuhäuser, R., Yerli, S. K., et al. 2015, MNRAS, 448, 3196

Drake, A. J., Graham, M. J., Djorgovski, S. G., et al. 2014, ApJS, 213, 9

Edelmann, H., Napiwotzki, R., Heber, U., Christlieb, N., & Reimers, D. 2005, ApJ, 634, L181

Fitzpatrick, E. L., Massa, D., Gordon, K. D., Bohlin, R., & Clayton, G. C. 2019, ApJ, 886, 108

Gaia Collaboration, Brown, A. G. A., Vallenari, A., et al. 2018, A&A, 616, A1

Gaia Collaboration, Brown, A. G. A., Vallenari, A., et al. 2020, arXiv e-prints, arXiv:2012.01533

Gaia Collaboration, Prusti, T., de Bruijne, J. H. J., et al. 2016, A&A, 595, A1

Georgy, C., Ekström, S., Granada, A., et al. 2013, A&A, 553, A24

Giddings, J. R. 1981, PhD thesis, -

Greene, J. E., Strader, J., & Ho, L. C. 2020, ARA&A, 58, 257

Handler, G., Pigulski, A., Daszyńska-Daszkiewicz, J., et al. 2019, ApJ, 873, L4

Harris, C. R., Millman, K. J., van der Walt, S. J., et al. 2020, Nature, 585, 357

Hattori, K., Valluri, M., Castro, N., et al. 2019, ApJ, 873, 116

Heber, U., Edelmann, H., Napiwotzki, R., Altmann, M., & Scholz, R. D. 2008, A&A, 483, L21

Hills, J. G. 1988, Nature, 331, 687

Hirsch, H. A., Heber, U., O'Toole, S. J., & Bresolin, F. 2005, A&A, 444, L61

Hoogerwerf, R., de Bruijne, J. H. J., & de Zeeuw, P. T. 2001, A&A, 365, 49

Huang, Y., Liu, X. W., Zhang, H. W., et al. 2017, ApJ, 847, L9

Hunter, J. D. 2007, Computing In Science & Engineering, 9, 90

Irrgang, A. 2014, doctoralthesis, Friedrich-Alexander-Universität Erlangen-Nürnberg (FAU)

Irrgang, A., Kreuzer, S., & Heber, U. 2018, A&A, 620, A48

Irrgang, A., Przybilla, N., Heber, U., et al. 2014, A&A, 565, A63

Irrgang, A., Przybilla, N., Heber, U., Nieva, M. F., & Schuh, S. 2010, ApJ, 711, 138

Irrgang, A., Wilcox, B., Tucker, E., & Schiefelbein, L. 2013, A&A, 549, A137

Kaufer, A., Stahl, O., Tubbesing, S., et al. 1999, The Messenger, 95, 8

Koposov, S. E., Boubert, D., Li, T. S., et al. 2020, MNRAS, 491, 2465

Kreuzer, S., Irrgang, A., & Heber, U. 2020, A&A, 637, A53

Kurucz, R. L. 1996, in Astronomical Society of the Pacific Conference Series, Vol. 108, M.A.S.S., Model Atmospheres and Spectrum Synthesis, ed. S. J. Adelman, F. Kupka, & W. W. Weiss, 160

Li, Y.-B., Luo, A. L., Zhao, G., et al. 2018, AJ, 156, 87

Lindegren, L., Bastian, U., Biermann, M., et al. 2020, arXiv e-prints, arXiv:2012.01742

Neuhäuser, R., Gießler, F., & Hambaryan, V. V. 2020, MNRAS, 498, 899

Poveda, A., Ruiz, J., & Allen, C. 1967, Boletin de los Observatorios Tonantzintla y Tacubaya, 4, 86

Przybilla, N., Fernanda Nieva, M., Heber, U., & Butler, K. 2008, ApJ, 684, L103

Przybilla, N., Nieva, M.-F., & Butler, K. 2011, Journal of Physics: Conference Series, 328, 012015

Raddi, R., Irrgang, A., Heber, U., Schneider, D., & Kreuzer, S. 2021, A&A, 645, A108

Renzo, M., Zapartas, E., de Mink, S. E., et al. 2019, A&A, 624, A66

Schoettler, C., de Bruijne, J., Vaher, E., & Parker, R. J. 2020, MNRAS, 495, 3104

Schönrich, R., Binney, J., & Dehnen, W. 2010, MNRAS, 403, 1829

Silva, M. D. V. & Napiwotzki, R. 2011, MNRAS, 411, 2596

Wright, E. L., Eisenhardt, P. R. M., Mainzer, A. K., et al. 2010, AJ, 140, 1868

Zheng, Z., Carlin, J. L., Beers, T. C., et al. 2014, ApJ, 785, L23

Appendices

A. Tables

Table A.1: Kinematic parameters of the program stars at their current positions. Listed are the positions and velocities in Cartesian coordinates, as well as the Galactic rest-frame velocity $v_{\mathrm{Grf}} = (v_x^2+v_y^2+v_z^2)^{-\frac{1}{2}}$, the escape velocity v_{esc} and the probability P_{b} for the star to be bound to the Galaxy. Results and statistical uncertainties are given as mode and highest density interval of 1σ confidence in case of a unimodal parameter distribution or as the mean and 15.87th and 84.13th percentiles if the distribution is not unimodal.

#	x	y	z	v_x	v_y	v_z	v_{Grf}	$v_{\mathrm{Grf}} - v_{\mathrm{esc}}$	P_{b}
	(kpc)			($\mathrm{km\,s^{-1}}$)					(%)
1	7.62	0.30	1.7	79	229	80	254	−365	100
Stat.	$^{+0.06}_{-0.07}$	$^{+0.03}_{-0.03}$	$^{+0.2}_{-0.1}$	$^{+11}_{-10}$	$^{+3}_{-3}$	$^{+11}_{-15}$	$^{+5}_{-4}$	$^{+5}_{-4}$	...
2	8.72	0.95	−4.5	63	206	−90	234	−362	100
Stat.	$^{+0.01}_{-0.02}$	$^{+0.04}_{-0.05}$	$^{+0.2}_{-0.2}$	$^{+4}_{-3}$	$^{+3}_{-3}$	$^{+1}_{-1}$	$^{+2}_{-2}$	$^{+1}_{-1}$	...
3	6.65	−0.85	2.9	98	463	167	501	−122	100
Stat.	$^{+0.08}_{-0.09}$	$^{+0.04}_{-0.04}$	$^{+0.1}_{-0.1}$	$^{+6}_{-6}$	$^{+11}_{-10}$	$^{+7}_{-7}$	$^{+14}_{-12}$	$^{+14}_{-12}$	...
4	19.2	−8.3	−9.9	142	−4	30	145	−374	100
Stat.	$^{+0.6}_{-0.4}$	$^{+0.3}_{-0.5}$	$^{+0.4}_{-0.6}$	$^{+2}_{-2}$	$^{+7}_{-9}$	$^{+9}_{-7}$	$^{+4}_{-3}$	$^{+7}_{-5}$	...
5	10.8	−6.6	4.0	353	96	33	367	−203	100
Stat.	$^{+0.1}_{-0.1}$	$^{+0.3}_{-0.3}$	$^{+0.2}_{-0.2}$	$^{+14}_{-15}$	$^{+4}_{-4}$	$^{+6}_{-4}$	$^{+13}_{-15}$	$^{+16}_{-16}$	...
6	8.70	−1.10	0.77	41	132	18	139	−472	100
Stat.	$^{+0.01}_{-0.01}$	$^{+0.04}_{-0.05}$	$^{+0.03}_{-0.03}$	$^{+1}_{-1}$	$^{+2}_{-2}$	$^{+2}_{-3}$	$^{+2}_{-2}$	$^{+1}_{-2}$	...
7	8.87	−4.9	4.1	126	85	−55	161	−426	100
Stat.	$^{+0.03}_{-0.02}$	$^{+0.2}_{-0.3}$	$^{+0.2}_{-0.2}$	$^{+7}_{-6}$	$^{+4}_{-5}$	$^{+5}_{-7}$	$^{+6}_{-4}$	$^{+8}_{-5}$	...
8	−1.0	−2.6	−6.1	286	270	−74	400	−224	100
Stat.	$^{+0.5}_{-0.5}$	$^{+0.1}_{-0.1}$	$^{+0.3}_{-0.3}$	$^{+7}_{-7}$	$^{+2}_{-2}$	$^{+10}_{-9}$	$^{+5}_{-6}$	$^{+10}_{-11}$	...
9	4.9	0.79	−2.1	−167	280	2	326	−324	100
Stat.	$^{+0.2}_{-0.2}$	$^{+0.04}_{-0.04}$	$^{+0.1}_{-0.1}$	$^{+2}_{-2}$	$^{+1}_{-0}$	$^{+3}_{-3}$	$^{+1}_{-1}$	$^{+1}_{-1}$	...
10	5.4	0.62	−2.0	−94	196	67	227	−417	100
Stat.	$^{+0.1}_{-0.1}$	$^{+0.03}_{-0.03}$	$^{+0.1}_{-0.1}$	$^{+3}_{-3}$	$^{+3}_{-3}$	$^{+4}_{-4}$	$^{+1}_{-1}$	$^{+2}_{-2}$	...
11	7.39	0.88	−3.4	73	333	−85	352	−261	100
Stat.	$^{+0.05}_{-0.04}$	$^{+0.04}_{-0.05}$	$^{+0.2}_{-0.1}$	$^{+5}_{-5}$	$^{+3}_{-3}$	$^{+2}_{-2}$	$^{+3}_{-4}$	$^{+4}_{-5}$	...
12	6.55	−0.51	0.126	−136	160	78	224	−415	100
Stat.	$^{+0.07}_{-0.07}$	$^{+0.02}_{-0.02}$	$^{+0.004}_{-0.004}$	$^{+1}_{-1}$	$^{+2}_{-2}$	$^{+2}_{-2}$	$^{+1}_{-1}$	$^{+2}_{-2}$	...
13	6.4	−17.0	−9.7	383	−161	−241	480	−49	98.3
Stat.	$^{+0.1}_{-0.1}$	$^{+0.9}_{-0.8}$	$^{+0.5}_{-0.5}$	$^{+21}_{-24}$	$^{+2}_{-2}$	$^{+4}_{-3}$	$^{+18}_{-20}$	$^{+22}_{-25}$	...
14	6.98	0.35	−1.49	50	136	−81	166	−463	100
Stat.	$^{+0.06}_{-0.08}$	$^{+0.02}_{-0.01}$	$^{+0.06}_{-0.09}$	$^{+5}_{-4}$	$^{+5}_{-7}$	$^{+5}_{-7}$	$^{+2}_{-2}$	$^{+3}_{-3}$	...
15	7.10	0.42	−1.7	72	143	−5	160	−465	100
Stat.	$^{+0.06}_{-0.08}$	$^{+0.02}_{-0.02}$	$^{+0.08}_{-0.10}$	$^{+3}_{-2}$	$^{+5}_{-6}$	$^{+3}_{-4}$	$^{+3}_{-4}$	$^{+3}_{-4}$	...

Table A.1 – *Continued from previous page.*

#	x	y	z	v_x	v_y	v_z	$v_{\rm Grf}$	$v_{\rm Grf} - v_{\rm esc}$	$P_{\rm b}$
	(kpc)			(km s^{-1})					(%)
16	7.93	0.44	−1.48	369	388	−183	565	−52	99.7
Stat.	$^{+0.02}_{-0.02}$	$^{+0.02}_{-0.02}$	$^{+0.07}_{-0.08}$	$^{+21}_{-19}$	$^{+5}_{-5}$	$^{+5}_{-5}$	$^{+19}_{-17}$	$^{+20}_{-17}$	...
17	9.77	0.34	−1.72	−212	304	−143	396	−202	100
Stat.	$^{+0.07}_{-0.06}$	$^{+0.02}_{-0.02}$	$^{+0.08}_{-0.09}$	$^{+11}_{-11}$	$^{+3}_{-3}$	$^{+10}_{-10}$	$^{+10}_{-9}$	$^{+11}_{-10}$	...
18	8.81	−0.90	2.0	−21	170	54	179	−427	100
Stat.	$^{+0.02}_{-0.02}$	$^{+0.04}_{-0.05}$	$^{+0.1}_{-0.1}$	$^{+1}_{-1}$	$^{+3}_{-3}$	$^{+3}_{-3}$	$^{+3}_{-3}$	$^{+2}_{-2}$	...
19	8.68	−1.46	2.7	59	288	315	432	−172	100
Stat.	$^{+0.01}_{-0.01}$	$^{+0.07}_{-0.07}$	$^{+0.1}_{-0.1}$	$^{+3}_{-2}$	$^{+7}_{-8}$	$^{+4}_{-4}$	$^{+7}_{-9}$	$^{+8}_{-10}$	...
20	9.10	0.50	3.3	336	395	184	550	−49	100
Stat.	$^{+0.03}_{-0.03}$	$^{+0.02}_{-0.02}$	$^{+0.1}_{-0.2}$	$^{+13}_{-14}$	$^{+5}_{-5}$	$^{+4}_{-4}$	$^{+11}_{-11}$	$^{+12}_{-11}$	...
21	6.98	−0.57	1.72	−230	136	111	290	−337	100
Stat.	$^{+0.06}_{-0.08}$	$^{+0.02}_{-0.03}$	$^{+0.09}_{-0.07}$	$^{+3}_{-3}$	$^{+3}_{-3}$	$^{+3}_{-4}$	$^{+0}_{-1}$	$^{+1}_{-1}$	...
22	11.3	12.7	5.8	−74	149	172	241	−301	100
Stat.	$^{+0.4}_{-0.3}$	$^{+1.9}_{-1.3}$	$^{+0.9}_{-0.6}$	$^{+6}_{-8}$	$^{+13}_{-12}$	$^{+25}_{-21}$	$^{+15}_{-15}$	$^{+23}_{-21}$	...
23	18.0	−8.4	9.1	522	−124	151	557	33	1.6
Stat.	$^{+0.9}_{-0.9}$	$^{+0.8}_{-0.8}$	$^{+0.9}_{-0.9}$	$^{+17}_{-14}$	$^{+6}_{-5}$	$^{+18}_{-23}$	$^{+12}_{-10}$	$^{+18}_{-15}$	...
24	26.9	4.9	−11.5	337	213	−152	426	−70	100
Stat.	$^{+1.6}_{-1.9}$	$^{+0.4}_{-0.5}$	$^{+1.2}_{-1.0}$	$^{+7}_{-8}$	$^{+13}_{-13}$	$^{+8}_{-8}$	$^{+6}_{-6}$	$^{+6}_{-6}$	...
25	21.3	68.9	−22.7	29	529	−211	573	170	0
Stat.	$^{+1.5}_{-1.4}$	$^{+7.7}_{-7.2}$	$^{+2.5}_{-2.4}$	$^{+19}_{-18}$	$^{+11}_{-10}$	$^{+23}_{-28}$	$^{+6}_{-5}$	$^{+14}_{-14}$	...
26	8.348	3.8	−4.8	−10	269	−168	317	−274	100
Stat.	$^{+0.003}_{-0.002}$	$^{+0.2}_{-0.2}$	$^{+0.2}_{-0.2}$	$^{+1}_{-1}$	$^{+4}_{-4}$	$^{+4}_{-3}$	$^{+3}_{-3}$	$^{+2}_{-3}$	...
27	9.47	4.0	−6.6	92	574	53	582	8	43.7
Stat.	$^{+0.10}_{-0.09}$	$^{+0.4}_{-0.4}$	$^{+0.6}_{-0.6}$	$^{+7}_{-8}$	$^{+21}_{-23}$	$^{+16}_{-14}$	$^{+25}_{-23}$	$^{+27}_{-29}$	...
28	12.7	4.5	−5.3	−77	220	−127	266	−297	100
Stat.	$^{+0.2}_{-0.2}$	$^{+0.2}_{-0.2}$	$^{+0.3}_{-0.2}$	$^{+5}_{-4}$	$^{+3}_{-3}$	$^{+6}_{-6}$	$^{+3}_{-3}$	$^{+4}_{-5}$	...
29	12.7	−1.23	3.6	−90	123	156	218	−352	100
Stat.	$^{+0.2}_{-0.2}$	$^{+0.05}_{-0.07}$	$^{+0.2}_{-0.2}$	$^{+5}_{-7}$	$^{+5}_{-6}$	$^{+6}_{-4}$	$^{+4}_{-3}$	$^{+5}_{-5}$	...
30	13.0	−5.9	4.7	126	214	−12	245	−314	100
Stat.	$^{+1.9}_{-1.1}$	$^{+1.4}_{-2.4}$	$^{+1.9}_{-1.1}$	$^{+39}_{-24}$	$^{+15}_{-14}$	$^{+19}_{-32}$	$^{+30}_{-16}$	$^{+48}_{-27}$	...
31	12.1	−1.33	5.0	124	109	−59	176	−395	100
Stat.	$^{+0.2}_{-0.2}$	$^{+0.07}_{-0.06}$	$^{+0.2}_{-0.2}$	$^{+6}_{-5}$	$^{+6}_{-6}$	$^{+6}_{-6}$	$^{+2}_{-2}$	$^{+4}_{-3}$	...
32	8.65	−0.38	2.4	147	171	123	257	−349	100
Stat.	$^{+0.01}_{-0.01}$	$^{+0.02}_{-0.02}$	$^{+0.1}_{-0.1}$	$^{+8}_{-7}$	$^{+3}_{-3}$	$^{+2}_{-2}$	$^{+2}_{-2}$	$^{+2}_{-2}$	...
33	9.73	−1.06	11.1	23	178	22	182	−376	100
Stat.	$^{+0.07}_{-0.07}$	$^{+0.06}_{-0.06}$	$^{+0.6}_{-0.6}$	$^{+3}_{-3}$	$^{+4}_{-4}$	$^{+7}_{-6}$	$^{+4}_{-4}$	$^{+2}_{-2}$	...
34	7.30	−0.36	3.7	−50	43	144	158	−454	100
Stat.	$^{+0.06}_{-0.04}$	$^{+0.02}_{-0.01}$	$^{+0.2}_{-0.2}$	$^{+1}_{-1}$	$^{+11}_{-8}$	$^{+2}_{-2}$	$^{+4}_{-4}$	$^{+3}_{-3}$	...
35	7.46	1.6	3.0	−212	158	114	290	−323	100
Stat.	$^{+0.09}_{-0.10}$	$^{+0.2}_{-0.1}$	$^{+0.3}_{-0.3}$	$^{+16}_{-20}$	$^{+15}_{-15}$	$^{+10}_{-9}$	$^{+11}_{-10}$	$^{+12}_{-11}$	...

Table A.1 – *Continued from previous page.*

#	x	y	z	v_x	v_y	v_z	v_{Grf}	$v_{\mathrm{Grf}} - v_{\mathrm{esc}}$	P_{b}
	(kpc)			($\mathrm{km\,s^{-1}}$)					(%)
36	8.06	1.28	1.8	128	249	81	292	−322	100
Stat.	$^{+0.02}_{-0.03}$	$^{+0.10}_{-0.08}$	$^{+0.1}_{-0.1}$	$^{+12}_{-9}$	$^{+4}_{-4}$	$^{+6}_{-6}$	$^{+6}_{-6}$	$^{+6}_{-6}$	...
37	6.6	5.8	−4.8	−164	73	−95	202	−392	100
Stat.	$^{+0.2}_{-0.2}$	$^{+0.7}_{-0.5}$	$^{+0.4}_{-0.6}$	$^{+15}_{-20}$	$^{+14}_{-20}$	$^{+12}_{-16}$	$^{+16}_{-13}$	$^{+22}_{-17}$	...
38	6.71	6.9	−5.9	−151	145	−59	216	−367	100
Stat.	$^{+0.09}_{-0.09}$	$^{+0.4}_{-0.4}$	$^{+0.3}_{-0.3}$	$^{+8}_{-7}$	$^{+5}_{-6}$	$^{+4}_{-4}$	$^{+3}_{-3}$	$^{+6}_{-5}$	...
39	6.98	2.4	−2.1	−203	210	−58	298	−323	100
Stat.	$^{+0.07}_{-0.07}$	$^{+0.1}_{-0.1}$	$^{+0.1}_{-0.1}$	$^{+8}_{-8}$	$^{+5}_{-5}$	$^{+1}_{-1}$	$^{+2}_{-2}$	$^{+2}_{-2}$	...
40	5.6	1.8	−5.8	−41	51	−207	218	−392	100
Stat.	$^{+0.2}_{-0.2}$	$^{+0.1}_{-0.1}$	$^{+0.4}_{-0.3}$	$^{+3}_{-3}$	$^{+15}_{-14}$	$^{+6}_{-6}$	$^{+4}_{-4}$	$^{+5}_{-5}$	...
41	5.8	2.3	−5.5	71	99	−166	204	−405	100
Stat.	$^{+0.2}_{-0.1}$	$^{+0.1}_{-0.1}$	$^{+0.4}_{-0.3}$	$^{+7}_{-6}$	$^{+10}_{-12}$	$^{+8}_{-7}$	$^{+4}_{-3}$	$^{+6}_{-4}$	...

Table A.2: Kinematic parameters of the program stars at the positions of disk intersection, denoted with a subscript p for "plane". Listed are the positions and velocities at disk intersection in Cartesian coordinates, as well as the Galactic rest-frame velocity $v_{\mathrm{Grf,p}} = (v_{x,\mathrm{p}}^2 + v_{y,\mathrm{p}}^2 + v_{z,\mathrm{p}}^2)^{-\frac{1}{2}}$, the ejection velocity $v_{\mathrm{ej,p}}$ and the time of flight $\tau_{\mathrm{flight,p}}$ from the position of disk intersection to the current position of the star. Results and statistical uncertainties are treated in the same way as in Table A.1.

#	x_{p}	y_{p}	z_{p}	r_{p}	$v_{x,\mathrm{p}}$	$v_{y,\mathrm{p}}$	$v_{z,\mathrm{p}}$	$v_{\mathrm{Grf,p}}$	$v_{\mathrm{ej,p}}$	$\tau_{\mathrm{flight,p}}$
	(kpc)				($\mathrm{km\,s^{-1}}$)					(Myr)
1	5.2	−3.4	0.0	6.3	211	194	122	308	144	16.7
Stat.	$^{+0.5}_{-0.5}$	$^{+0.3}_{-0.3}$	$^{+0.1}_{-0.1}$	$^{+0.3}_{-0.4}$	$^{+23}_{-21}$	$^{+11}_{-13}$	$^{+12}_{-10}$	$^{+12}_{-7}$	$^{+12}_{-12}$	$^{+1.6}_{-1.6}$
2	4.0	−4.98	0.0	6.4	244	129	−188	333	197	31.0
Stat.	$^{+0.2}_{-0.3}$	$^{+0.04}_{-0.05}$	$^{+0.1}_{-0.1}$	$^{+0.2}_{-0.1}$	$^{+6}_{-6}$	$^{+7}_{-7}$	$^{+7}_{-6}$	$^{+6}_{-5}$	$^{+6}_{-7}$	$^{+0.8}_{-0.9}$
3	4.5	−7.4	0.0	8.7	181	403	209	489	348	14.7
Stat.	$^{+0.2}_{-0.2}$	$^{+0.2}_{-0.2}$	$^{+0.1}_{-0.1}$	$^{+0.1}_{-0.1}$	$^{+4}_{-4}$	$^{+9}_{-8}$	$^{+8}_{-8}$	$^{+13}_{-12}$	$^{+19}_{-15}$	$^{+0.1}_{-0.1}$
4	−6.0	0.3	0.0	6.0	159	−188	−331	414	382	108.7
Stat.	$^{+0.6}_{-0.9}$	$^{+0.7}_{-0.5}$	$^{+0.1}_{-0.1}$	$^{+0.9}_{-0.6}$	$^{+11}_{-14}$	$^{+26}_{-19}$	$^{+4}_{-4}$	$^{+11}_{-15}$	$^{+8}_{-11}$	$^{+8.0}_{-5.4}$
5	−7.7	−6.7	0.0	9.9	369	−117	133	409	257	45.4
Stat.	$^{+1.8}_{-1.6}$	$^{+0.2}_{-0.3}$	$^{+0.1}_{-0.1}$	$^{+1.6}_{-1.2}$	$^{+4}_{-4}$	$^{+4}_{-3}$	$^{+4}_{-4}$	$^{+5}_{-5}$	$^{+15}_{-15}$	$^{+3.6}_{-3.5}$
6	6.3	−3.6	0.0	7.2	186	84	48	210	151	21.2
Stat.	$^{+0.3}_{-0.3}$	$^{+0.1}_{-0.2}$	$^{+0.1}_{-0.1}$	$^{+0.1}_{-0.2}$	$^{+11}_{-9}$	$^{+6}_{-7}$	$^{+1}_{-1}$	$^{+7}_{-6}$	$^{+5}_{-4}$	$^{+1.5}_{-1.3}$

Table A.2 – *Continued from previous page.*

#	x_p	y_p	z_p	r_p	$v_{x,\mathrm{p}}$	$v_{y,\mathrm{p}}$	$v_{z,\mathrm{p}}$	$v_\mathrm{Grf,p}$	$v_\mathrm{ej,p}$	$\tau_\mathrm{flight,p}$
	(kpc)				($\mathrm{km\,s^{-1}}$)					(Myr)
7	−4.5	−2.2	0.0	5.0	145	−232	218	349	220	64.4
Stat.	$^{+0.4}_{-0.6}$	$^{+0.4}_{-0.3}$	$^{+0.1}_{-0.1}$	$^{+0.4}_{-0.3}$	$^{+15}_{-22}$	$^{+3}_{-1}$	$^{+4}_{-6}$	$^{+5}_{-7}$	$^{+6}_{-4}$	$^{+3.5}_{-2.3}$
8	−10.3	−10.6	0.0	14.8	179	139	−188	295	354	38.8
Stat.	$^{+0.9}_{-0.8}$	$^{+0.4}_{-0.4}$	$^{+0.1}_{-0.1}$	$^{+0.9}_{-0.9}$	$^{+4}_{-3}$	$^{+7}_{-7}$	$^{+2}_{-2}$	$^{+7}_{-7}$	$^{+10}_{-10}$	$^{+0.8}_{-0.9}$
9	6.5	−7.4	0.0	9.85	41	184	−95	211	171	32.6
Stat.	$^{+0.2}_{-0.1}$	$^{+0.1}_{-0.1}$	$^{+0.1}_{-0.1}$	$^{+0.03}_{-0.03}$	$^{+2}_{-2}$	$^{+5}_{-5}$	$^{+3}_{-4}$	$^{+2}_{-2}$	$^{+3}_{-3}$	$^{+0.9}_{-0.8}$
10	1.85	−5.9	0.0	6.2	193	−15	−123	230	156	49.1
Stat.	$^{+0.09}_{-0.08}$	$^{+0.1}_{-0.1}$	$^{+0.1}_{-0.1}$	$^{+0.2}_{-0.1}$	$^{+2}_{-2}$	$^{+6}_{-5}$	$^{+6}_{-6}$	$^{+3}_{-2}$	$^{+8}_{-7}$	$^{+0.5}_{-0.5}$
11	3.5	−7.1	0.0	7.89	218	245	−167	368	217	25.4
Stat.	$^{+0.3}_{-0.3}$	$^{+0.2}_{-0.2}$	$^{+0.1}_{-0.1}$	$^{+0.05}_{-0.04}$	$^{+4}_{-5}$	$^{+3}_{-2}$	$^{+5}_{-5}$	$^{+3}_{-5}$	$^{+8}_{-9}$	$^{+0.6}_{-0.7}$
12	6.75	−0.77	0.0	6.80	−122	159	79	215	188	1.570
Stat.	$^{+0.08}_{-0.06}$	$^{+0.02}_{-0.02}$	$^{+0.1}_{-0.1}$	$^{+0.08}_{-0.06}$	$^{+1}_{-1}$	$^{+2}_{-2}$	$^{+3}_{-2}$	$^{+1}_{-1}$	$^{+2}_{-2}$	$^{+0.005}_{-0.005}$
13	−7.5	−9.2	0.0	11.9	363	−275	−287	537	354	35.6
Stat.	$^{+1.6}_{-1.4}$	$^{+0.5}_{-0.5}$	$^{+0.1}_{-0.1}$	$^{+1.2}_{-1.3}$	$^{+16}_{-18}$	$^{+4}_{-4}$	$^{+2}_{-2}$	$^{+10}_{-10}$	$^{+13}_{-\ 2}$	$^{+1.7}_{-1.7}$
14	5.4	−1.5	0.0	5.6	174	121	−122	245	196	14.0
Stat.	$^{+0.2}_{-0.2}$	$^{+0.1}_{-0.1}$	$^{+0.1}_{-0.1}$	$^{+0.2}_{-0.2}$	$^{+10}_{-\ 9}$	$^{+5}_{-6}$	$^{+6}_{-7}$	$^{+6}_{-5}$	$^{+13}_{-\ 9}$	$^{+0.4}_{-0.4}$
15	1.92	−2.9	0.0	3.5	314	40	−125	341	196	27.0
Stat.	$^{+0.07}_{-0.08}$	$^{+0.2}_{-0.1}$	$^{+0.1}_{-0.1}$	$^{+0.2}_{-0.2}$	$^{+4}_{-4}$	$^{+3}_{-3}$	$^{+6}_{-7}$	$^{+6}_{-5}$	$^{+12}_{-\ 9}$	$^{+0.5}_{-0.4}$
16	4.8	−2.53	0.0	5.5	433	375	−202	608	414	7.5
Stat.	$^{+0.2}_{-0.2}$	$^{+0.08}_{-0.08}$	$^{+0.1}_{-0.1}$	$^{+0.2}_{-0.2}$	$^{+23}_{-21}$	$^{+4}_{-4}$	$^{+7}_{-6}$	$^{+21}_{-19}$	$^{+17}_{-18}$	$^{+0.2}_{-0.2}$
17	11.9	−3.1	0.0	12.3	−155	297	−154	369	273	11.3
Stat.	$^{+0.2}_{-0.2}$	$^{+0.1}_{-0.1}$	$^{+0.1}_{-0.1}$	$^{+0.3}_{-0.2}$	$^{+12}_{-11}$	$^{+3}_{-3}$	$^{+\ 9}_{-10}$	$^{+\ 9}_{-11}$	$^{+13}_{-12}$	$^{+0.5}_{-0.5}$
18	7.4	−4.8	0.0	8.85	126	117	96	197	129	25.5
Stat.	$^{+0.1}_{-0.1}$	$^{+0.2}_{-0.2}$	$^{+0.1}_{-0.1}$	$^{+0.01}_{-0.01}$	$^{+4}_{-5}$	$^{+6}_{-6}$	$^{+2}_{-2}$	$^{+1}_{-1}$	$^{+4}_{-4}$	$^{+1.1}_{-1.5}$
19	7.98	−3.8	0.0	8.85	108	272	331	442	335	8.3
Stat.	$^{+0.03}_{-0.04}$	$^{+0.2}_{-0.2}$	$^{+0.1}_{-0.1}$	$^{+0.06}_{-0.06}$	$^{+3}_{-3}$	$^{+7}_{-6}$	$^{+4}_{-5}$	$^{+8}_{-9}$	$^{+6}_{-6}$	$^{+0.3}_{-0.3}$
20	3.1	−5.5	0.0	6.27	435	343	231	600	388	15.3
Stat.	$^{+0.5}_{-0.5}$	$^{+0.3}_{-0.4}$	$^{+0.1}_{-0.1}$	$^{+0.04}_{-0.02}$	$^{+14}_{-18}$	$^{+2}_{-3}$	$^{+1}_{-1}$	$^{+\ 9}_{-11}$	$^{+15}_{-12}$	$^{+0.9}_{-0.8}$
21	9.5	−2.34	0.0	9.8	−142	122	136	232	266	13.3
Stat.	$^{+0.1}_{-0.1}$	$^{+0.10}_{-0.09}$	$^{+0.1}_{-0.1}$	$^{+0.1}_{-0.1}$	$^{+2}_{-2}$	$^{+4}_{-5}$	$^{+2}_{-2}$	$^{+4}_{-5}$	$^{+1}_{-1}$	$^{+0.9}_{-0.9}$
22	12.6	6.9	0.0	14.3	1	212	194	288	227	31.1
Stat.	$^{+0.9}_{-0.6}$	$^{+2.2}_{-1.5}$	$^{+0.1}_{-0.1}$	$^{+1.8}_{-1.3}$	$^{+16}_{-20}$	$^{+11}_{-14}$	$^{+22}_{-17}$	$^{+11}_{-10}$	$^{+17}_{-15}$	$^{+0.7}_{-0.8}$
23	−5.8	−1.0	0.0	5.8	517	−275	328	658	589	41.5
Stat.	$^{+2.6}_{-3.5}$	$^{+0.7}_{-0.6}$	$^{+0.1}_{-0.1}$	$^{+3.3}_{-2.4}$	$^{+19}_{-\ 9}$	$^{+24}_{-\ 2}$	$^{+\ 5}_{-19}$	$^{+32}_{-21}$	$^{+\ 9}_{-11}$	$^{+7.1}_{-5.6}$
24	2.0	−7.5	0.0	7.9	502	129	−235	568	362	60.3
Stat.	$^{+1.3}_{-1.6}$	$^{+0.4}_{-0.5}$	$^{+0.1}_{-0.1}$	$^{+0.5}_{-0.5}$	$^{+11}_{-11}$	$^{+26}_{-26}$	$^{+\ 8}_{-10}$	$^{+9}_{-8}$	$^{+11}_{-10}$	$^{+5.5}_{-6.1}$
25	16.3	11.2	0.0	18.5	85	633	−231	665	552	95.8
Stat.	$^{+2.6}_{-2.5}$	$^{+8.6}_{-7.2}$	$^{+0.1}_{-0.1}$	$^{+6.9}_{-4.5}$	$^{+31}_{-26}$	$^{+\ 9}_{-30}$	$^{+14}_{-21}$	$^{+17}_{-14}$	$^{+30}_{-41}$	$^{+11.0}_{-\ 9.3}$

Table A.2 – *Continued from previous page.*

#	x_p	y_p	z_p	r_p	$v_{x,\mathrm{p}}$	$v_{y,\mathrm{p}}$	$v_{z,\mathrm{p}}$	$v_{\mathrm{Grf,p}}$	$v_{\mathrm{ej,p}}$	$\tau_{\mathrm{flight,p}}$
	(kpc)				($\mathrm{km\,s^{-1}}$)					(Myr)
26	7.13	−2.88	0.0	7.69	127	269	−229	375	236	23.3
Stat.	$^{+0.06}_{-0.06}$	$^{+0.08}_{-0.07}$	$^{+0.1}_{-0.1}$	$^{+0.08}_{-0.08}$	$^{+3}_{-3}$	$^{+3}_{-3}$	$^{+6}_{-6}$	$^{+3}_{-3}$	$^{+5}_{-6}$	$^{+0.7}_{-0.7}$
27	−13.6	−60	0.0	60	169	381	−62	421	440	130
Stat.	$^{+5.5}_{-8.5}$	$^{+10}_{-30}$	$^{+0.1}_{-0.1}$	$^{+30}_{-20}$	$^{+6}_{-6}$	$^{+14}_{-15}$	$^{+12}_{-10}$	$^{+11}_{-12}$	$^{+13}_{-21}$	$^{+50}_{-30}$
28	13.2	−3.6	0.0	13.7	50	223	−163	281	164	34.5
Stat.	$^{+0.4}_{-0.4}$	$^{+0.2}_{-0.2}$	$^{+0.1}_{-0.1}$	$^{+0.3}_{-0.3}$	$^{+7}_{-6}$	$^{+2}_{-2}$	$^{+5}_{-5}$	$^{+3}_{-3}$	$^{+5}_{-6}$	$^{+0.7}_{-0.6}$
29	13.7	−3.76	0.0	14.2	−9	108	175	206	222	21.3
Stat.	$^{+0.4}_{-0.3}$	$^{+0.04}_{-0.04}$	$^{+0.1}_{-0.1}$	$^{+0.4}_{-0.3}$	$^{+6}_{-8}$	$^{+5}_{-6}$	$^{+6}_{-5}$	$^{+2}_{-2}$	$^{+9}_{-8}$	$^{+0.4}_{-0.4}$
30	−5.4	−14.4	0.0	14.2	211	−91	85	238	95	90
Stat.	$^{+\ 5.4}_{-13.3}$	$^{+2.2}_{-3.7}$	$^{+0.1}_{-0.1}$	$^{+10.7}_{-\ 3.6}$	$^{+32}_{-59}$	$^{+25}_{-\ 6}$	$^{+8}_{-9}$	$^{+23}_{-47}$	$^{+16}_{-\ 9}$	$^{+70}_{-30}$
31	−5.3	−3.3	0.0	6.3	202	−151	237	344	255	74.0
Stat.	$^{+0.5}_{-0.5}$	$^{+0.3}_{-0.2}$	$^{+0.1}_{-0.1}$	$^{+0.3}_{-0.3}$	$^{+13}_{-14}$	$^{+4}_{-2}$	$^{+7}_{-9}$	$^{+5}_{-5}$	$^{+10}_{-13}$	$^{+3.0}_{-2.5}$
32	5.3	−3.06	0.0	6.1	264	138	164	341	230	16.3
Stat.	$^{+0.3}_{-0.3}$	$^{+0.08}_{-0.07}$	$^{+0.1}_{-0.1}$	$^{+0.2}_{-0.2}$	$^{+15}_{-11}$	$^{+6}_{-7}$	$^{+3}_{-3}$	$^{+9}_{-8}$	$^{+6}_{-6}$	$^{+0.8}_{-0.7}$
33	0.6	−10.4	0.0	10.4	171	−35	216	277	231	83.7
Stat.	$^{+0.4}_{-0.4}$	$^{+0.2}_{-0.2}$	$^{+0.1}_{-0.1}$	$^{+0.2}_{-0.2}$	$^{+4}_{-4}$	$^{+9}_{-9}$	$^{+5}_{-7}$	$^{+5}_{-4}$	$^{+6}_{-7}$	$^{+4.2}_{-4.0}$
34	7.0	−1.2	0.0	7.1	90	27	204	225	299	20.6
Stat.	$^{+0.1}_{-0.1}$	$^{+0.1}_{-0.1}$	$^{+0.1}_{-0.1}$	$^{+0.1}_{-0.1}$	$^{+6}_{-6}$	$^{+10}_{-\ 8}$	$^{+4}_{-4}$	$^{+4}_{-5}$	$^{+10}_{-12}$	$^{+0.7}_{-1.0}$
35	10.7	−2.0	0.0	10.9	−94	157	154	240	220	21.4
Stat.	$^{+0.5}_{-0.4}$	$^{+0.2}_{-0.2}$	$^{+0.1}_{-0.1}$	$^{+0.5}_{-0.4}$	$^{+17}_{-16}$	$^{+13}_{-13}$	$^{+9}_{-8}$	$^{+12}_{-12}$	$^{+15}_{-15}$	$^{+2.0}_{-1.9}$
36	4.8	−2.85	0.0	5.6	264	225	126	368	188	16.6
Stat.	$^{+0.3}_{-0.4}$	$^{+0.08}_{-0.08}$	$^{+0.1}_{-0.1}$	$^{+0.3}_{-0.3}$	$^{+17}_{-16}$	$^{+6}_{-7}$	$^{+8}_{-7}$	$^{+13}_{-11}$	$^{+15}_{-11}$	$^{+0.7}_{-0.7}$
37	9.8	1.8	0.0	9.9	−5	146	−166	219	192	34.5
Stat.	$^{+0.9}_{-0.6}$	$^{+1.2}_{-0.9}$	$^{+0.1}_{-0.1}$	$^{+1.1}_{-0.7}$	$^{+27}_{-37}$	$^{+\ 7}_{-10}$	$^{+\ 9}_{-11}$	$^{+4}_{-2}$	$^{+9}_{-7}$	$^{+0.7}_{-0.7}$
38	9.4	−2.4	0.0	9.7	67	196	−164	263	168	48.1
Stat.	$^{+0.5}_{-0.5}$	$^{+0.3}_{-0.3}$	$^{+0.1}_{-0.1}$	$^{+0.4}_{-0.4}$	$^{+12}_{-14}$	$^{+1}_{-2}$	$^{+3}_{-3}$	$^{+1}_{-1}$	$^{+3}_{-3}$	$^{+1.2}_{-1.1}$
39	10.1	−2.95	0.0	10.5	−57	209	−102	239	161	24.0
Stat.	$^{+0.2}_{-0.2}$	$^{+0.06}_{-0.06}$	$^{+0.1}_{-0.1}$	$^{+0.2}_{-0.1}$	$^{+6}_{-5}$	$^{+4}_{-3}$	$^{+2}_{-2}$	$^{+1}_{-1}$	$^{+4}_{-4}$	$^{+0.7}_{-0.8}$
40	5.1	0.3	0.0	5.1	112	76	−312	339	374	21.7
Stat.	$^{+0.2}_{-0.2}$	$^{+0.3}_{-0.3}$	$^{+0.1}_{-0.1}$	$^{+0.2}_{-0.2}$	$^{+4}_{-5}$	$^{+7}_{-6}$	$^{+13}_{-11}$	$^{+10}_{-10}$	$^{+18}_{-19}$	$^{+0.6}_{-0.7}$
41	2.5	−0.4	0.0	2.5	266	119	−320	432	401	23.0
Stat.	$^{+0.3}_{-0.3}$	$^{+0.2}_{-0.3}$	$^{+0.1}_{-0.1}$	$^{+0.4}_{-0.3}$	$^{+9}_{-8}$	$^{+2}_{-1}$	$^{+20}_{-18}$	$^{+20}_{-20}$	$^{+33}_{-29}$	$^{+0.4}_{-0.3}$

B. Figures

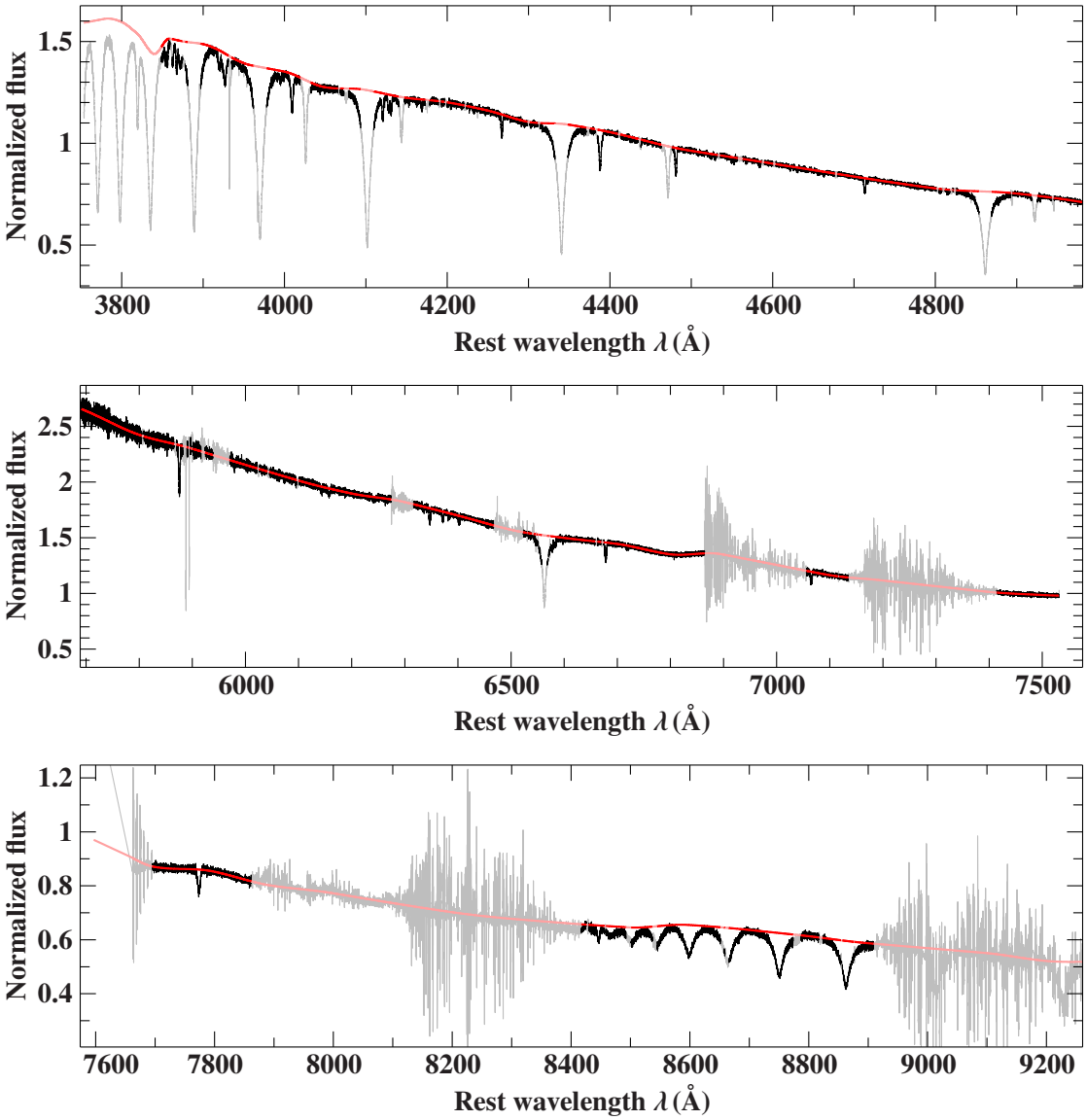

Figure B.1: Cubic spline interpolation of the continuum of EC 10500−1358.

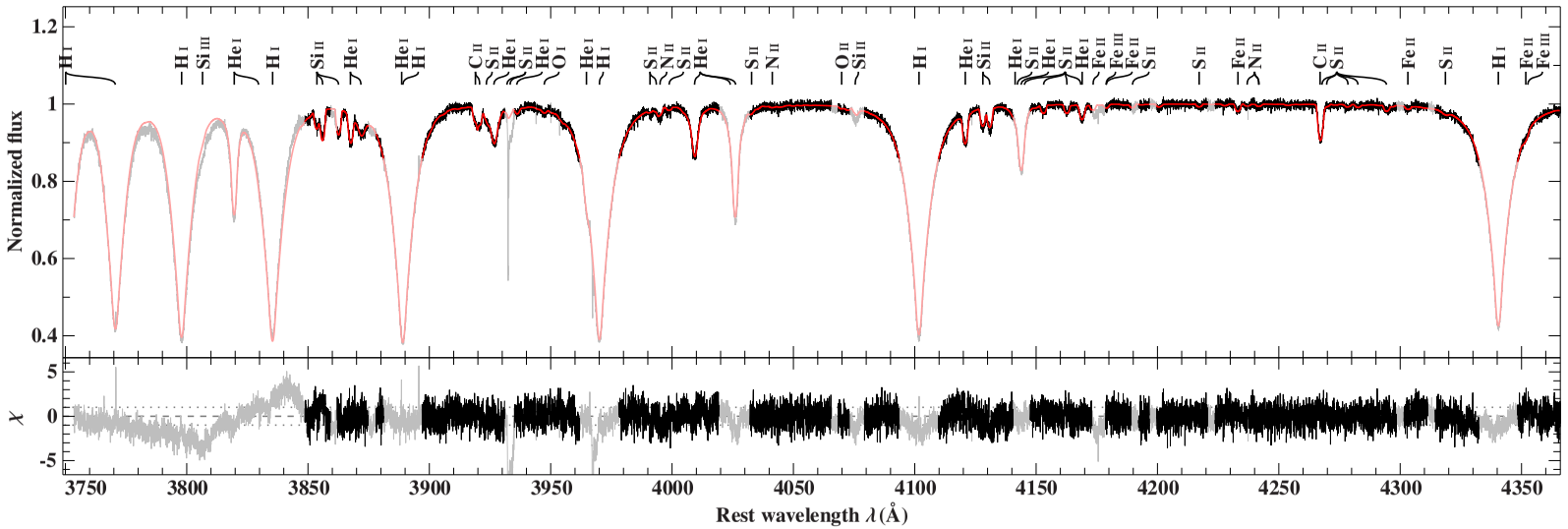

Figure B.2: Spectral fit of EC 10500−1358 (Part 1).

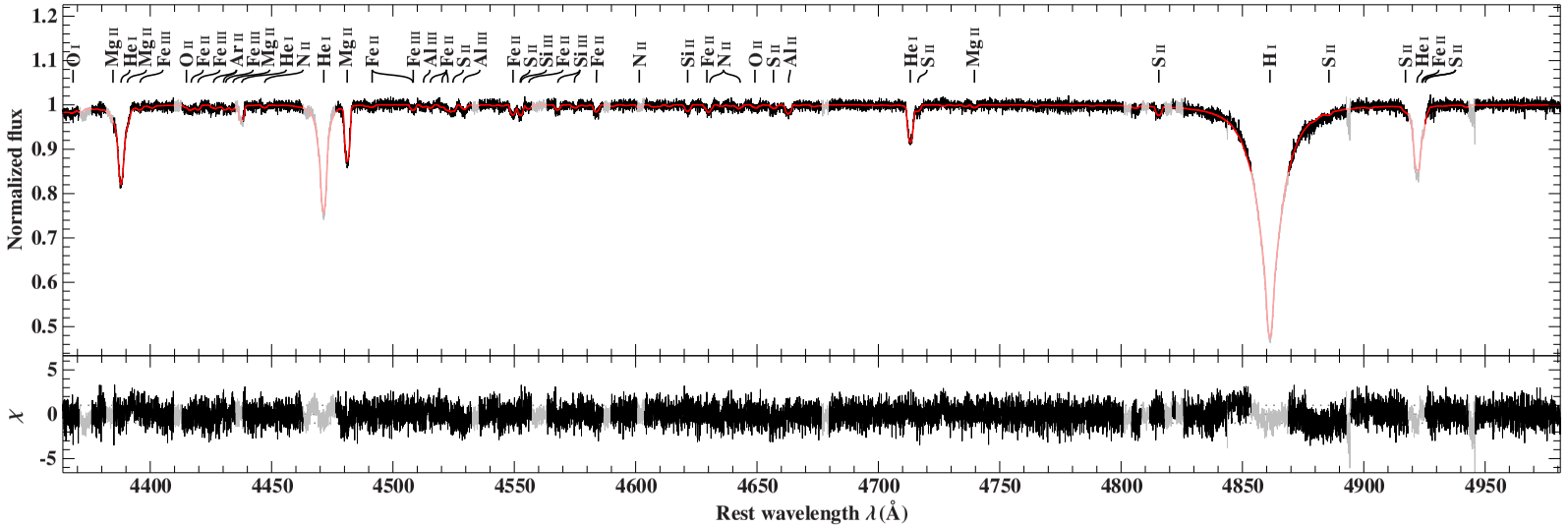

Figure B.3: Spectral fit of EC 10500−1358 (Part 2).

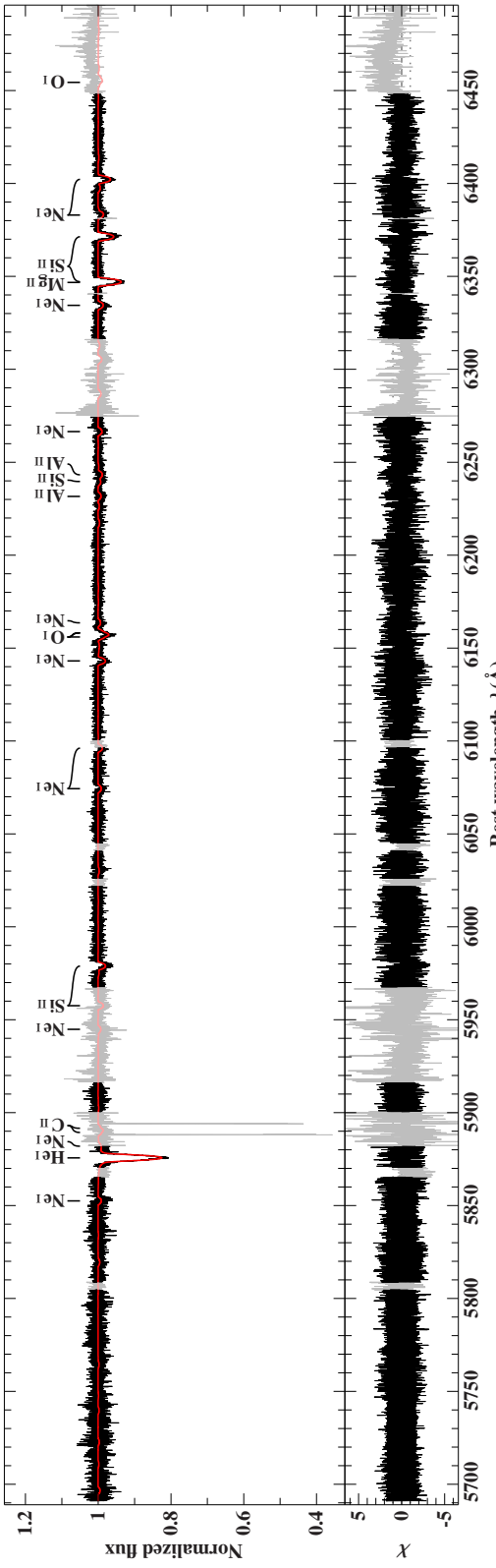

Figure B.4: Spectral fit of EC 10500−1358 (Part 3).

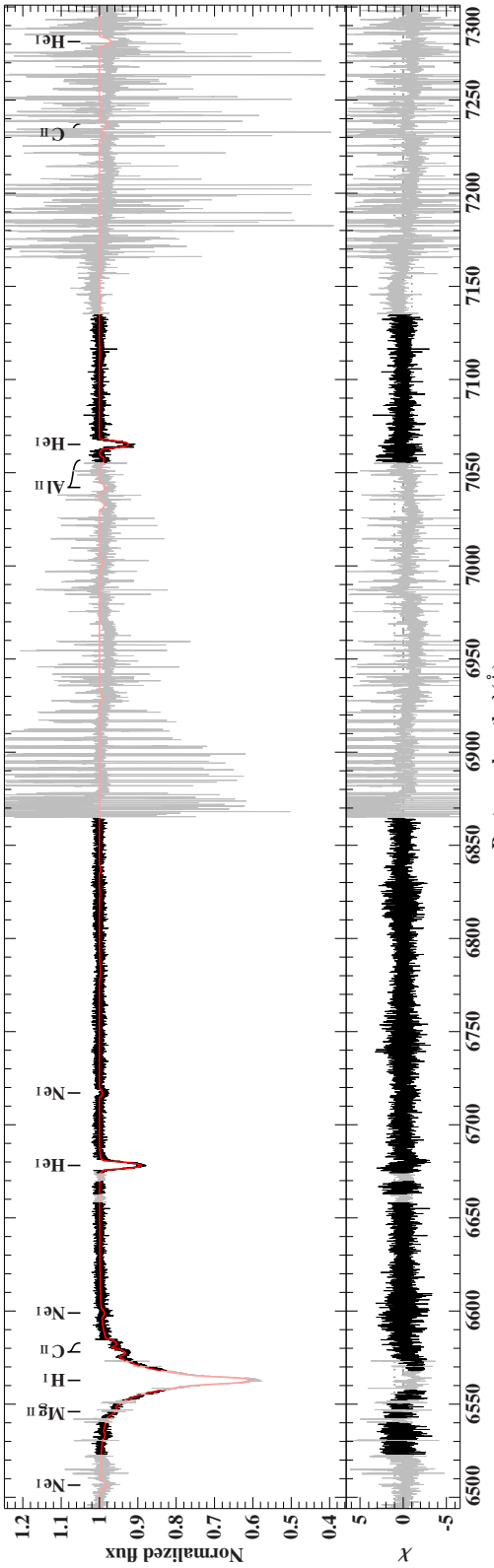

Figure B.5: Spectral fit of EC 10500−1358 (Part 4).

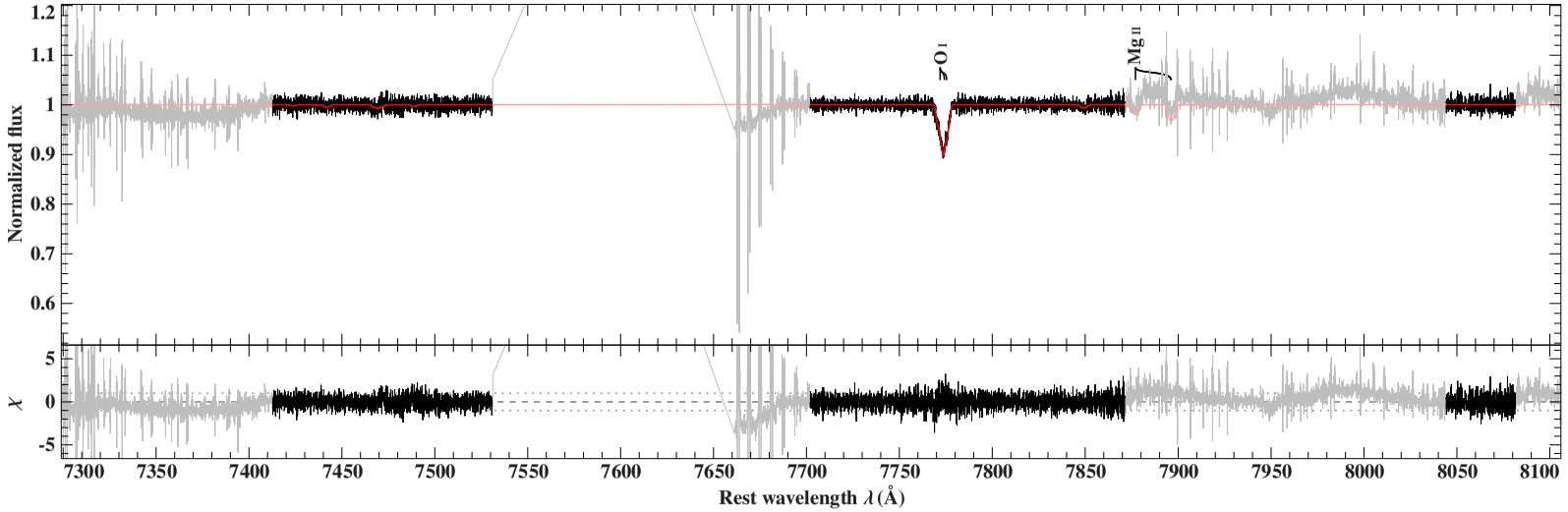

Figure B.6: Spectral fit of EC 10500−1358 (Part 5).

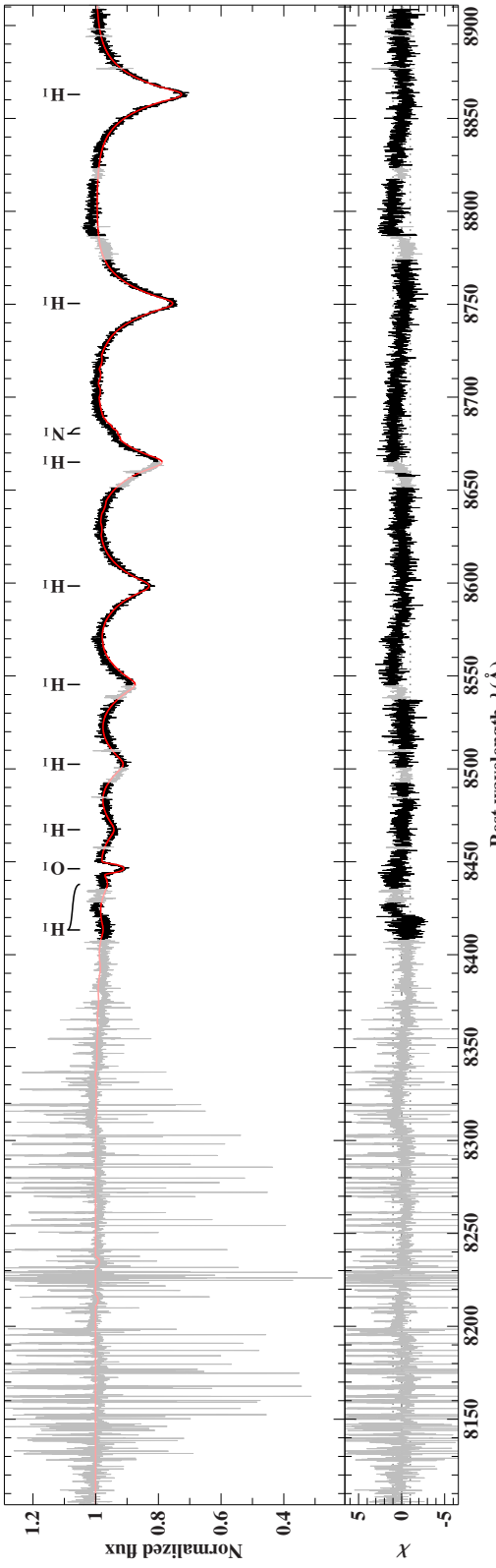

Figure B.7: Spectral fit of EC 10500−1358 (Part 6).

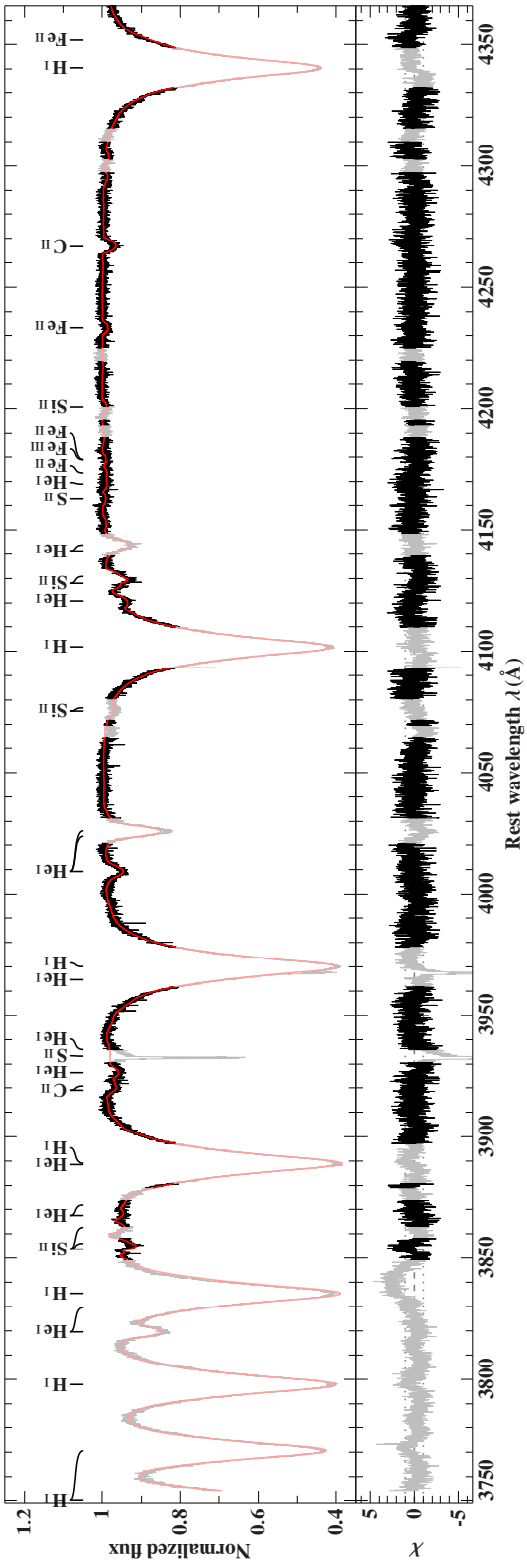

Figure B.8: Spectral fit of PG 0955+291 (Part 1).

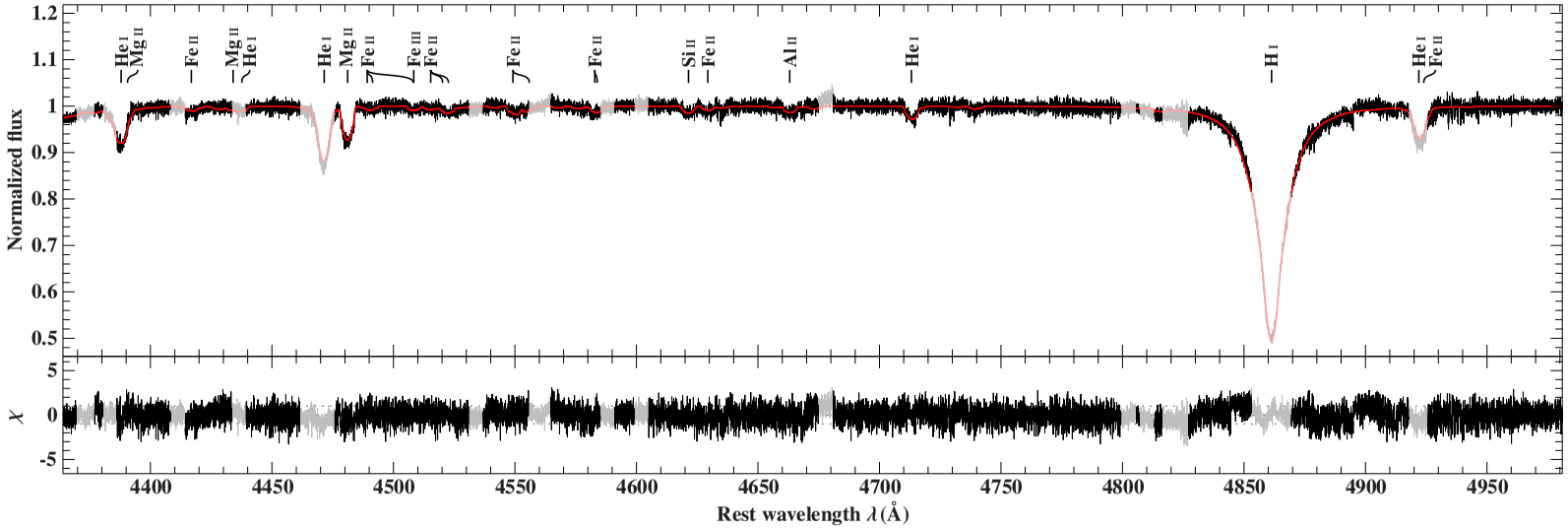

Figure B.9: Spectral fit of PG 0955+291 (Part 2).

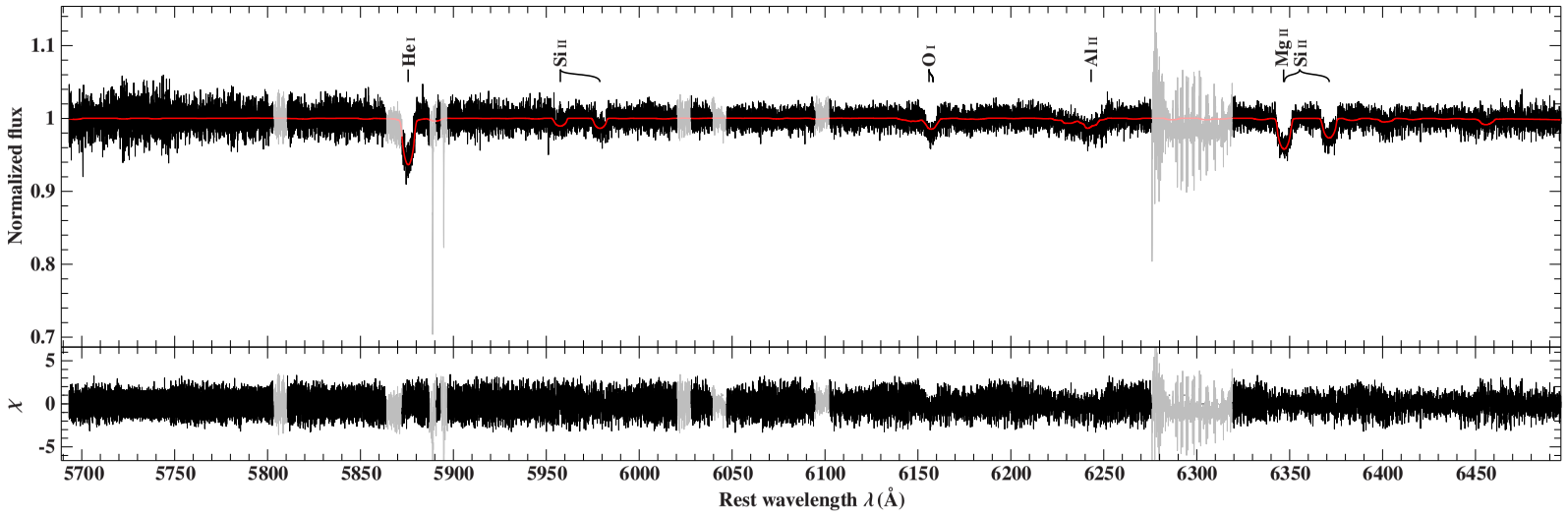

Figure B.10: Spectral fit of PG 0955+291 (Part 3).

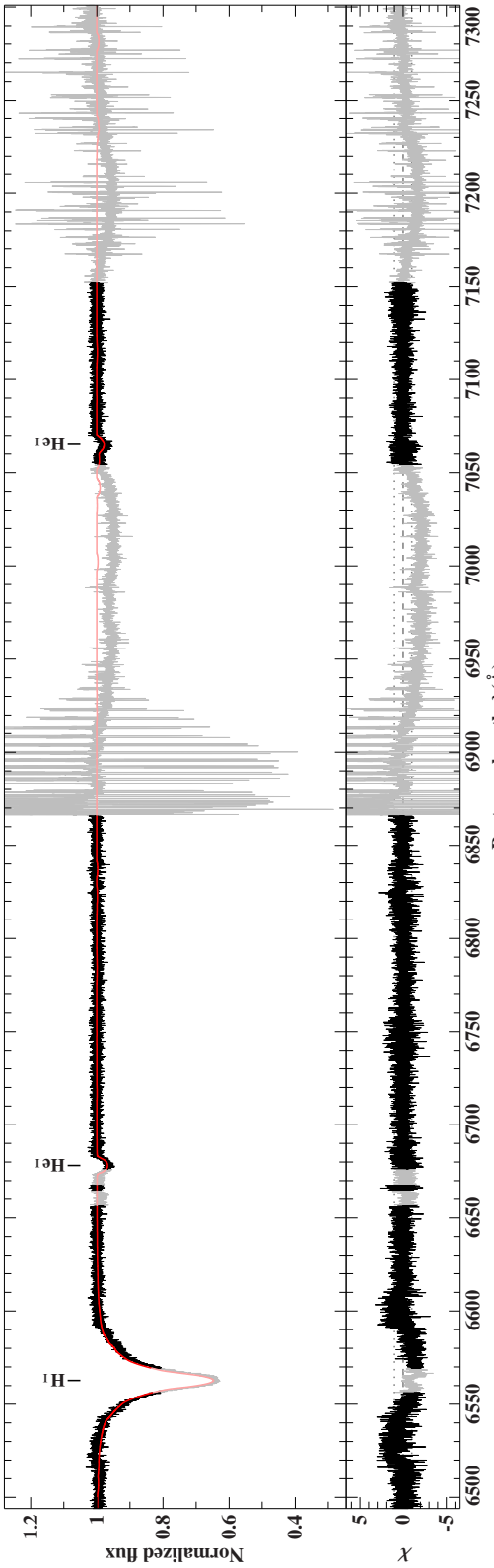

Figure B.11: Spectral fit of PG 0955+291 (Part 4).

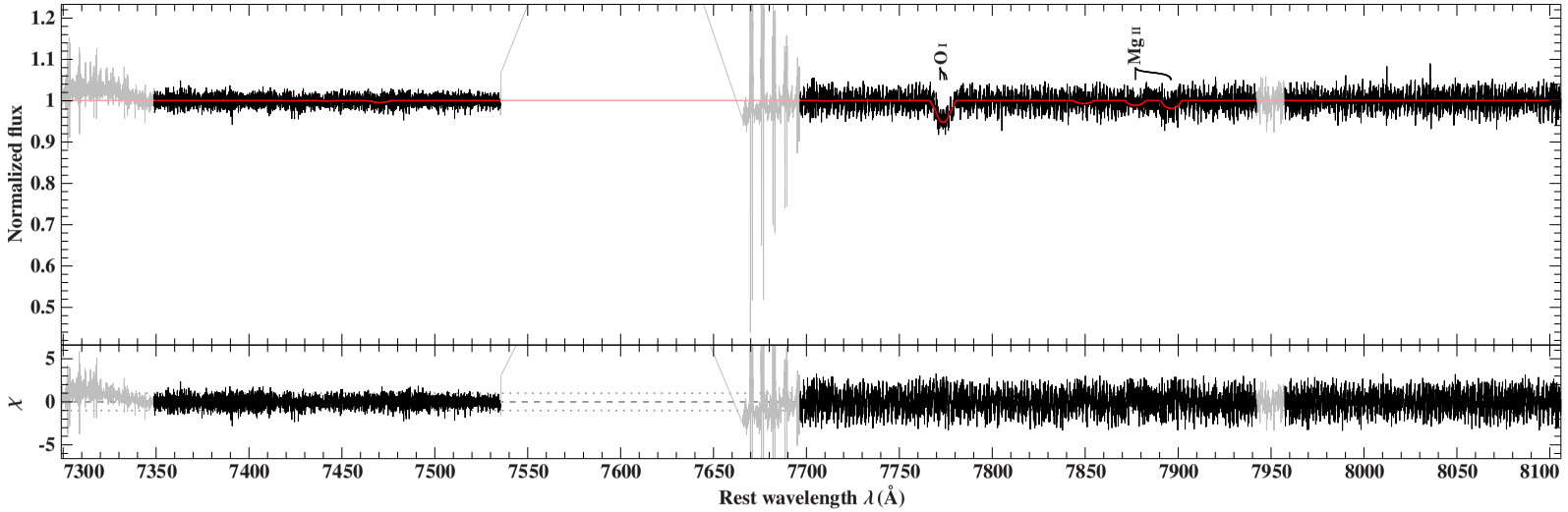

Figure B.12: Spectral fit of PG 0955+291 (Part 5).

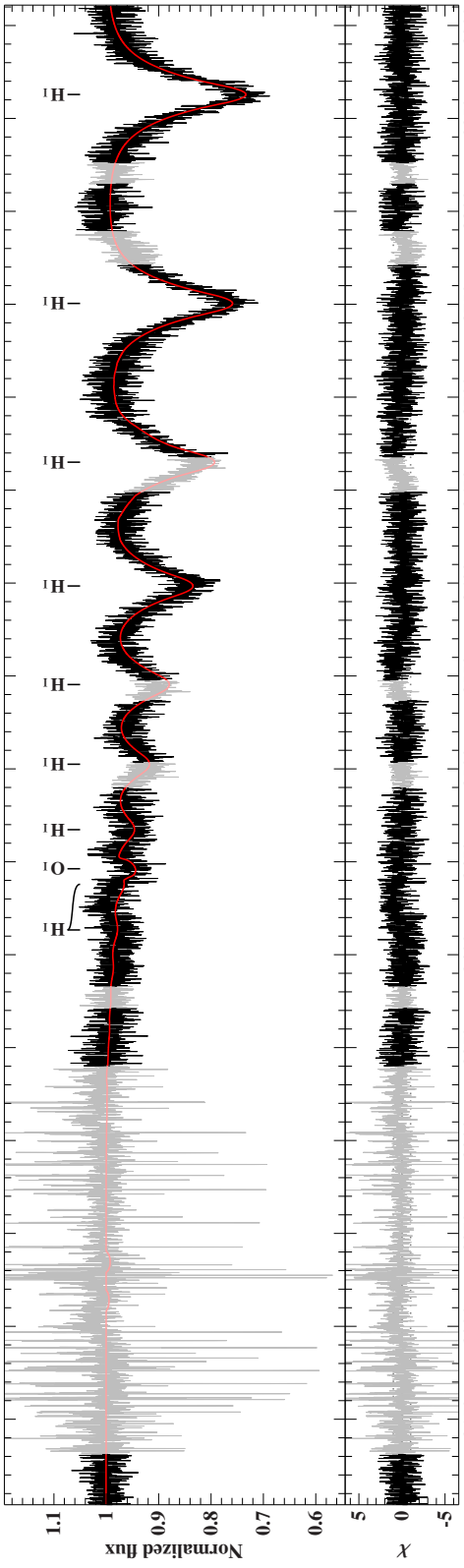

Figure B.13: Spectral fit of PG 0955+291 (Part 6).

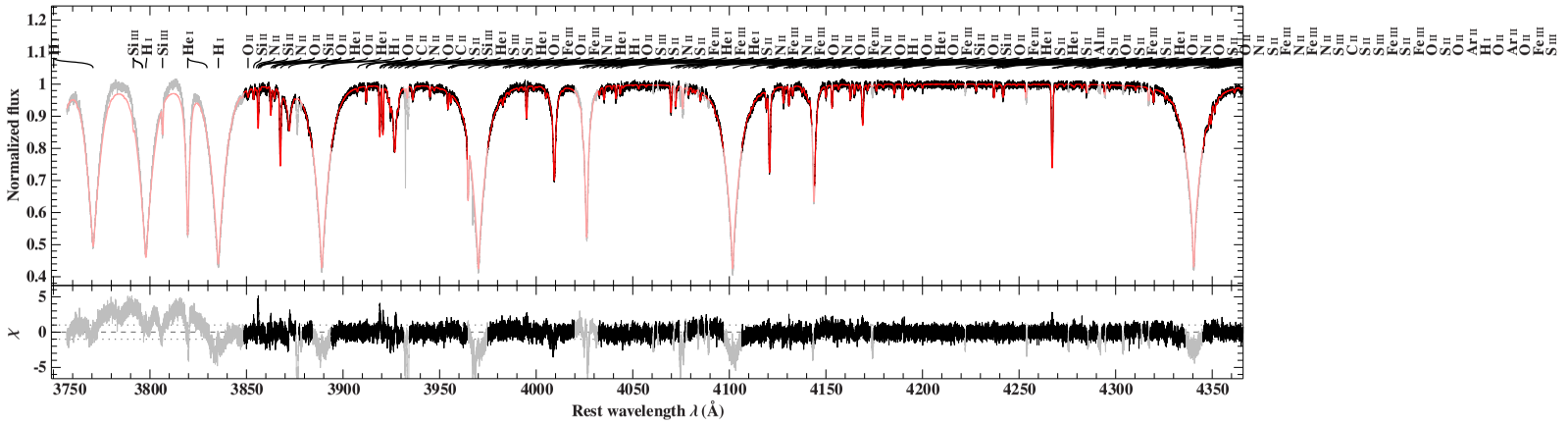

Figure B.14: Spectral fit of BD −15 115 (Part 1).

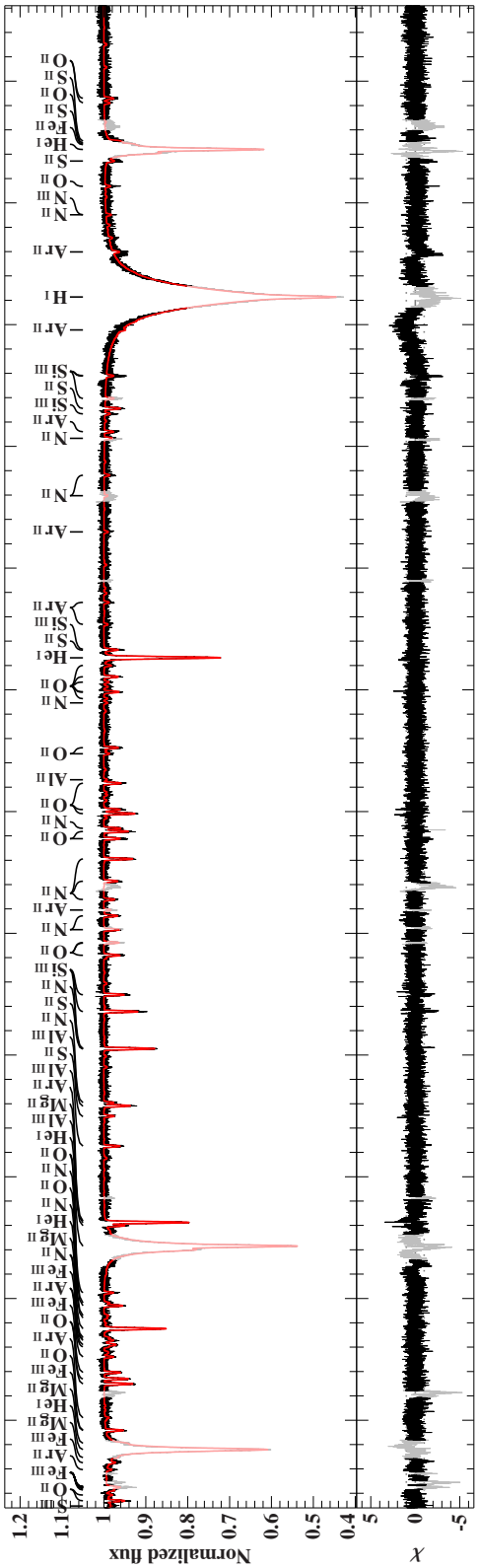

Figure B.15: Spectral fit of BD −15 115 (Part 2).

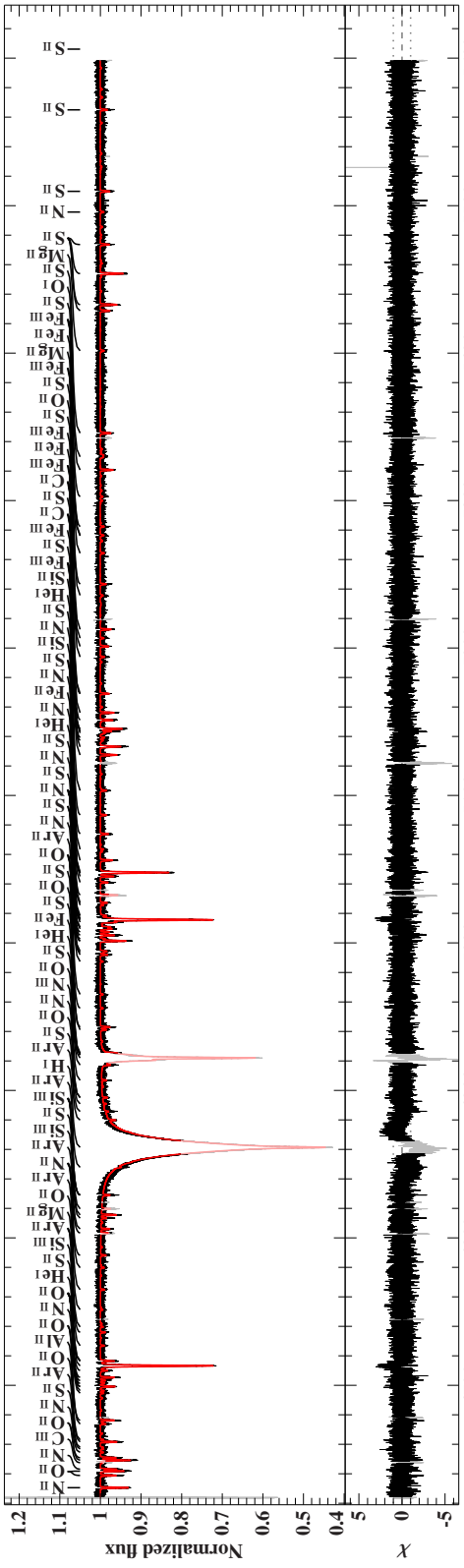

Figure B.16: Spectral fit of BD −15 115 (Part 3).

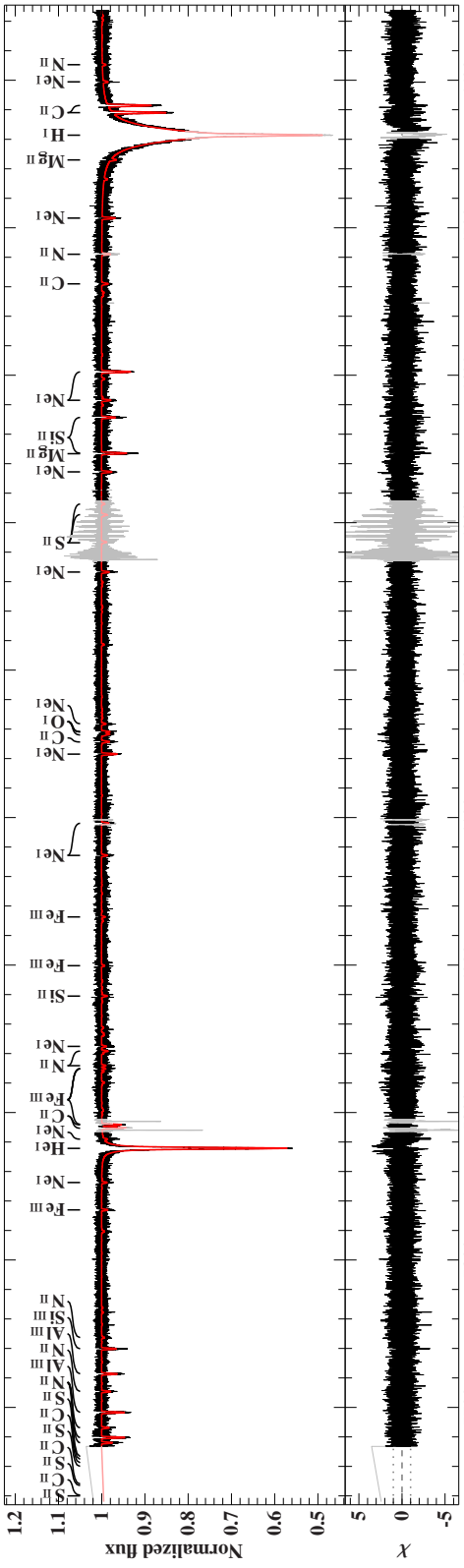

Figure B.17: Spectral fit of BD −15 115 (Part 4).

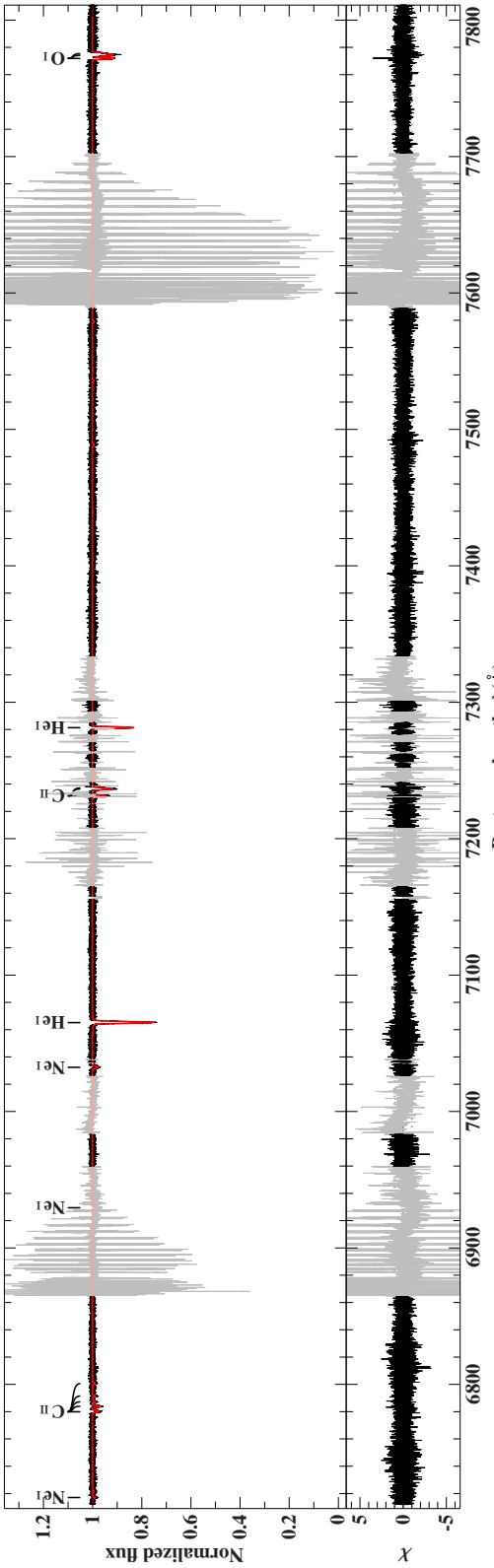

Figure B.18: Spectral fit of BD −15 115 (Part 5).

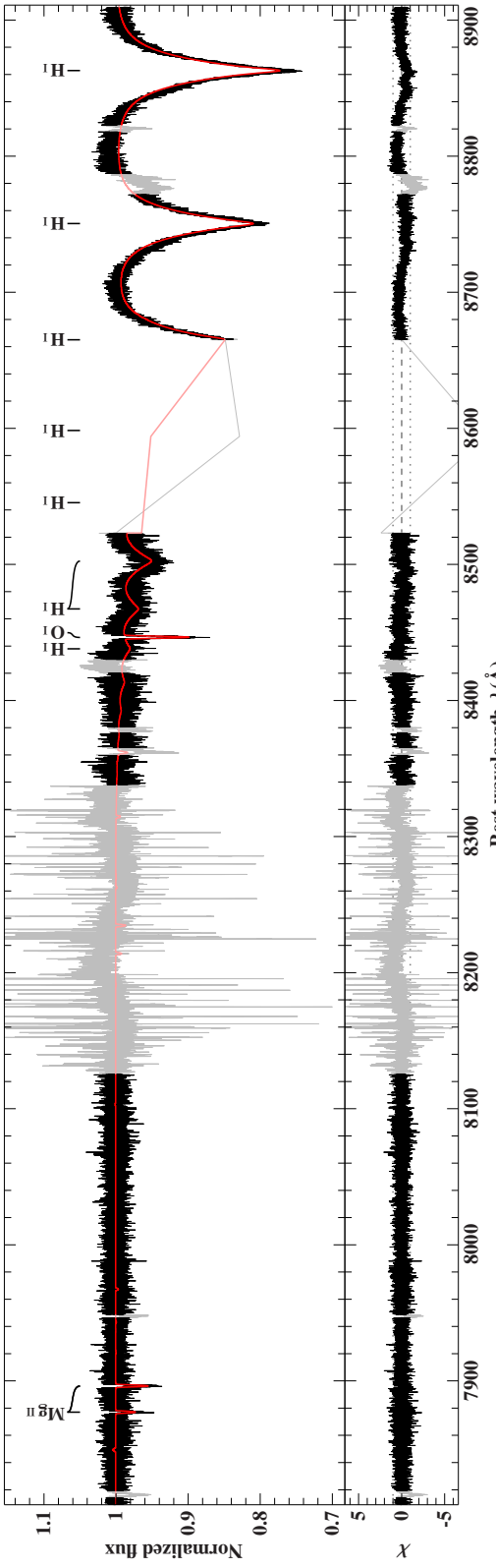

Figure B.19: Spectral fit of BD −15 115 (Part 6).

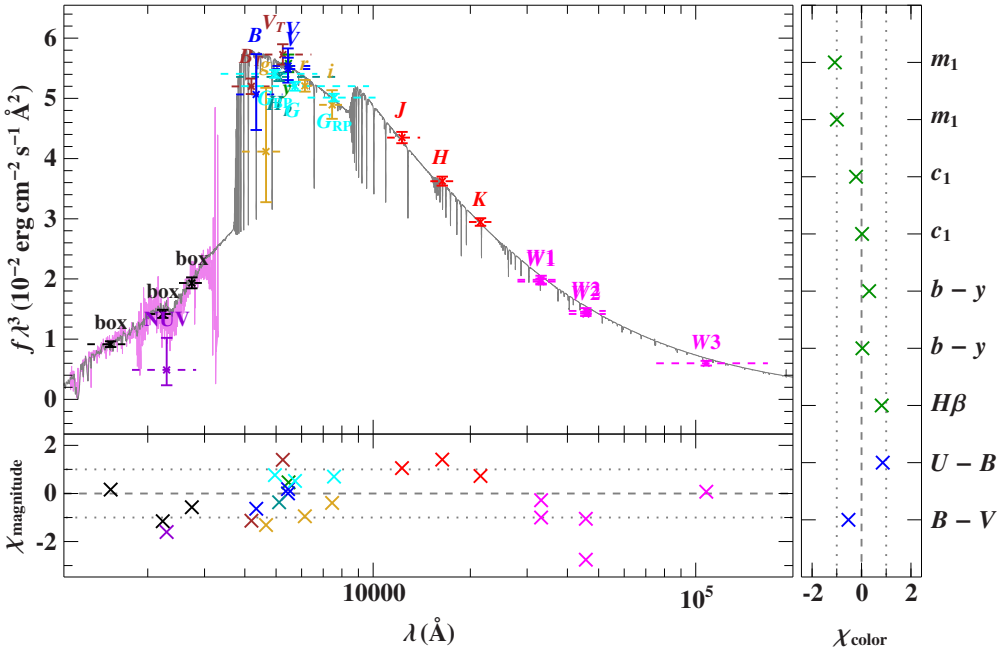

Figure B.20: Photometric fit of BD +20 3004.

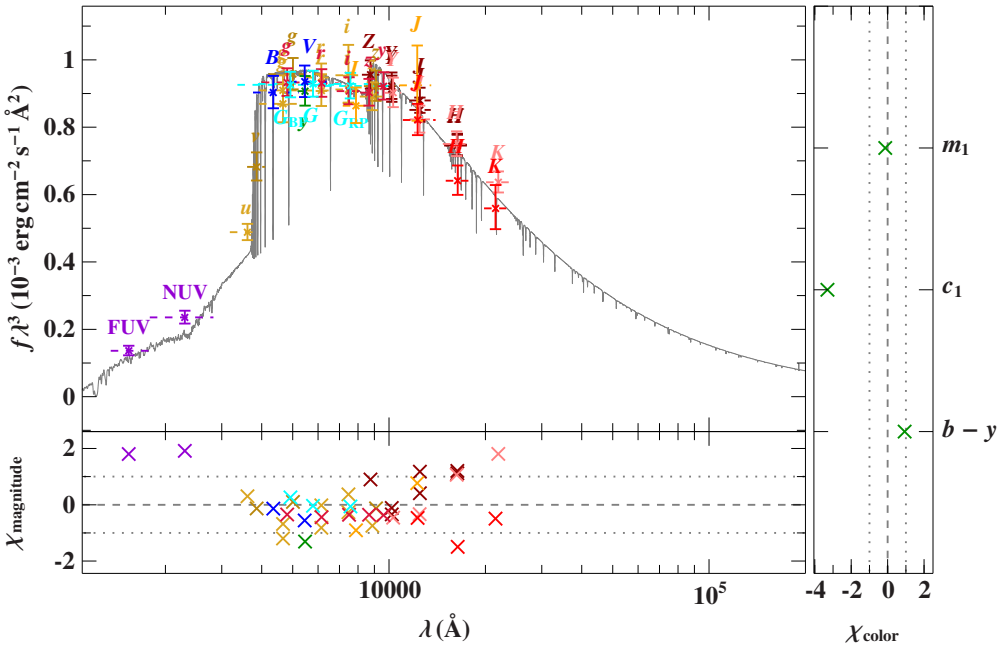

Figure B.21: Photometric fit of PG 0914+001.

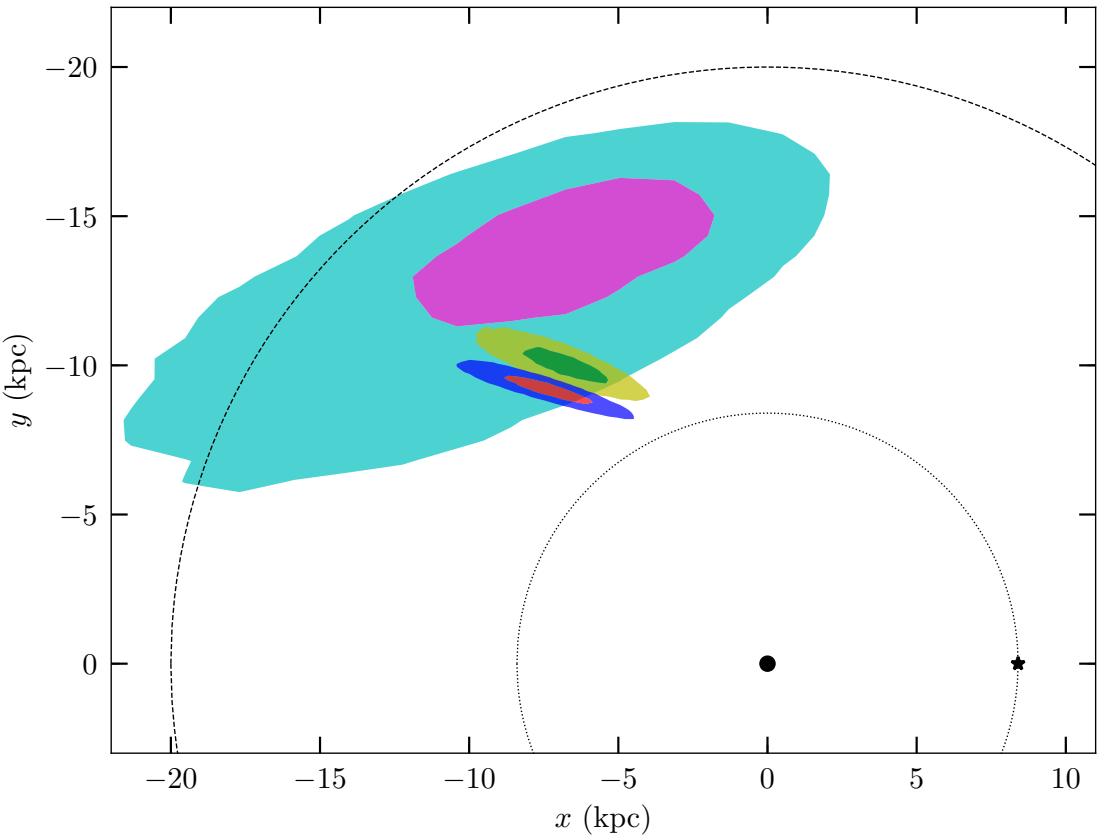

Figure B.22: Galactic plane crossing contours of HD 271791 for different proper motion values. The 1σ and 2σ contours are shown for the following proper motions: *Hipparcos* (magenta/cyan): $\mu_\alpha \cos(\delta) = -1.50 \pm 1.48$ mas/yr, $\mu_\delta = 6.89 \pm 1.82$ mas/yr; *Gaia* DR2 (green/yellow): $\mu_\alpha \cos(\delta) = -0.619 \pm 0.067$ mas/yr, $\mu_\delta = 4.731 \pm 0.071$ mas/yr; *Gaia* EDR3 (red/blue): $\mu_\alpha \cos(\delta) = -0.413 \pm 0.035$ mas/yr, $\mu_\delta = 4.704 \pm 0.042$ mas/yr. Coordinates, distance and radial velocity are kept the same for all three cases. The Galactic center is marked as a black dot and the position of the Sun as a black star. The solar circle (dotted circle, 8.4 kpc) and the edge of the Galactic disk (dashed circle, 20 kpc) are shown for reference.

C. Python code for the Model I halo potential

```
import numpy as nu
from galpy.potential.Potential import Potential,
        kms_to_kpcGyrDecorator, _APY_LOADED
if _APY_LOADED:
    from astropy import units

from galpy.potential.mwpotentials import Irrgang13I
from galpy.util import bovy_conversion

class Model_I_halo(Potential):
    def __init__(self,amp=1.,a=2.562,Lambda=200.,
                 gamma=2.,normalize=False,
                 ro=None,vo=None):
        """
        NAME:
           __init__
        PURPOSE:
           initialize a Irrgang13I_halo potential
        INPUT:
           amp - amplitude to be applied to the potential
           a - scale length (can be Quantity)
           \\Lambda - cut-off parameter (can be Quantity)
           \\gamma - exponent
           normalize - if True, normalize such that
                       vc(1.,0.)=1., or, if given as a
                       number, such that the force is
                       this fraction of the force necessary
                       to make vc(1.,0.)=1.
           ro=, vo= distance and velocity scales for
                    translation into internal units
                    (default from configuration file)
        OUTPUT:
           (none)
        HISTORY:
           2019-10-24 - Written - Dimpel
        """
        Potential.__init__(self,amp=amp,ro=ro,vo=vo,
                           amp_units='mass')
        if _APY_LOADED and isinstance(a,units.Quantity):
            a= a.to(units.kpc).value/self._ro
            Lamda= Lambda.to(units.kpc).value/self._ro
        self._a= a
```

```
        self._scale= self._a
        self._Lambda= Lambda
        self._gamma= gamma
        self._a2= self._a**2.
        if normalize or \
                (isinstance(normalize,(int,float)) \
                     and not isinstance(normalize,bool)):
            self.normalize(normalize)
        self.hasC= False
        self.hasC_dxdv= False
        self._nemo_accname= 'Model_I_halo'

    def _evaluate(self,R,z,phi=0.,t=0.):
        """
        NAME:
           _evaluate
        PURPOSE:
           evaluate the potential at R,z
        INPUT:
           R - Galactocentric cylindrical radius
           z - vertical height
           phi - azimuth
           t - time
        OUTPUT:
           Phi(R,z)
        HISTORY:
           2019-10-24 - Written - Dimpel
        """
        r= nu.sqrt(R**2.+z**2.)
        if r<self._Lambda:
            return (1./self._a)*(1./(self._gamma-1.)*\
                    nu.log((1.+(nu.sqrt(R**2.+z**2.)/\
                    self._a)**(self._gamma-1.))/(1.+\
                    (self._Lambda/self._a)**\
                    (self._gamma-1.)))-((self._Lambda/\
                    self._a)** (self._gamma-1.))/\
                    (1.+(self._Lambda/self._a)**\
                    (self._gamma-1.)))
        else:
            return -1./nu.sqrt(R**2.+z**2.)*\
            ((self._Lambda/self._a)**(self._gamma))/\
            (1.+(self._Lambda/self._a)**(self._gamma-1.))

    def _Rforce(self,R,z,phi=0.,t=0.):
```

```
        """
        NAME:
           _Rforce
        PURPOSE:
           evaluate the radial force for this potential
        INPUT:
           R - Galactocentric cylindrical radius
           z - vertical height
           phi - azimuth
           t - time
        OUTPUT:
           the radial force
        HISTORY:
           2019-10-24 - Written - Dimpel
        """
        r= nu.sqrt(R**2.+z**2.)
        if r<self._Lambda:
            dPhidrr= -(R*(nu.sqrt(R**2.+z**2.)/self._a)**\
                       self._gamma)/((R**2.+z**2.)*(self._a*\
                       (nu.sqrt(R**2.+z**2.)/self._a)**\
                       self._gamma + nu.sqrt(R**2.+z**2.)))
        else:
            dPhidrr= -((R**2.+z**2.)**-1.5)*R*\
                       ((self._Lambda/self._a)**\
                       (self._gamma))/(1.+\
                       (self._Lambda/self._a)**\
                       (self._gamma-1.))
        return dPhidrr

    def _zforce(self,R,z,phi=0.,t=0.):
        """
        NAME:
           _zforce
        PURPOSE:
           evaluate the vertical force for this potential
        INPUT:
           R - Galactocentric cylindrical radius
           z - vertical height
           phi - azimuth
           t - time
        OUTPUT:
           the vertical force
        HISTORY:
           2019-10-24 - Written - Dimpel
```

```
    """
    r= nu.sqrt(R**2.+z**2.)
    if r<self._Lambda:
        dPhidrr= -(z*(nu.sqrt(R**2.+z**2.)/\
                  self._a)**self._gamma)/\
                  ((R**2.+z**2.)*(self._a*\
                  (nu.sqrt(R**2.+z**2.)/self._a)**\
                  self._gamma + nu.sqrt(R**2.+z**2.)))
    else:
        dPhidrr= -((R**2.+z**2.)**-1.5)*z*\
                  ((self._Lambda/self._a)**\
                  (self._gamma))/(1.+\
                  (self._Lambda/self._a)**\
                  (self._gamma-1.))
    return dPhidrr

def _dens(self,R,z,phi=0.,t=0.):
    """
    NAME:
       _dens
    PURPOSE:
       evaluate the density for this potential
    INPUT:
       R - Galactocentric cylindrical radius
       z - vertical height
       phi - azimuth
       t - time
    OUTPUT:
       the density
    HISTORY:
       2019-10-24 - Written - Dimpel
    """
    r= nu.sqrt(R**2.+z**2.)
    if r<self._Lambda:
        return 1./(4.*nu.pi*self._a)*((nu.sqrt(R**2.+\
                z**2.)/self._a)**(self._gamma-1.)*\
                ((nu.sqrt(R**2.+z**2.)/self._a)**\
                (self._gamma-1.)+self._gamma))/\
                ((R**2.+z**2.)*(1.+(nu.sqrt(R**2.+\
                z**2.)/self._a)**(self._gamma-1.))**2.)
    else:
        return 0.

def _R2deriv(self,R,z,phi=0.,t=0.):
```

```
        """
        NAME:
           _R2deriv
        PURPOSE:
           evaluate the second radial derivative for
           this potential
        INPUT:
           R - Galactocentric cylindrical radius
           z - vertical height
           phi - azimuth
           t - time
        OUTPUT:
           the second radial derivative
        HISTORY:
           2019-10-24 - Written - Dimpel
        """
        r= nu.sqrt(R**2.+z**2.)
        if r<self._Lambda:
            t1 = ((self._gamma-2.)*(self._gamma-1.)*R**2.*\
                 (nu.sqrt(R**2.+z**2.)/self._a)**\
                 (self._gamma-3.))/(self._a2*(R**2.+z**2.)*\
                 ((nu.sqrt(R**2.+z**2.)/self._a)**\
                 (self._gamma-1.)+1.))
            t2 = ((self._gamma-1.)**2.*R**2.*(nu.sqrt(R**2.+\
                 z**2.)/self._a)**(2.*self._gamma-4.))/\
                 (self._a2*(R**2.+z**2.)*((nu.sqrt(R**2.+\
                 z**2.)/self._a)**(self._gamma-1.)+1.)**2.)
            t3 = ((self._gamma-1.)*(nu.sqrt(R**2.+z**2.)/\
                 self._a)**(self._gamma-2.))/(self._a*\
                 nu.sqrt(R**2.+z**2.)*((nu.sqrt(R**2.+z**2.)/\
                 self._a)**(self._gamma-1.)+1.))
            t4 = ((self._gamma-1.)*R**2.*(nu.sqrt(R**2.+\
                 z**2.)/self._a)**(self._gamma-2.))/\
                 (self._a*(R**2.+z**2.)**1.5*\
                 ((nu.sqrt(R**2.+z**2.)/self._a)**\
                 (self._gamma-1.)+1.))
            return 1./(self._a*(self._gamma-1.))*(t1-t2+t3-t4)
        else:
            return -(2.*R**2.-z**2.)*(R**2.+z**2.)**(-2.5)*\
                    ((self._Lambda/self._a)**(self._gamma))/\
                    (1.+(self._Lambda/self._a)**\
                    (self._gamma-1.))

    def _z2deriv(self,R,z,phi=0.,t=0.):
```

```
    """
    NAME:
        _z2deriv
    PURPOSE:
        evaluate the second vertical derivative for
        this potential
    INPUT:
       R - Galactocentric cylindrical radius
        z - vertical height
        phi - azimuth
        t - time
    OUTPUT:
        the second vertical derivative
    HISTORY:
        2019-10-24 - Written - Dimpel
    """
    r= nu.sqrt(R**2.+z**2.)
    if r<self._Lambda:
        t1 = ((self._gamma-2.)*(self._gamma-1.)*z**2.*\
             (nu.sqrt(R**2.+z**2.)/self._a)**\
             (self._gamma-3.))/(self._a2*(R**2.+z**2.)*\
             ((nu.sqrt(R**2.+z**2.)/self._a)**\
             (self._gamma-1.)+1.))
        t2 = ((self._gamma-1.)**2.*z**2.*(nu.sqrt(R**2.+\
             z**2.)/self._a)**(2.*self._gamma-4.))/\
             (self._a2*(R**2.+z**2.)*((nu.sqrt(R**2.+\
             z**2.)/self._a)**(self._gamma-1.)+1.)**2.)
        t3 = ((self._gamma-1.)*(nu.sqrt(R**2.+z**2.)/\
             self._a)**(self._gamma-2.))/(self._a*\
             nu.sqrt(R**2.+z**2.)*((nu.sqrt(R**2.+z**2.)/\
             self._a)**(self._gamma-1.)+1.))
        t4 = ((self._gamma-1.)*z**2.*(nu.sqrt(R**2.+\
             z**2.)/self._a)**(self._gamma-2.))/(self._a*\
             (R**2.+z**2.)**1.5*((nu.sqrt(R**2.+z**2.)/\
             self._a)** (self._gamma-1.)+1.))
        return 1./(self._a*(self._gamma-1))*(t1-t2+t3-t4)
    else:
        return (R**2.-2.*z**2.)*(R**2.+z**2.)**(-2.5)*\
               ((self._Lambda/self._a)**(self._gamma))/\
               (1.+(self._Lambda/self._a)**\
               (self._gamma-1.))
```

```
def _Rzderiv(self,R,z,phi=0.,t=0.):
    """
    NAME:
       _Rzderiv
    PURPOSE:
       evaluate the mixed R,z derivative for this
       potential
    INPUT:
       R - Galactocentric cylindrical radius
       z - vertical height
       phi - azimuth
       t - time
    OUTPUT:
       d2phi/dR/dz
    HISTORY:
       2019-10-24 - Written - Dimpel
    """
    r= nu.sqrt(R**2.+z**2.)
    if r<self._Lambda:
        return -(R*z*(nu.sqrt(R**2.+z**2.)/self._a)**\
                 self._gamma*(2.*self._a* (nu.sqrt(R**2.+\
                 z**2.)/self._a)**self._gamma -\
                 (self._gamma-3.)*nu.sqrt(R**2.+z**2.)))/\
                 ((R**2.+z**2.)**2.*(self._a*(nu.sqrt(\
                 R**2.+ z**2.)/self._a)**self._gamma +\
                 nu.sqrt(R**2.+z**2.))**2.)
    else:
        return -3.*R*z*(R**2.+z**2.)**-2.5*\
                 ((self._Lambda/self._a)**(self._gamma))/\
                 (1.+(self._Lambda/self._a)**\
                 (self._gamma-1.))

@kms_to_kpcGyrDecorator
def _nemo_accpars(self,vo,ro):
    """
    NAME:
       _nemo_accpars
    PURPOSE:
       return the accpars potential parameters for use
       of this potential with NEMO
    INPUT:
       vo - velocity unit in km/s
       ro - length unit in kpc
    OUTPUT:
```

```
            accpars string
        HISTORY:
            2019-10-24 - Written - Dimpel
        """
        ampl= self._amp*vo**2.*ro
        return "0,%s,%s,%s,%s" % (ampl, self._a*ro,
                                  self._Lambda*ro, self._gamma)


mgal_in_msun= 1e5/bovy_conversion._G
# complete Model I:
ro, vo = 8.4, 242.
ModelI = Irrgang13I[0:2] +\
         Model_I_halo(amp=1018.*mgal_in_msun/\
                bovy_conversion.mass_in_msol(vo,ro),\
                a=2.562/ro,gamma=2.,Lambda=200./ro)
```

Erklärung:

Hiermit erkläre ich, dass ich die Arbeit selbstständig angefertigt und keine anderen als die angegebenen Hilfsmittel verwendet habe.

Ort, Datum	Markus Dimpel